4-2020

Numerical Investigation of Leading-Edge Modifications of a NACA Airfoil

Anisur Rahman Ikram
Grand Valley State University

Numerical Investigation of Leading-Edge Modifications of a NACA Airfoil

Submitted by

Anisur Rahman Ikram

A Thesis Submitted to the Graduate Faculty of

GRAND VALLEY STATE UNIVERSITY

In

Partial Fulfillment of the Requirements

For the Degree of

Master of Science in Engineering

School of Engineering

April 2020

Acknowledgement

First, and most of all I would like to express my deepest gratitude to my thesis supervisor Dr. Sanjivan Manoharan, for his assistance, guidance and expertise throughout the process of completion of this thesis. He continuously encouraged me and provided technical support from the beginning of this journey. Without his motivation and help this work would not have been possible.

I am especially grateful to the thesis committee members Dr. Wael Mokhtar and Dr. Lindsay Corneal for their technical support and feedback. I want to sincerely thank Dr. Corneal who put a lot of effort to guide me during writing of the thesis paper.

I wish to thank Dr. Shabbir Choudhuri for his motivation and guidance to complete the thesis work within time. I want to extend my gratitude towards the staffs of Padnos College of Engineering and Computing, who supported me at various stages during this work. Special thanks for Md. Maruf Hossain for sharing his experience and providing insightful feedback on the thesis work.

Finally, I want to express my gratitude to my parents, my wife, my brothers and friends who encouraged and supported me throughout the journey of my master study and this thesis work.

Abstract

A parametric investigation was carried out to understand the flow characteristics of tubercle airfoils and to determine the best approach and parameters for designing a tubercle airfoil. For this purpose, a straight edge base airfoil (NACA 4414) and several tubercle airfoils, by modifying the leading edge of the base airfoil, were created in SolidWorks and tested with Computational Fluid Dynamics (CFD) application software Star CCM+.

Alternative tubercle airfoil with elliptical bumps demonstrated superior post-stall performance when compared to their straight edge counterparts; their post-stall lift did not decrease drastically. However, their pre-stall lift coefficients were always lower than the base NACA 4414 airfoil. Alternative tubercle airfoil with spherical bumps at the leading edge showed good agreement with the base NACA 4414 lift curve while providing slightly higher lift coefficients for all tested angles. However, the drag coefficient was also higher for this model which resulted in a poor lift to drag ratio.

Tubercle models with varying amplitude suffered drastically at high angles of attack while also stalling earlier. Early flow separation took place at tubercles with high maximum amplitudes. Gradual increase of lift and stall angle were achieved by lowering the maximum amplitude of tubercles. The varying amplitude model 4414_sin_0.015t_0.4_100 with a maximum amplitude of 1.5% of chord length provided a higher lift to drag ratio than the base airfoil at low angles of attack between 0° and 4°.

Conventional sinusoidal models were created with various magnitudes of amplitude and wavelength. It was found that low amplitude and long wavelength contribute to the best

aerodynamic performance. An additional study found that surface waviness contributes to the enhancement of post stall lift coefficient. Following these parametric studies, an optimal tubercle airfoil (4414_sin_0.6_0.2_100) configuration was identified with a uniform amplitude of 0.6% of chord length and wavelength of 31.4% (0.2 factor) of chord length.

Finally, the effect of Reynolds number on the optimal tubercle airfoil was studied by testing the airfoil at three Reynolds numbers: $1x10^6$, $5x10^6$, $10x10^6$. A trend of increasing lift and a 4° increase of stall angle was observed with the increase of Reynolds number.

Table of Contents

List of Tables

List of Figures

Nomenclature

ρ	Density
u	Velocity components in the x direction
v	Velocity components in the x direction
w	Velocity components in the x direction
p	Static pressure
$\tau_{xx,}$	Normal stress in the x direction
$\tau_{yy,}$	Normal stress in the y direction
$\tau_{zz,}$	Normal stress in the z direction
$\tau_{xy,}$	Shear stress in the x direction
$\tau_{yz,}$	Shear stress in the y direction
$\tau_{zx,}$	Shear stress in the z direction
$f_{x,}$	Body forces in x direction
$f_{y,}$	Body forces in y direction
$f_{z,}$	Body forces in z direction
q	Total heat entered the control volume
k	Thermal conductivity
α	Angle of attack

C_L	Lift Coefficient
L	Lift force
D	Drag Force
V	Velocity of air
A	Projected area
k	Turbulent kinetic energy
ε	Rate of dissipation of turbulent kinetic energy
ω	Specific rate of dissipation of turbulence kinetic energy into internal thermal energy
E_{ij}	Rate of deformation
μ_t	Eddy viscosity

1. Introduction

When an aircraft moves through the air with a given speed, due to the interaction of its airfoil surface with the surrounding air, velocity gradients are developed with the adjacent layers of air. At the airfoil surface the layer of air has zero velocity relative to the solid airfoil boundary. The velocity increases with the increase of distance from the solid boundary and at some point, it reaches the free stream velocity. The vertical distance from any point on the airfoil surface to the point where the velocity reaches 99% of free stream velocity is the boundary layer thickness (DiGiovanni et al., 2018). The forward moving air around the airfoil reaches to a maximum velocity at some point, and at this point the pressure is also the lowest. Thus, up to this point, the air flow encounters a favorable pressure gradient (high to low). Beyond this point, the air encounters an adverse pressure gradient (low to high) since it has to return to atmospheric pressure downstream of the airfoil. If the adjacent layers of air do not have the required energy to overcome the adverse pressure gradient, they will move in the reverse direction. The reverse stream meets the oncoming air and is separated away from the airfoil surface, creating a zone with reverse flows and vortices. This zone is known as the wake zone. For convenience, the point where the reverse flow begins is termed the separation point. Figure 1 shows a combined representation of boundary layer, separation point and wake zone.

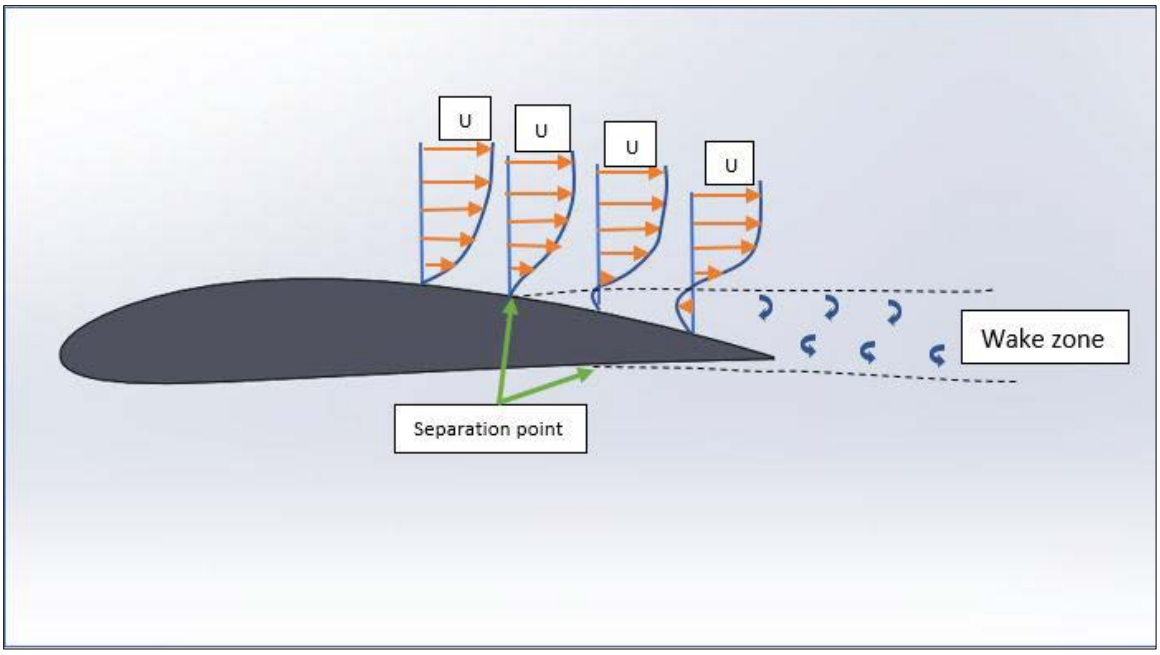

Figure 1: Demonstration of boundary layer separation

A pressure difference is created between the top and bottom surface of the airfoils while the aircraft moves forward. High pressure is developed at the bottom surface, which is called the pressure side, and low pressure is developed at the top surface, which is called the suction side. This pressure difference between the top and bottom surfaces creates the lift force necessary to lift the airfoil. This force is perpendicular to the direction of the oncoming flow. Another active force on the airfoil is drag force, which acts parallel to the flow direction. The pressure imbalance as a result of the wake zone results in a significant increase in form (pressure) drag.

At low angles of attack, flow separation starts at the trailing edge of the airfoil while flow remains attached to the rest of the airfoil. With increasing angle of attack, the separation point moves upstream of the airfoil resulting in a bigger wake zone. If the angle of attack keeps increasing, flow separation starts earlier and the wake zone keeps getting bigger. At some angle of attack, the wake zone will be very large resulting in stall since majority of the airflow is

unable to adhere to airfoil and generate lift. Beyond the stalling point, lift decreases significantly and form drag increases due to large wake zone. The critical or stall angle of attack is the angle at which lift is maximum

Early flow separation is detrimental to the airfoil performance, and several mitigation techniques have been investigated in the literature. Flow separation can be controlled by different active and passive flow control methods to increase lift, stall angle or decrease drag. Active flow control methods involve additional power usage for functioning. Leading edge slats and trailing edge flaps are examples of active flow control. These devices are angled down during the low speed takeoff and landing to increase the camber and wing area, thus increasing the lift. During cruise conditions these slats and flaps are retracted to avoid increased drag (Hansen, 2012). Another active control technique uses a suction method to stabilize laminar flow and delay laminar flow transformation. A vacuum is used to suck the air from the boundary layer region and guide it through narrow slots or channel to the rear side of the airfoil. However, the power requirement for the vacuum is too high if suctions are used over the entire span (Swatton, 2011). Spanwise slots are used as an active control method to pass air from the pressure side to the suction side during takeoff and landing to energize the wake zone air. During cruise conditions the slots are kept closed (Swatton, 2011). Vortex generator jets are used to exchange momentum at the suction side of the airfoil at higher angles of attack. They are positioned near the separation zone and the angle of the jet can be changed (Johnson et al., 2008).

Passive flow control involves either changing the geometry of the airfoil or adding nonmoving objects that do not require additional energy. Examples of passive flow control methods are

vortex generators, serration at the leading edge, turbulators, tubercles, etc. Vortex generators are rectangular or delta shaped winglets with small height, placed on the top surface of the airfoil to create rotating vortices that enhance momentum in the wake zone (Lin, 2002). Similar vortices are generated by serration of the airfoil leading edge just below the stagnation point. These serrations automatically move up at high angles of attack when separation control is necessary (Soderman, 1972). Several bio-inspired passive control methods have gone through extensive research. One of such methods was inspired by birds landing where they lift their suction side feathers up during landing. Movable flaps were used at the trailing edge which moved up during landing and takeoff. These flaps prevented the separation zone from propagating towards the leading edge (Meyer et al., 1999). In another approach comb-like serrated fixtures were used at the airfoil leading edge which is found on the leading edge of owls' wings. The fixtures were applied to an airfoil leading edge and found that vortices were created which delayed stall (Anderson, 1973).

Active flow control methods have advantages such as ability to switch on and off, target specific control, low associated drag, adjustability during flight, etc. But the implementation of active flow controls is often more complex, expensive, not reliable, and requires strict monitoring. The advantage of passive flow control is that it requires less monitoring, usually less complicated, more reliable, and cost effective. Hence research work for finding new passive control techniques are still in great demand.

Humpback whales have a unique feature in their flippers. Their flippers have round protuberances also known as tubercles at the leading edge that give them passive control of fluid flow during turning or banking. With tubercles, the leading edge of the flipper appears as a

sinusoidal curve traveling along the span. Similar to the main two parameters of a sinusoidal curve, these tubercles also have features of amplitude and wavelength. Amplitude is the distance between crest and valley of a tubercle and wavelength is the distance from one crest to the next or one valley to the next. While moving forward under water, the tubercles at the leading edge of the flipper guide the water into two opposite directions along the streamway due to their geometric angle. Water pushed by two adjacent tubercles meet in the area behind the trough and creates vorticity. This vortex increases the kinetic energy of the water, which eventually helps to energize the water at the separation zone to stay attached to the airfoil top surface and thus delays the stall.

Experimental results showed that the flipper model with tubercles increases maximum lift coefficient with the expense of minimum drag increase and helps to delay stall compared to the model with no tubercles. However, not much improvement was observed in the pre-stall lift (Miklosovic et al., 2004). Several other experimental works were carried out later with tubercle airfoils created from the profile of commercial airfoils. As a tubercle airfoil has variables such as amplitude and wavelength, so many variations are possible for their design with many possibilities to improve the aerodynamic efficiency. However, due to the limitation of resources for experiments and difficulty of fabricating complex designs, tubercles were not studied adequately. Computational Fluid Dynamics (CFD) software can be a great tool in this case, for investigating tubercle airfoils' performance, due to their great flexibility and computational power. Although the reliability of experimental investigation is always higher than that of numerical analysis, with careful selection of appropriate CFD solver and correct boundary

conditions, numerical analysis can give accurate results. In addition, the different post-processing tools of CFD software help to efficiently analyze results and help to find solutions.

2. Literature Review

One of the very first numerical analysis on tubercle-featured airfoils was carried out by Watts et al. (2001). They simulated a tubercle-featured wing and a straight leading-edge wing for a single angle of attack at 10° with inviscid simulation and compared the two results. A 3D panel method code, based on first order vortex, was employed to solve the simulation. The airfoil chord length was 17.6 cm with a free stream velocity of 1 m/s, which is basically a very low Reynolds number (Re). For the tubercle leading edge airfoil, they found a lift coefficient of 0.456 and drag coefficient of 0.0501, while for the straight leading-edge wing the lift and drag coefficients were 0.435 and 0.0562, respectively. Hence, a total of 4.8% increase in lift, a 10.9% reduction in induced drag, and a 17.6% increase in lift to drag ratio were obtained.

Miklosovic et al. (2004) have shown by wind tunnel testing that the flipper of a humpback whale with sinusoidal tubercles delays stall angle by 40% compared to an idealized flipper with no tubercles. For the purpose of simulating hydrodynamic flow around the airfoils, their test was performed in a low speed closed circle wind tunnel with Reynolds number ranging from $5.05x10^5 – 5.20x10^5$ in an incompressible steady state flow environment. Lift coefficients between angles of attack of 9.3° and 12° were found to be lower for tubercle flipper, but for all other angles, the lift was higher than that of the smooth flipper. The maximum angle of attack (stall angle) achieved by their tubercle flipper was 16.3° while that for the smoothed-edge flipper was 12°. The drag coefficient was observed to be less than that of the smooth model for all angles of attack beyond 12°. The maximum lift to drag ratio was reduced slightly, but the ratio was higher for scalloped (tubercle) models at all other angles. Therefore, the scalloped flipper performed better at most points, especially at high angles of attack.

In a later experiment, Miklosovic et al. (2007) conducted a wind tunnel study with a full span tubercle model and a base model, where they observed detrimental effects by tubercles. A low lift coefficient and high drag coefficient were observed in the pre-stall region, which was caused by early flow separation due to the tubercles. However, in the post stall region the tubercle model showed higher lift coefficients than the base model.

Nierop et al. (2008) proved by an aerodynamic model of a humpback flipper that tubercles do not increase lift coefficient, although they flatten the lift curve by making gradual declination of the lift after stall. Increasing amplitudes of tubercle bumps was found to help the increase of stall angle. They found a very small improvement of 0.1% for the lift to drag ratio for short wavelength airfoils, and in most cases, it was insensitive to wavelength variation. They concluded that the trough region stalls early, which was observed by manometer readings from the experiments, and this is the reason tubercles cause lower lift than straight airfoils.

In 2011, Weber et al. conducted numerical studies to understand the flow physics of a tubercle model. For this purpose, they used one tubercle model and one simplified model and analyzed them with two different simulation software, Star CCM+ and SolidWorks Flow Simulation (SFS) 2009. Star CCM+ results were in good agreement with experimental results from the pre-stall region, while SFS provided better agreement in the post-stall region. Spalart-Allmaras turbulent model provided the best results for pre-stall angles and K-ω model performed better for post-stall angles. Flow visualization confirmed trailing edge stall for the simplified model while the tubercle model had stall at the leading edge at the trough between two tubercles.

In the same year as Weber et al., Hansen et al. (2011) performed an experimental investigation on two airfoils, NACA 65-021 and NACA 0021, to study performance variation due to the sinusoidal leading-edge modification. The tubercle airfoil for NACA 65-021 was found to be more beneficial than the tubercle airfoil for NACA 0021. They applied combinations of amplitude and wavelength on a full span airfoil to observe their effect on aerodynamic performance. It was found that smaller amplitudes were more beneficial than larger amplitudes for the pre-stall region while for the post stall region larger amplitudes were better. Similarly, smaller wavelengths of tubercles were also found beneficial over larger wavelengths. Their experiments were performed for a Reynolds number of 1.2×10^5 with a mean chord length of 70 mm and span of 495 mm.

Lohry et al. (2012) carried out a computational study to validate a Reynolds-averaged Navier Stokes (RANS) approach that was developed at Princeton University for the analysis of tubercle geometry in the Re range of $6.25 \times 10^4 – 5 \times 10^5$. They used a NACA 0020 geometry that Miklosovic et al. (2007) used for experimental analysis but used a straight span instead of variation in span length to decouple the effect of span loading. They developed the tubercle model by varying the leading edge of NACA 0020 with a sinusoidal curve. The results of their simulation were then compared with the experimental results from Miklosovic et al. (2007) even though the geometry along the span was different from that of Miklosovic et al. The new results showed that the RANS approach with a Menter SST turbulence model closely matched the experimental results of Miklosovic et al. However, the after-stall characteristics had a large deviation. They suggested that tubercles made by chord variations act as vortex generators,

which break up separation regions and create span wise fences, that can increase maximum lift. This was an important conclusion.

Rostamzadeh et al. (2013) employed Prandtl's nonlinear lifting line theory to form a hypothesis that favorable traits are observed by some other methods as an alternative to tubercles at the leading edge of the wing. One wavy model with geometrically varying angle of attack along the span and one tubercle model with only a sinusoidal leading edge were developed. Using the Prandtl's lifting line theory, they found the wavy model had higher flow circulation. Four airfoils with a wavy span were then modeled and fabricated for wind tunnel testing to measure pressure and force. Chordwise Reynolds number of the models was $1.2x10^5$ for a mean chord length of 70 mm and wind tunnel stream velocity of 25 m/s. Of the four wavy airfoils, three showed gradual stall, which is analogous to the behavior of the tubercle wings. Among the three, one model with the highest peak-to-peak angular amplitude and smallest wavelength showed the best post-stall behavior. They also conducted a CFD investigation on the wavy airfoil and observed similar results when compared to experimental data except for post-stall angles of attack. They suggested that this discrepancy in the simulation result can be avoided with a higher order simulation tool for turbulent flow. In a subsequent study in 2014, they investigated the mechanism of vortex formation over the full span of the tubercle airfoil and observed that counter rotating stream wise vortices were formed along the span from leading edge to trailing edge at all angles of attack, thus improving post-stall behavior. This observation was in agreement with Lohry et al. (2012).

Fernandes et al. (2013) investigated the effect of tubercles on a NACA 2412 airfoil by Numerical analysis using ANSYS. They also made sinusoidal tubercle models with combinations of

amplitude and wavelengths for a Reynolds number 2.185 x 10^6. They found no pre-stall enhancements of aerodynamic performance. According to their study, larger amplitudes with smaller wavelengths contributed to the best performance enhancements with a 5.33% lift increase and 2.72% drag reduction.

Experimental studies were conducted on two swept back wings by Bolzon et al. (2016), one with a tubercle leading edge and one with a smooth leading edge to compare vortices produced by tubercles for angles of attack of 0°, 3°, 6°, 9° and 12°. Asymmetry was observed in the strength of vortices generated by a single tubercle on the tubercle wing. Increase in strength of tubercle vortices was observed with increasing angle of attack. They found that below an angle of attack of 6°, the profile drag reduced while the induced drag remained largely unchanged for the tubercle wing. However, above an angle of attack of 9°, the profile drag increased significantly while the induced drag decreased.

Bolzon at al. (2017) investigated the effect of a single tubercle of amplitude 10.5 mm and 60 mm terminating at the swept wing's tip for the pre-stall region. Flow visualization wake surveys and force measurements were conducted for various angles of attack. For small angles of attack of 1° and 2°, tubercles reduce the lift coefficient and hence the lift to drag ratio by 3%. Between 3° and 15°, the lift coefficient and lift to drag ratio remained unchanged when compared to the non-tubercled counterpart. A summary of the findings from the literature that has been reviewed is presented in Table 1.

Table 1: Summary of Literature Review

Paper	Year	Study Type	Base Model	Description	Reynolds No.	Findings	
						Advantage	Disadvantage
Watts, P., & Fish, F. E. (2001, August)	2001	Numerical	Whale Flipper	C = 176 mm S =359 mm		At AOA 10° 4.8% CL increase and 10.9% CD reduction and 17.6% CL/CD increase	
Miklosovic, D. S., Murray, M. M., Howle, L. E., & Fish, F. E. (2004)	2004	Experimental	Whale Flipper /NACA 0020	C = 161.9 mm S =565.2 mm	$5.05x10^5$ - $5.20x10^5$	delays the stall angle by approximately 40%, increase lift and decrease drag	
Miklosovic, D. S., Murray, M. M., & Howle, L. E. (2007).	2007	Experimental	Whale Flipper /NACA 0020	Full span C = 3.438 in S =11.313 in Semi span C = 5.539 in S = 22.5 in	$2.74x10^5$ - $2.77x10^5$	Semi span - Maximum Cl increase 4%, Stall angle 5 degree	Full span- above 8 degAOA 16% less Cl and 17% less L/D, increased Cd for 7 deg < α < 16 deg
Carreira Pedro, H., & Kobayashi, M. (2008, January)	2008	Numerical	Whale Flipper	C = 127 mm S = 562.5 mm	<5x10^5	Higher aerodynamic performance for the scalloped flipper	
Van Nierop, E. A., Alben, S., & Brenner, M. P. (2008)	2008	Experimental	Whale Flipper & NACA-0018			1. Lift curve flaten after stall. 2. Higher overall stall angle	1. Maximum lift decreases 2. No significant improvement in L/D ratio even after stall
Weber, P. W., Howle, L. E., Murray, M. M., & Miklosovic, D. S. (2011)	2011	Numerical analysis of experiment of Miklosovic by Star CCM & SFS	Whale Flipper	C = 130.5 mm S = 560.7 mm	$5.05x10^5$ - $5.20x10^5$	Star CCM found good match for prestall regime and Solidwork for post stall regime	
Hansen, K. L., Kelso, R. M., & Dally, B. B. (2011)	2011	Experimental	NACA 65-021 NACA 0021	C = 70 mm S =495 mm	$1.2x10^5$	1. Reducing tubercle amplitude give higher maximum Cl and larger stall angle. 2. Reducing wavelength improves maximum Cl, 3. NACA 65021 performs better than NACA 0021 for tubercles	
Fernandes, I., Sapkota, Y., Mammen, T., Rasheed, A., Rebello, C., & Kim, Y. H. (2013)	2013	Experimental	NACA 2412	C = 1 m S =5 m	$2.185×10^6$	1. Enhance after stall CL behavior 2. with larger amplitude and smaller wavelength 5.33% CL increase and 2.72% drag reduction in post stall region	
Lohry, M. W., Clifton, D., & Martinelli, L. (2012, July)	2012	computational study	Whale Flipper /NACA 0020		$6.25x10^4$ - $5x10^5$	RANS approach succesfully captured applied the analysis of tubercle wing	
Hansen, K. L. (2012)	2013	Experimental	NACA 65-021 NACA 0021	C = 70mm S =495mm	$1.2x10^5$	1. Lift increased at post stall region 2. Mitigate tonal noise 3. Smallest amp;itude and wavelength tubercles performed best	1. Degraded lift performance in the prestall region
Rostamzadeh, N., Kelso, R. M., Dally, B. B., & Hansen, K. L. (2013)	2013	Experimental/ Numerical	Wavy airfoils based on NACA0021	C = 70mm S =495mm	$1.2x10^5$	1. highest peak-to-peak angular amplitude and smallest wavelength gave best post stall lift	

Table 1 continued

Paper	Year	Study Type	Base Model	Description	Reynolds No.	Findings	
						Advantage	Disadvantage
Rostamzadeh, N., Hansen, K. L., Kelso, R. M., & Dally, B. B. (2014)	2014	Experimental /CFD Study	Three airfoil model based on NACA 0021	C = 70 mm S= 495 mm	$1.2x10^5$	Give benefits post-stall behavior	Vortices are detrimental to the performance of full-span wings pre-stall
Zhang, M. M., Wang, G. F., & Xu, J. Z. (2014)	2014	Experimental	NACA634-021	C = 100 mm S = 350 mm	$2x10^5$	1. increases CL, and L/D, by as much as 54.5 and 67.7 %, 2. decreases CD and Cm, by as much as 6.70 and 11.1 %, in the post-stall AOA of 22 –80	For AOA 7-21 , CL and L/D becomes lower than base
Bolzon, M. D., Kelso, R. M., & Arjomandi, M. (2016)	2016	Experimental	Swept NACA 0021 airfoil	C_{max} = 175 mm S = 330 mm	$2.25x10^5$	AOA 6◦ and below the tubercled wing reduced the profile drag coefficient	AOA 9◦ onwards tubercled wing increased the profile drag coefficient
Ng, B. F., New, T. H., & Palacios, R. (2016)	2016	Numerical	Goland Wing	C = 1.83 m S =6.10 m	Not mentioned	1. Flutter speed 5% higher 2. 6%decrease in reduced frequencies 3. low structural stiffness required	Smaller effects on flutter speeds as the sweep angle is increased for swept airfoil
Wei, Z., Zang, B., New, T. H., & Cui, Y. D. (2016)	2016	Experimental	NACA634-021	C = 75 mm S = 300 mm	$1.4x10^4$		Causes unsteadiness of span wise flow

From the literature, it can be summarized that, most of the studies covered tubercle featured airfoils with uniformly distributed sinusoidal designs at the leading edge. Tubercles with varying amplitude and wavelength were not covered in these studies for lift and drag improvement. There were gaps in information about the tubercles' potential as tubercle airfoil with varying amplitude and wavelength were left uninvestigated. Moreover, previous studies were based on only the sinusoidal leading-edge type. More alternative models can be designed, taking into consideration the basic working principle of tubercles. In one of the papers of Hansen et al. (2011), they proposed that other alternative forms of tubercle design can also be studied to find out the potential aerodynamic advantage. Rostamzadeh et al. (2014) investigated wavy body design in one of their studies and found that they also give lift enhancement like tubercles

at the leading edge. A combination of sinusoidal tubercle with wavy span can be used to model a tubercle airfoil. In addition, the effect of Reynolds number on the performance of straight airfoil wings were studied earlier, but the effect of Reynolds number on tubercle airfoils were not studied; the Reynolds numbers were in the low range. To gain a better appreciation about the effect of tubercles on airfoil aerodynamic performance and selection of optimal combination, all possible areas should be investigated.

3. Scope of Present Work

The present work focused on the investigation of different approaches to create tubercle airfoils and their performance compared to a base airfoil. The base airfoil for this purpose was selected as a NACA 4414 airfoil, which is a custom airfoil with a maximum camber of 4.3% of chord located at 40% chord length, a maximum thickness of 14%, and 151 points. The profile of a NACA 4414 airfoil is shown in Figure 2 with representation of the camber line and chord line.

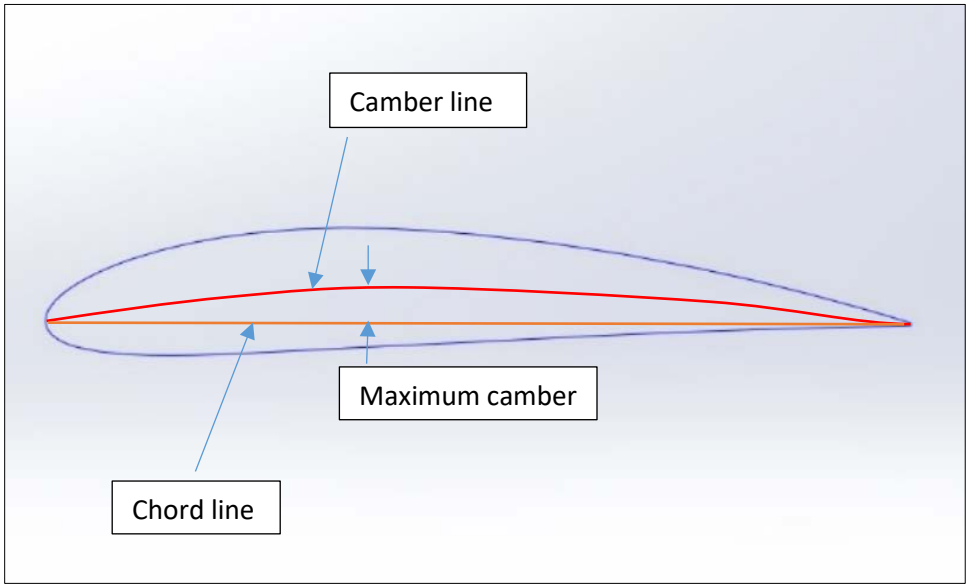

Figure 2: NACA 4414 profile with camber line and chord line

Different types of airfoil models were created by modifying the leading edge of the base NACA 4414 airfoil. Beside conventional sinusoidal tubercles, some tubercle airfoils were created with a non-sinusoidal leading edge as part of the alternative approaches. These alternative tubercle airfoils were then analyzed by running simulations to observe performance changes from the base airfoil. Sinusoidal airfoils with and without surface waviness were created and tested to measure the effect of surface waviness on tubercle airfoil performance. Then, sinusoidal tubercle airfoils with different wavelengths and amplitudes (constant and varying) were

modeled based on the NACA 4414 to observe key variables responsible for performance variation and optimum combination of those variables. Finally, a tubercle airfoil was developed using the information obtained from the study with the best approach and optimum combination of the variables. This airfoil was then tested for different Reynolds number to evaluate the effect of Reynolds number on tubercle airfoils. The uniqueness of this study was that it covered investigation of tubercles created with some alternative approaches and sinusoidal models with varying amplitude and wavelength, which have not been extensively studied. In addition, limited data is available for effects of high Reynolds number on tubercle airfoils' performance; this study added to this as well. A summary of the scope of this work is provided below.

1. Recreated Clark-Y airfoil to determine appropriate physics model and boundary conditions by matching published data; i.e. verify numerical setup.
2. Checked mesh independence by using Clark Y airfoil.
3. Recreated and simulated the base NACA 4414 airfoil to obtain data of lift coefficient and drag coefficient by applying the appropriate physics model.
4. Created alternative tubercle airfoils based on the NACA 4414 airfoil.
5. Evaluated lift and drag coefficient values for various angles of attack on the alternative tubercle models.
6. Created tubercle airfoils with sinusoidal leading edge with constant and varying amplitude and different wavelengths based on the NACA 4414 airfoil.
7. Evaluated lift and drag coefficient values for sinusoidal leading-edge tubercle airfoils.
8. Investigated the effect of a wavy surface on tubercle airfoils.

9. Determined the best approach to develop optimum tubercle geometry and tested it.
10. Investigated the effect of Reynolds number by testing a tubercle airfoil for various Reynolds number.

4. Theoretical Background

In Computational Fluid Dynamics, there are three conservation laws that are the base of numerical solutions. The three laws are conservation of mass, momentum, and energy, which are also called governing equations.

4.1 Conservation of Mass

All numerical simulations must satisfy the conservation of mass principle for solving a numerical problem. According to the conservation of mass principle, for a control volume, the rate at which mass enters the system is equals to the rate at which mass leaves the system plus rate of accumulation of mass in the region. The conservation of mass principle can be written in the form of a differential equation which is shown in Equation 1.

$$\frac{\partial \rho}{\partial t} + \frac{\partial (\rho u)}{\partial x} + \frac{\partial (\rho v)}{\partial y} + \frac{\partial (\rho w)}{\partial z} = 0 \qquad (1)$$

Where,

ρ is density.

u, v and w are velocity components in the x, y, and z directions, respectively.

For steady-incompressible flow, Equation 1 becomes:

$$\frac{\partial u}{\partial x} + \frac{\partial v}{\partial y} + \frac{\partial w}{\partial z} = 0 \qquad (2)$$

4.2 Conservation of Momentum

The conservation of momentum is based on Newton's second law, F=ma. In fluid dynamics, two types of forces act on a control volume of fluid, namely body forces and surface forces. The body forces act directly on the mass of the control volume, such as gravity and electromagnetic forces. Surface forces act on the surfaces and are a result of pressure distribution and normal and shear stress distribution on the surfaces. Equations 3, 4, and 5 are general forms of conservation of momentum equations in the x, y, and z directions, respectively.

$$\frac{\partial(\rho u)}{\partial t}+\frac{\partial(\rho uu)}{\partial t}+\frac{\partial(\rho vu)}{\partial t}+\frac{\partial(\rho wu)}{\partial t}=-\frac{\partial p}{\partial x}+\frac{\partial \tau_{xx}}{\partial x}+\frac{\partial \tau_{xy}}{\partial y}+\frac{\partial \tau_{zx}}{\partial z}+\rho f_x \quad (3)$$

$$\frac{\partial(\rho v)}{\partial t}+\frac{\partial(\rho uv)}{\partial t}+\frac{\partial(\rho vv)}{\partial t}+\frac{\partial(\rho wv)}{\partial t}=-\frac{\partial p}{\partial y}+\frac{\partial \tau_{xy}}{\partial x}+\frac{\partial \tau_{yy}}{\partial y}+\frac{\partial \tau_{zy}}{\partial z}+\rho f_y \quad (4)$$

$$\frac{\partial(\rho w)}{\partial t}+\frac{\partial(\rho uw)}{\partial t}+\frac{\partial(\rho vw)}{\partial t}+\frac{\partial(\rho ww)}{\partial t}=-\frac{\partial p}{\partial z}+\frac{\partial \tau_{xz}}{\partial x}+\frac{\partial \tau_{yz}}{\partial y}+\frac{\partial \tau_{zz}}{\partial z}+\rho f_z \quad (5)$$

Where

ρ is density.

p is static pressure.

u, v and w are velocity components in the x, y, and z directions, respectively.

τ_{xx}, τ_{yy}, and τ_{yy} are normal stresses in the x, y, and z directions, respectively.

τ_{xy}, τ_{yz}, and τ_{zx} are the shear stresses in the x, y, and z directions, respectively.

f_x, f_y, and f_z are body forces in x, y, and z directions, respectively.

4.3 Navier-Stokes Equation

Equations 3, 4, 5 are also called the Navier-Stokes equation in the conservation form. For Newtonian fluids, Stokes developed Equations 6 – 11 for the stress components.

$$\tau_{xx} = \lambda(\frac{\partial(\mathrm{u})}{\partial \mathrm{x}} + \frac{\partial(\mathrm{v})}{\partial \mathrm{y}} + \frac{\partial(\mathrm{w})}{\partial \mathrm{z}}) + 2\mu \frac{\partial \mathrm{u}}{\partial \mathrm{x}} \quad (6)$$

$$\tau_{yy} = \lambda(\frac{\partial(\mathrm{u})}{\partial \mathrm{x}} + \frac{\partial(\mathrm{v})}{\partial \mathrm{y}} + \frac{\partial(\mathrm{w})}{\partial \mathrm{z}}) + 2\mu \frac{\partial \mathrm{v}}{\partial \mathrm{y}} \quad (7)$$

$$\tau_{zz} = \lambda(\frac{\partial(\mathrm{u})}{\partial \mathrm{x}} + \frac{\partial(\mathrm{v})}{\partial \mathrm{y}} + \frac{\partial(\mathrm{w})}{\partial \mathrm{z}}) + 2\mu \frac{\partial \mathrm{w}}{\partial \mathrm{z}} \quad (8)$$

$$\tau_{xy} = \tau_{yx} = \mu(\frac{\partial \mathrm{v}}{\partial \mathrm{x}} + \frac{\partial \mathrm{u}}{\partial \mathrm{y}}) \quad (9)$$

$$\tau_{xz} = \tau_{zx} = \mu(\frac{\partial \mathrm{u}}{\partial \mathrm{z}} + \frac{\partial \mathrm{w}}{\partial \mathrm{x}}) \quad (10)$$

$$\tau_{yz} = \tau_{zy} = \mu(\frac{\partial \mathrm{w}}{\partial \mathrm{y}} + \frac{\partial \mathrm{v}}{\partial \mathrm{z}}) \quad (11)$$

Where

μ is the molecular viscosity coefficient,

λ is the second viscosity coefficient,

and λ = -2μ/3.

Now, substituting Equations 6 – 11 into Equations 3, 4, and 5 gives the complete Navier-Stokes equations in conservation form for compressible fluid, shown in Equations 12, 13, and 14.

$$\frac{\partial(\rho u)}{\partial t}+\frac{\partial(\rho uu)}{\partial t}+\frac{\partial(\rho vu)}{\partial t}+\frac{\partial(\rho wu)}{\partial t}=-\frac{\partial p}{\partial x}+\frac{\partial}{\partial x}(\lambda(\nabla.V)+2\mu\frac{\partial u}{\partial x})+\frac{\partial}{\partial y}(\mu(\frac{\partial v}{\partial x}+\frac{\partial u}{\partial y}))+$$

$$\frac{\partial}{\partial z}(\mu(\frac{\partial u}{\partial z}+\frac{\partial w}{\partial x}))+\rho f_x \quad (12)$$

$$\frac{\partial(\rho v)}{\partial t}+\frac{\partial(\rho uv)}{\partial t}+\frac{\partial(\rho vv)}{\partial t}+\frac{\partial(\rho wv)}{\partial t}=-\frac{\partial p}{\partial y}+\frac{\partial}{\partial x}(\lambda(\nabla.V)+2\mu\frac{\partial u}{\partial x})+\frac{\partial}{\partial y}(\mu(\frac{\partial v}{\partial x}+\frac{\partial u}{\partial y}))+$$

$$\frac{\partial}{\partial z}(\mu(\frac{\partial u}{\partial z}+\frac{\partial w}{\partial x}))+\rho f_x \quad (13)$$

$$\frac{\partial(\rho w)}{\partial t}+\frac{\partial(\rho uw)}{\partial t}+\frac{\partial(\rho vw)}{\partial t}+\frac{\partial(\rho ww)}{\partial t}=-\frac{\partial p}{\partial z}+\frac{\partial}{\partial x}(\lambda(\nabla.V)+2\mu\frac{\partial u}{\partial x})+\frac{\partial}{\partial y}(\mu(\frac{\partial v}{\partial x}+\frac{\partial u}{\partial y}))+$$

$$\frac{\partial}{\partial z}(\mu(\frac{\partial u}{\partial z}+\frac{\partial w}{\partial x}))+\rho f_x \quad (14)$$

4.4 Conservation of Energy

The rate of change of energy inside the control volume is equal to the net flux of heat into the control volume plus the rate of work being done on the element due to body and surface forces. This is the principle of conservation of energy and can be written as shown in Equation 15.

$$\rho\frac{De}{Dt}=\rho q+\frac{\partial}{\partial x}\left(k\frac{\partial T}{\partial x}\right)+\frac{\partial}{\partial x}\left(k\frac{\partial T}{\partial x}\right)+\frac{\partial}{\partial x}\left(k\frac{\partial T}{\partial x}\right)-p\left(\frac{\partial u}{\partial x}+\frac{\partial v}{\partial y}+\frac{\partial w}{\partial z}\right)+\tau_{xx}\frac{\partial u}{\partial x}+\tau_{yz}\frac{\partial u}{\partial y}+$$

$$\tau_{zx}\frac{\partial u}{\partial z}+\tau_{xy}\frac{\partial v}{\partial x}+\tau_{yy}\frac{\partial v}{\partial y}+\tau_{zy}\frac{\partial v}{\partial z}+\tau_{xz}\frac{\partial w}{\partial x}+\tau_{yz}\frac{\partial w}{\partial y}+\tau_{zz}\frac{\partial w}{\partial z} \quad (15)$$

Equation 15 is the energy equation in terms of internal energy e.

Where,

ρ is density.

u, v, and w are velocity components in the x, y, and z directions, respectively.

τ_{xx}, τ_{yy}, and τ_{zz} are normal stresses in the x, y, and z directions, respectively.

τ_{xy}, τ_{yz}, and τ_{zx} are the shear stresses in the x, y, and z directions, respectively.

f_x, f_y, and f_z are body forces in x, y, and z directions, respectively.

p is the static pressure force exerted on the surfaces.

q is the total heat entering the control volume.

k is the thermal conductivity.

4.5 Definitions

Some important terms are used in this study frequently. Understanding those terms is necessary for better comprehension of the objectives and outcome of the study. In this chapter, some commonly used terms are explained briefly.

Angle of attack (α): It is the angle between the vector direction of incoming flow and a reference line of the airfoil. Usually, the reference line is the chord line, which is the imaginary line that connects the leading edge and the trailing edge.

Lift Coefficient (C_L): When an aircraft moves through the air with a given speed and angle of attack, pressure difference is created on the top and bottom surfaces of the airfoil. High pressure is developed at the bottom surface and low pressure at the top surface. This pressure difference between the top and bottom surface creates lift to the airfoil. The lift coefficient depends on the velocity of the aircraft (V), density of surrounding air (ρ), planform area (A), and angle of attack (α). It is a dimensionless quantity and can be written in the form as in Equation 16.

$$C_L = \frac{L}{(\rho.\frac{V^2}{2}.A)} \quad (16)$$

Drag Coefficient (C_D): While moving through the air the aircraft faces resistive drag forces such as friction drag, pressure drag, lift induced drag. The drag coefficient is a dimensionless quantity that is used to quantify the drag forces that act on an object in a fluid environment. Equation 17 defines drag in terms of dependable parameters. The area here is still the planform area.

$$C_D = \frac{D}{(\rho.\frac{V^2}{2}.A)} \quad (17)$$

Lift to Drag Ratio: It is also a dimensionless quantity which is simply the ratio of the lift coefficient and drag coefficient. The significance of this ratio is that it defines the aerodynamic efficiency of an object moving through a fluid.

4.6 Turbulent Models

It is believed that the Navier-Stokes equation can describe turbulence properly. However, the numerical solution of the Navier-Stokes equation is very difficult. Laminar solvers result in unsteady solutions for solving turbulent flow. Hence, the Reynolds-averaged Navier-Stokes (RANS) approach is used to solve turbulent flow in commercial CFD software. Spalart-Allmaras, k epsilon (k-ε), k-omega (k-ω), and SST models are some common models used for solving turbulent flow in CFD software. The K-ε model is a commonly used model for solving turbulent flow problems. It is a model of two equations with two variables, k and ε. The first variable k is the turbulent kinetic energy and the second variable is the rate of dissipation of turbulent kinetic energy.

Equation 18 shows the formula for kinetic energy, k.

$$\frac{\partial(\rho \mathrm{k})}{\partial \mathrm{t}}+\frac{\partial(\rho \mathrm{k} u_i)}{\partial \mathrm{x}_i}=\frac{\partial}{\partial \mathrm{x}_j}\left[\frac{\mu_t}{\sigma_k}\frac{\partial \mathrm{k}}{\partial \mathrm{x}_j}\right]+2\mu_t E_{ij}E_{ij}-\rho\varepsilon \quad (18)$$

Equation 19 shows the formula for dissipation of kinetic energy, ε.

$$\frac{\partial(\rho \varepsilon)}{\partial \mathrm{t}}+\frac{\partial(\rho \varepsilon u_i)}{\partial \mathrm{x}_i}=\frac{\partial}{\partial \mathrm{x}_j}\left[\frac{\mu_t}{\sigma_\varepsilon}\frac{\partial \varepsilon}{\partial \mathrm{x}_j}\right]+\mathrm{C}_{1\varepsilon}\frac{\varepsilon}{k}2\mu_t E_{ij}E_{ij}-C_{2\varepsilon}\rho\frac{\varepsilon^2}{k} \quad (19)$$

Where,

u_i is the velocity component in the corresponding axis,

E_{ij} is the rate of deformation,

μ_t is the eddy viscosity,

such that $\mu_t = \rho C_\mu k^2/\varepsilon$

Following are the values of four constants that are used in Equation 18 and 19

C_μ=0.09, σ_k = 1.0, σ_ε = 1.30, $C_{1\varepsilon}$=1.44, $C_{2\varepsilon}$=1.44

5. Methodology

For the purpose of this study, a NACA 4414 airfoil was recreated and tested to determine its aerodynamic characteristics such as lift and drag coefficients. Then, tubercle geometry of different types was modeled on the base NACA 4414 airfoil profile and tested with CFD software while maintaining similar boundary conditions for all models. The whole process was done in several steps such as CAD modeling, mesh set up, physics model set up, applying boundary conditions, running simulations, and post processing. In the following sub sections of this chapter, these steps are discussed briefly.

5.1 CAD Modeling

Many Computer Aided Design (CAD) models were created for this study. All the models were not tested, and all the tested models were not reported here. CAD models were created using SolidWorks solid model and surface model tools. NACA 4414 was the base airfoil for this study. Data points of the NACA 4414 airfoil were imported into SolidWorks to create a boundary curve for the NACA 4414 airfoil. This curve was then scaled by multiplying by an appropriate value so that the chord length was 100 millimeters. The scaled curve was then extruded in the direction normal to the sketch plane XY to create a 3D model with a 100 mm span length. This model is shown in Figure 3.

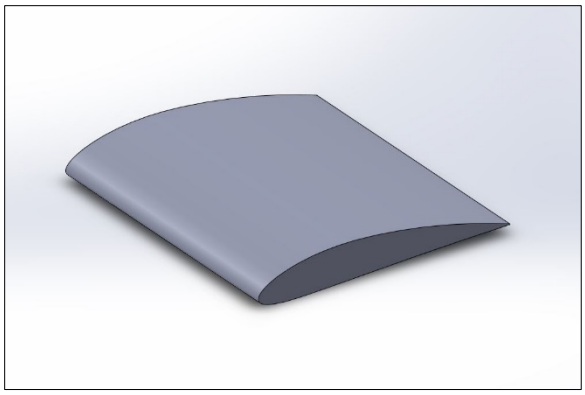

Figure 3: NACA 4414 airfoil

Based on the base NACA 4414 airfoil, several tubercle models of different types were created by modifying the leading edge. All the created tubercle models were grouped into some distinctive types. Images for each category can be found below as well.

a. Alternative non-sinusoidal tubercle airfoil
b. Uniform amplitude sinusoidal airfoil with chordwise wave
c. Uniform amplitude sinusoidal airfoil without chordwise wave
d. Uniform amplitude sinusoidal airfoil with top surface chordwise wave
e. Varying amplitude sinusoidal airfoil with chordwise wave

A few approaches were used for creating alternative non-sinusoidal tubercle models. One of the approaches was to create elliptical tubercles at the upper front side of the airfoil body. The model 4414_Tubercle1_25 was created by this approach which can be seen in Figure 4. The ellipses started at the leading edge and ended at 20% of the chord length distance from the leading edge. The maximum height of the ellipse was 5% of the chord length and all three elliptical tubercles were the same height. The model was created with a 25 mm span length.

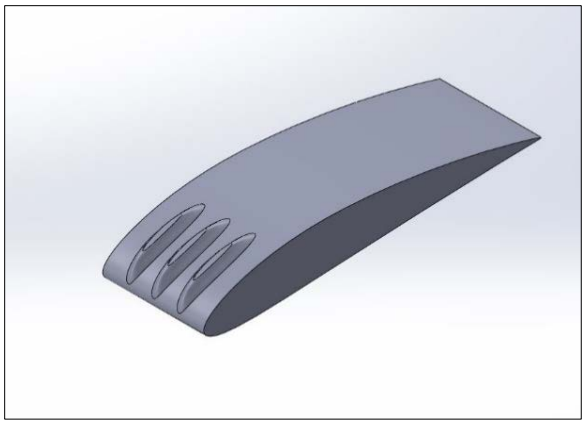

Figure 4: 4414_Tubercle1_25

Figure 5 shows model 4414_Tubercle4_50, which was created with bumps like tubercles at the leading edge, but unlike the sinusoidal type it had no curved valley. Instead, between the turbercles was the straight edge of the base NACA airfoil profile. The model had two bumps with a spacing of 10 mm between them. The bumps had a maximum height of 4.9% of the chord length and 10 mm width. The span was 50 mm. The model was created using the surface loft tool.

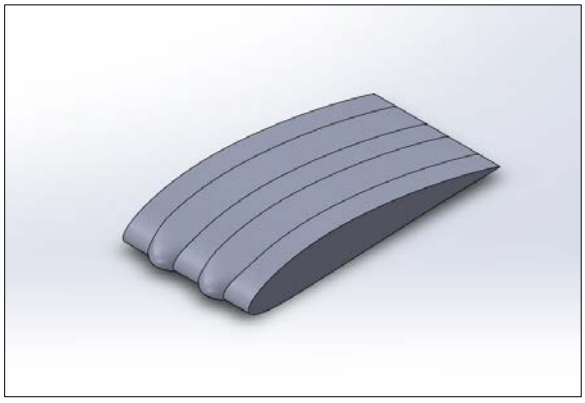

Figure 5: 4414_Tubercle4_50

For tubercle models of sinusoidal leading edge, a sine or cosine curve was created at the leading edge using the equation driven curve tool in SolidWorks. Two NACA 4414 base airfoil

curves were drawn at two ends of the sinusoidal curve. For generating the airfoil surface using the surface loft tool, two base 4414 curves at two ends of the sine curve were selected as profiles and the sine curve at the leading edge and a straight line at the trailing edge were selected as guide curves. A wavy pattern was created at both the top and bottom surfaces of the airfoil that was carried to the trailing edge.

Equations 20, 21, and 22 are the general form of parametric equations that were used for generating the sinusoidal curves to generate sinusoidal leading edges with constant amplitude and wavelength.

$$\mathbf{X_t = m.\sin(n.t)} \quad (20)$$

$$\mathbf{Y_t = 0} \quad (21)$$

$$\mathbf{Z_t = t} \quad (22)$$

Where, $t_1 < t < t_2$.

m is the integer or decimal value of amplitude in millimeters.

n is the integer or decimal value that determines the frequency or wavelength in millimeters.

t is the parametric variable which requires a lower range t_1 and upper range t_2. The difference between t_1 and t_2 is the length of the span.

Equation 20 is the main function that controls the behavior of the sinusoidal curve. In Equation 21, Y_t is equal to zero because it is redundant for the two-dimensional curve that was created in the XZ plane. Every term in Equation 20 has its significance on the development of the

sinusoidal curve. For example, Equation 23 was used to create the sinusoidal profile at the leading edge for model 4414_sin_1_0.4_s_100.

$$\mathbf{X_t = 1.0 * \sin(0.4 * t)} \quad (23)$$

In Equation 23, the value 1.0 before the sine function indicates that the amplitude of the sine curve is one millimeter for this model. The value 0.4 inside the parenthesis of the sine function determines the wavelength of the curve. For this model, the lower limit value of t_1 was set to 0 and the upper limit t_2 was set to 100, hence, the span length for this model was 100 mm. Naming of sinusoidal tubercle models were developed from the first equation of the parametric curve function for leading edge curve. As an example, the meanings of different terms in the name of model 4414_sin_1_0.4_100, where Equation 23 was the leading-edge curve equation, are shown in Table 2.

Table 2: Naming convention for 4414_sin_1_0.4_100 model

Term	Stands For
4414	Base airfoil NACA 4414
sin	The leading-edge curve is drawn using sine function
1	Amplitude of sine curve is 1% of chord
0.4	Multiplying factor to determine the wavelength
100	Span length is 100 millimeters

The amplitude of the tubercle was the distance between the crest and the trough of a sinusoidal tubercle profile. On the other hand, the wavelength was the distance between one

peak to the next peak or one crest to the next crest. The span length was the distance from one root to the next root. Amplitude, wavelength and span of a typical tubercle airfoil are shown in Figure 6.

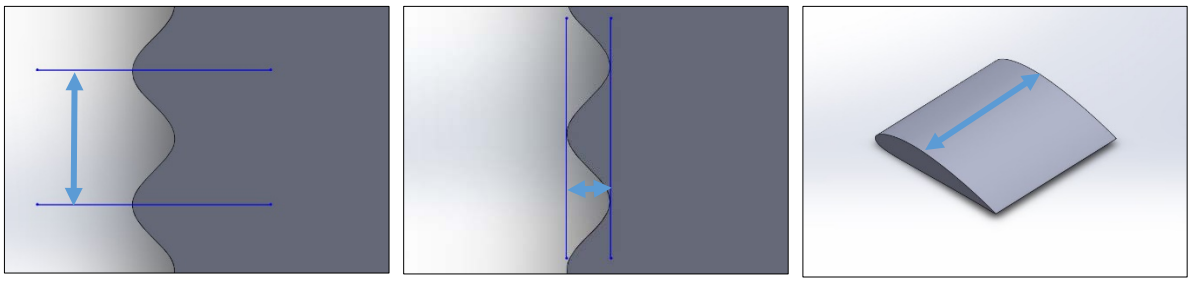

Figure 6: Left (Wavelength), Middle (Amplitude), Right (Span length)

4414_sin_1_0.4_150, which is shown in Figure 7, was the first sinusoidal model with uniform amplitude and wavelength that was created for testing. This model had a span length of 150 mm and it was the only model with this span length.

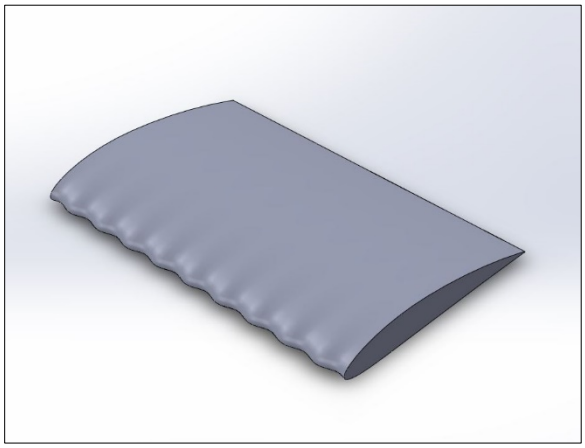

Figure 7**:** 4414_sin_1_0.4_150

Models were created by varying the amplitude and the wavelength to test the effect of these variables on the aerodynamic performance. Models 4414_sin_1_0.4_100, 4414_sin_0.6_0.4_100, 4414_sin_2_0.4_100, 4414_sin_3_0.4_100, 4414_sin_4_0.4_100 were

tested to analyze the effect of tubercle amplitude. These models are shown in Figures 8, 9, 10, 11, and 12.

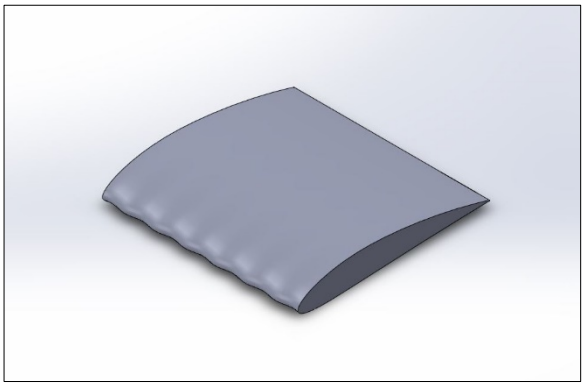

Figure 8: 4414_sin_1_0.4_100

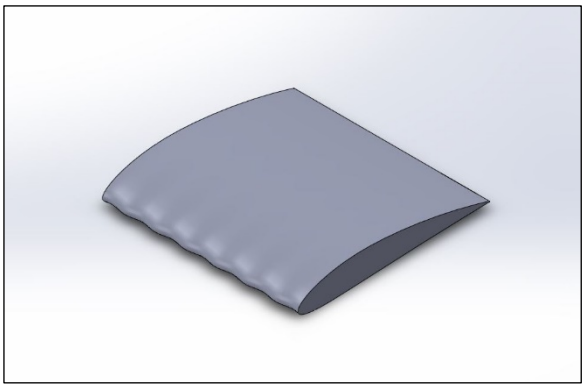

Figure 9: 4414_sin_0.6_0.4_100

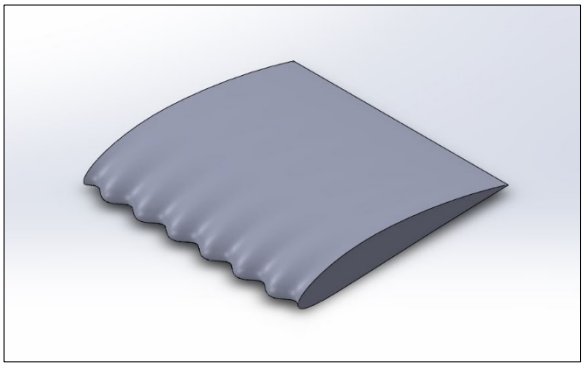

Figure 10: 4414_sin_2_0.4_100

Figure 11: 4414_sin_3_0.4_100

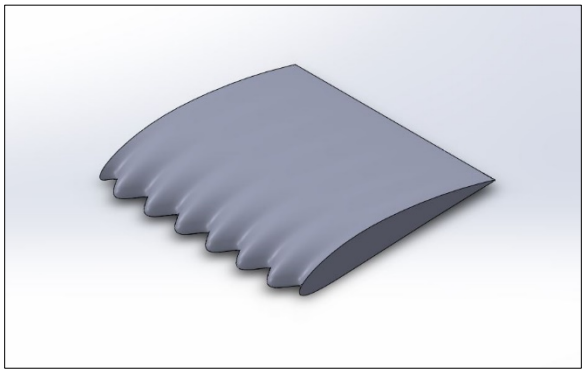

Figure 12: 4414_sin_4_0.4_100

Models 4414_sin_1_0.2_100, 4414_sin_1_0.6_100, 4414_sin_1_0.8_100, which are shown in Figures 13, 14, and 15, were created to test the effect of wavelength. They have wavelengths of 31.4%, 15.70% and 10.52% of the chord length, respectively.

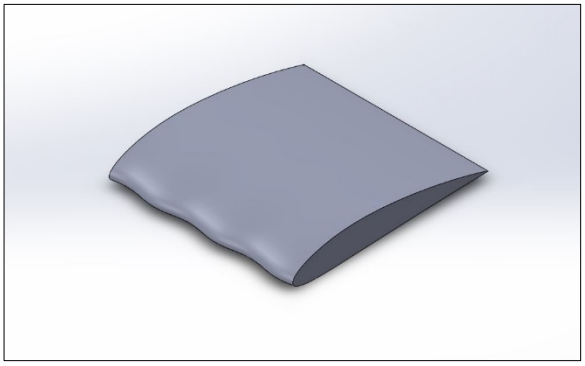

Figure 13: 4414_sin_1_0.2_100

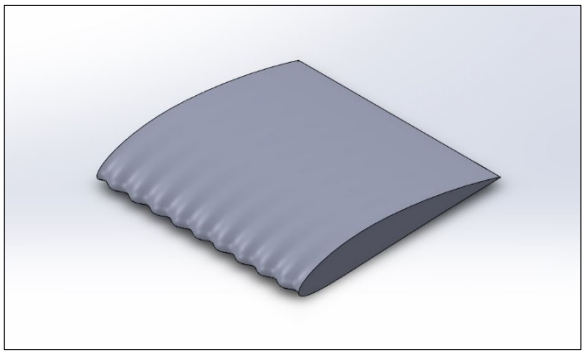

Figure 14: 4414_sin_1_0.6_100

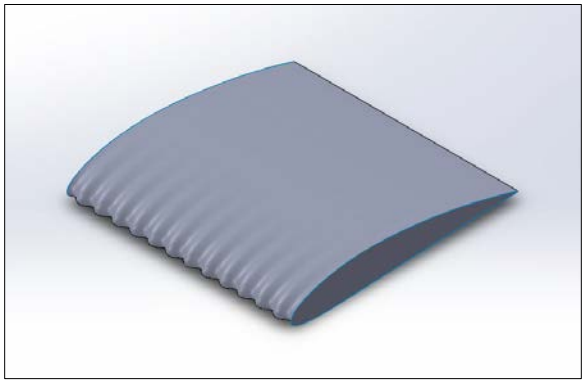

Figure 15: 4414_sin_1_0.8_100

Models were also created by removing waviness at the top and bottom surface of constant amplitude sinusoidal airfoils to check the effect of waviness on aerodynamic performance. Two straight lines were drawn connecting the airfoil boundary curves at a distance of 20% of the chord length from the origin, on the top and bottom side from the mid-plane. These lines were used as a guide curve for producing loft, in addition to the line at the trailing edge, to stop the

propagation of waviness to the rest of the body. Model 4414_1_0.4_100_V2 was created by this approach with flat top and bottom surfaces, as shown in Figure 16.

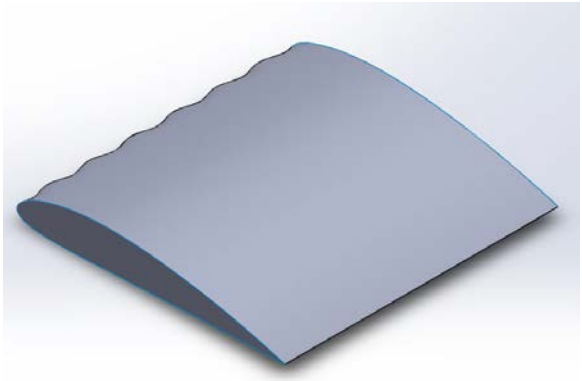

Figure 16**:** 4414_sin_1_0.4_100V2

Another type of model was created with only top surface waviness. 4414_sin_1_0.4_100V1 was created in this way and is shown in Figure 17.

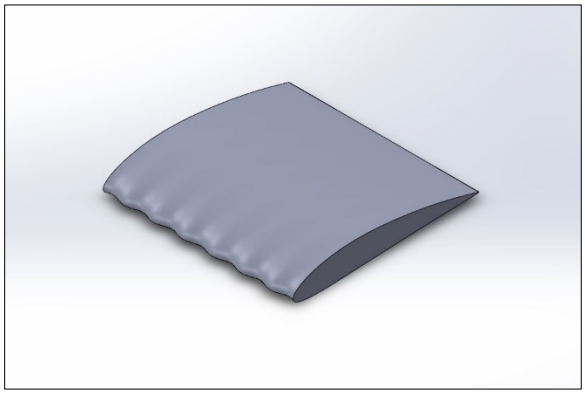

Figure 17: 4414_sin_1_0.4_100V1

For creating tubercle models with varying amplitude, the parametric variable "t" was multiplied before the sine function in the first parametric equation for X_t. Equation 24 is shown as an example of the equation that was used to create the varying amplitude airfoil 4414_sin_0.05t_0.4_55 with a span length of 55 mm. Here the lower limit t_1 and t_2 of the

parametric variable t were 0 and 55, respectively, giving a span length of 55 mm. As the parametric variable t was multiplied with the amplitude term, it generated a varying amplitude. At one root of the airfoil, the amplitude was zero, and it gradually increased as the span increased towards the other root. Hence, the maximum amplitude was 2.75 mm at the root where t_2 was 55. Model 4414_sin_0.05t_0.4_55 is shown in Figure 18. Other varying amplitude models are 4414_sin_0.05t_0.4_100, 4414_sin_0.025t_0.4_100, and 4414_sin_0.015t_0.4_100, which were created using the same method.

$$\mathbf{X_t = 0.05t * sin(0.4 * t)} \quad (24)$$

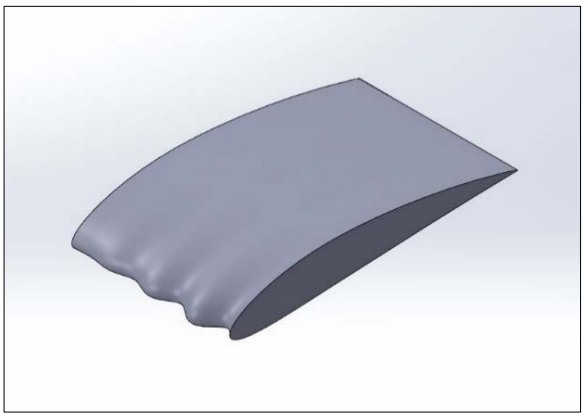

Figure 18**:** 4414_sin_0.05t_0.4_55

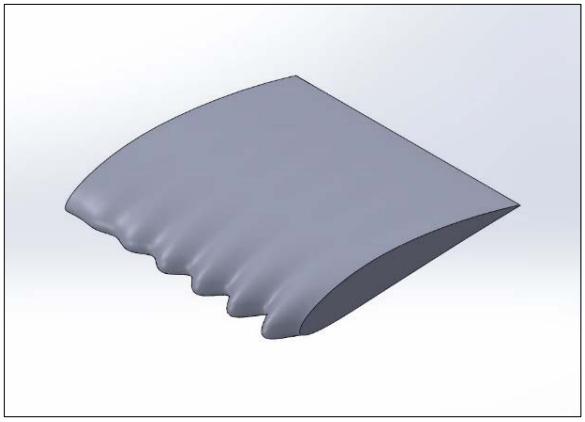

Figure 19: 4414_sin_0.05t_0.4_100

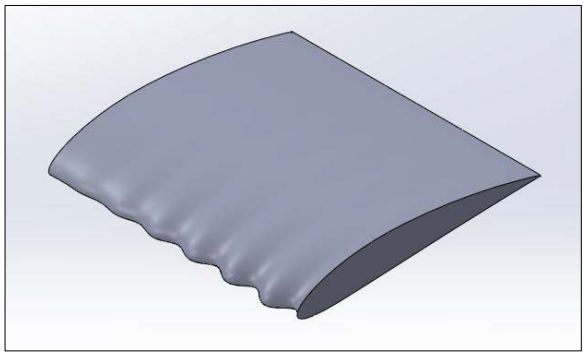

Figure 20: 4414_sin_0.025t_0.4_100

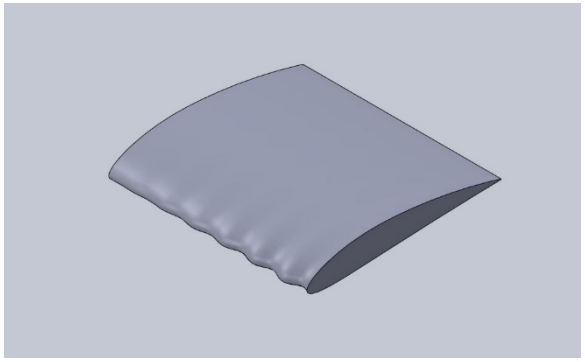

Figure 21: 4414_sin_0.015t_0.4_100

Model 4414_sin_0.6_0.2_100 was created with optimum magnitude of amplitude and wavelength found after analyzing several models. The model had an amplitude of 0.6% of the chord length and wavelength of 31.4% (0.2 factor) of the chord length. From Figure 22, it can be seen that the model had three crests and three troughs in the 100 mm span length.

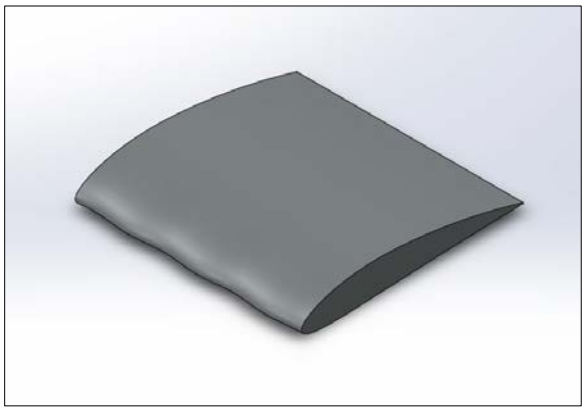

Figure 22: 4414_sin_0.6_0.2_100

5.2 Mesh Set-up

The Computational Fluid Dynamics (CFD) application software Star CCM+ was used for analyzing the airfoils. Initially, ANSYS was used for analysis purposes but failed to converge solutions of tubercle models. ANSYS required a higher number of cells and high disc space to capture the tubercle airfoil domain. On the other hand, STAR CCM+ provided similar mesh with faster time, a smaller number of cells, and lesser disc space with more controlling options. As the simulation results of ANSYS were not included in this report, its settings are not provided here. Settings that were used for generating mesh in Star CCM+ are shown in Table 3.

Table 3**:** Settings used for mesh in Star CCM+

Base size	50 % of chord length
Number of prism layer	15
Prism Layer Stretching	1.2
Prism Layer Thickness	4% of base
Surface curvature	400 ~ 500
Surface growth rate	1.2
Relative Minimum Size (Global)	4 ~ 6 % of base
Relative Target Size (Global)	30 ~ 50 % of base
Minimum cell size for airfoil	1.1 ~ 1.4 % of base
Relative Target Size for airfoil	6 % of base

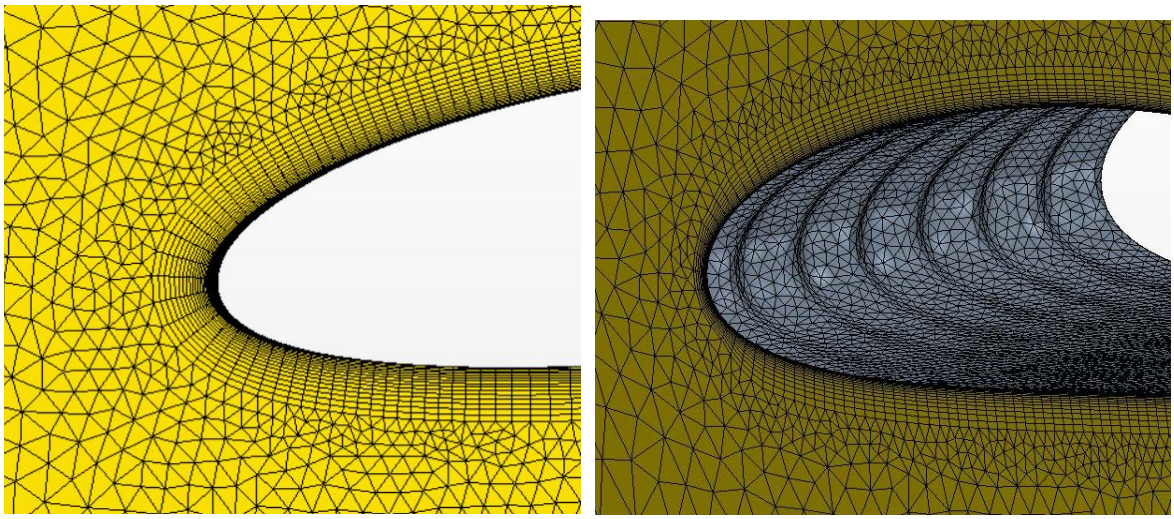

Figure 23: Prism layer at airfoil front (left); Volume mesh around airfoil (right)

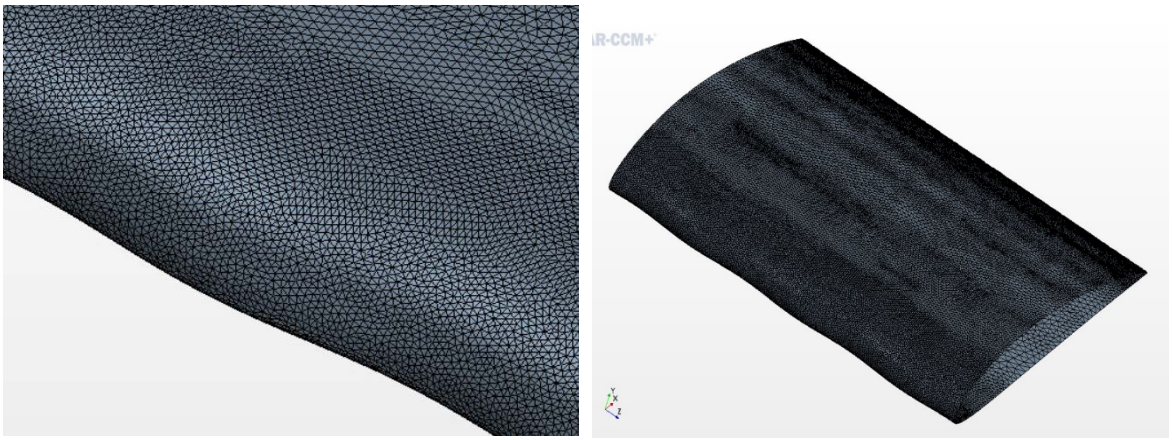

Figure 24: Mesh around the airfoil

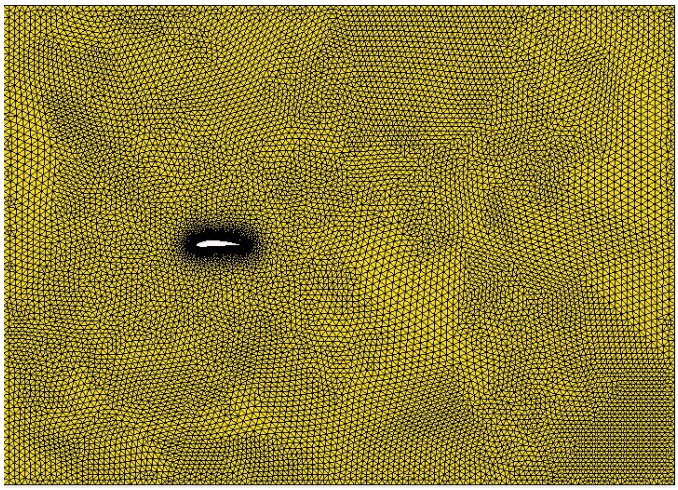

Figure 25: Domain with airfoil

5.2 Physics Set-up

All the tested models were three dimensional. As the speed used for this study was kept below the speed of sound or below Mach number 0.3, constant density was considered for the gas properties. Air density was assumed as 1.225 kg/m^3 and the dynamic viscosity of air was 1.85508 x 10^{-5} Pa-s. Reynolds-averaged Navier-Stokes (RANS) solvers with a realizable k-epsilon turbulence model was used for solving the simulations. Segregated flow was used for its fast and convenient converging capability. The following are the physics models that were enabled for all simulations.

1. Three dimensional
2. Steady flow
    a. Segregated flow
3. Gas
    a. Constant density
4. Turbulent
    a. K-epsilon Turbulence
    b. Two-layer All y + Wall treatment
    c. Exact Wall Distance
    d. Realizable K-epsilon Two-Layer
5. Reynolds-Average Navier-Stokes

5.3 Boundary Conditions

Only lift and drag coefficients were used for comparison to evaluate the performance of airfoils which are dependent on planform area. The domain was kept within the width of the airfoil neglecting the interaction of the side faces of the airfoils. The length and height of the domain were 15 times and 100 times the chord length, but the width was varied as models with different span lengths were created. The front domain plane was considered as the inlet, the rear domain plane as the outlet, the top and bottom faces as far field, and the side faces as symmetry, as shown in Figure 26.

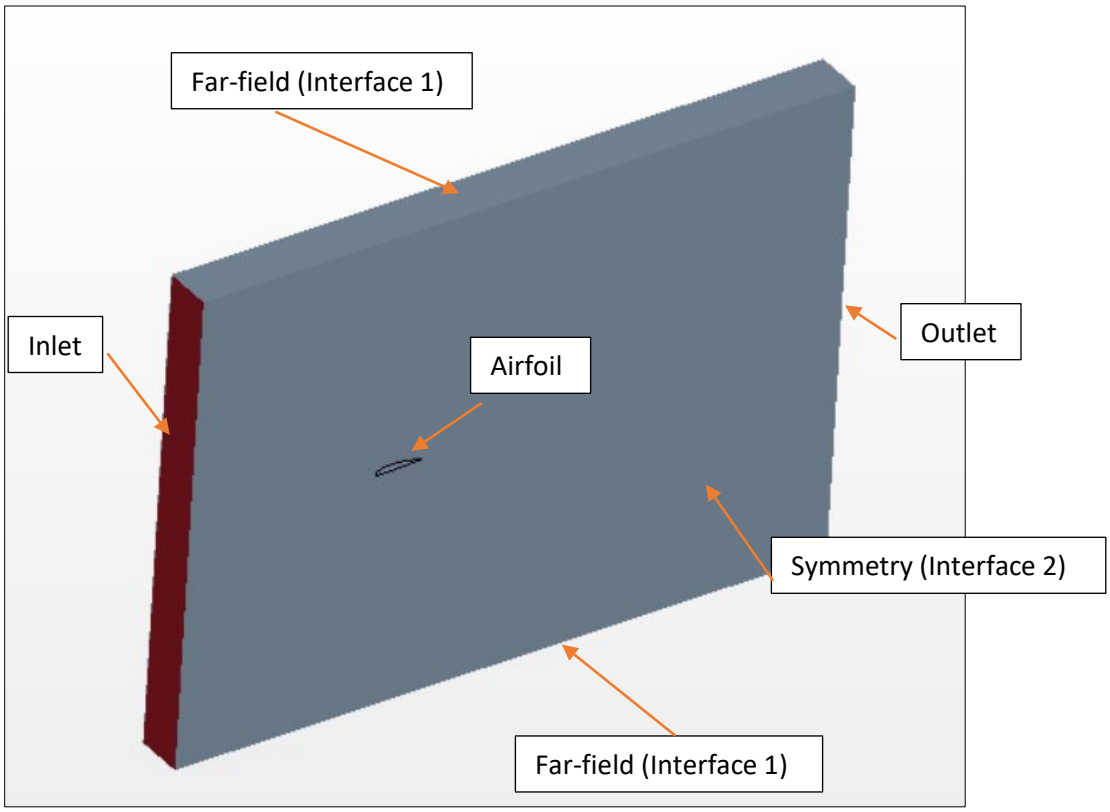

Figure 26: Boundary names

Boundaries with names of far-field and symmetry had wall boundary condition. Two interfaces were created, one taking far-field boundaries together and another taking symmetry boundaries together. Translational transformation was chosen for periodic interface topology. The boundary conditions used for testing the models are shown in Table 4.

Table 4: Boundary Conditions

Boundary Name	Boundary Conditions
Inlet	Velocity inlet
Outlet	Pressure Outlet
Far-field	Wall (Interface between far-field top & bottom boundaries)
Symmetry	Wall (Interface between symmetry right & left boundaries)
Interface Topology	Periodic
Periodic Transformation	Translational
Inlet Velocity	30 m/s for Reynolds number 200000 (chord length 0.1 m)
Inlet Velocity	15 m/s for Reynolds number 1000000 (chord length 1 m)
Inlet Velocity	75 m/s for Reynolds number 5000000 (chord length 1 m)
Inlet Velocity	145 m/s for Reynolds number 10000000 (chord length 1 m)

5.4 Validation

Validation tests were performed to select appropriate mesh density and for turbulent model selection. The methods of these validation processes that were followed during the study are discussed in this chapter.

5.4.1 Validation of Mesh Density – Grid Independence

It was necessary to determine how the mesh density affected the lift and drag coefficients of the airfoil. For this purpose, a grid independence test was performed at the beginning of this study with a Clark Y 3D airfoil since results are readily available in the literature. Five different mesh densities were created for simulation of the Clark Y-3D airfoil in the range of Reynolds number between 700000 and 2000000 at angles of attack of 0°, 8°, and 16°. The same number of iterations were carried out for all simulations. Data of lift and drag coefficients for different mesh densities are shown in Table 5.

Table 5: Grid Independence Test for 3D airfoil

Number of Cells	C_L	C_D	C_L	C_D	C_L	C_D
	AOA 0°		AOA 8°		AOA 16°	
702629	0.2992926	0.0088018	0.9931614	0.0408281	1.4999756	0.1105549
1024665	0.2932993	0.0086743	0.9822128	0.0394824	1.4783289	0.1063914
1237012	0.2936714	0.0085962	0.9855091	0.0394640	1.4636174	0.1041795
1550932	0.2867162	0.0082997	0.9690868	0.0382635	1.4513588	0.1022309
1994218	0.2871000	0.0082346	0.9711634	0.0381941	1.4588239	0.1018476

Table 6: Percentage change between number of cells

	C_L	C_D	C_L	C_D	C_L	C_D
	AOA 0°		AOA 8°		AOA 16°	
% change of 702629 & 1994218	4.07%	6.44%	2.21%	6.45%	2.74%	7.88%
% change of 1237012 & 1550932	2.37%	3.45%	1.67%	3.04%	0.84%	1.87%
% change of 1550932 & 1994218	-0.13%	0.78%	-0.21%	0.18%	-0.51%	0.37%

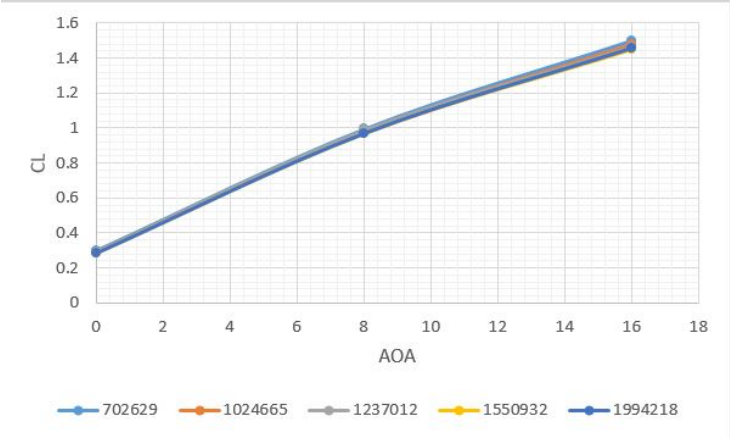

Figure 27: C_L vs. AOA (α) plot for different mesh density

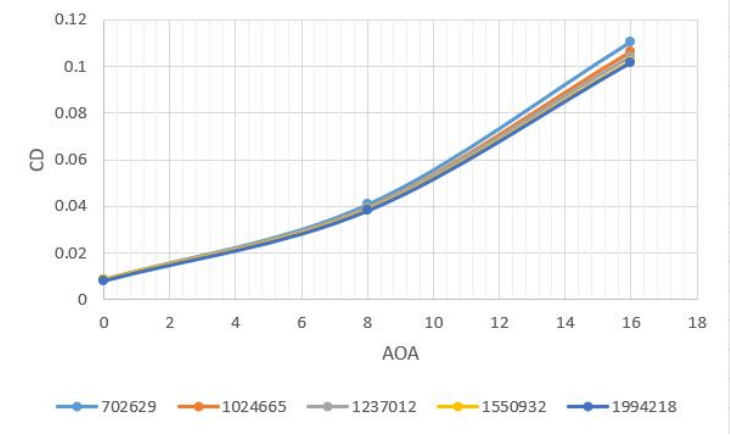

Figure 28: C_D vs. AOA (α) plot for different mesh density

The comparison plots of lift and drag coefficients vs angle of attack are shown in Figures 27 and 28. Both lift and drag values were found to get smaller with finer mesh. In Table 6, the percent difference of lift and drag for different mesh densities are provided. The maximum difference of lift coefficient was 4.07% which was obtained between the least dense and most dense mesh set up at 0° angle of attack. On the other hand the maximum percent difference was observed 7.88% between least dense mesh and most dense mesh at an angle of attack of 16°. The percent difference of both lift coefficient and drag coefficient became less with the simulation containing 1,550,932 cells. From Table 6, it can be seen that the maximum percent difference between this mesh density with its previous density was 2.37% for C_L and 3.45% for C_D at angle of attack 0°. The percent difference was much less between the mesh with 1,550,932 cells and the most dense mesh with 1,994,218 cells. A maximum change of 0.51% C_L at 16° and a change of 0.78% C_D at 0° was observed between these two mesh set-ups. Hence, mesh density for 1,550,932 cells was found to be optimum for testing the models.

5.4.2 Turbulent Model Validation

There are several computational models for simulating turbulent flow. It is difficult to match simulation data with experimental results completely, especially for cases where turbulence is very high. That is because of the computational limitation of the available software for turbulent flow. Most simulation models can give quite accurate results for airfoils at angles of attack before stall but fail to provide correct results after the stall angle. Even for smooth models, it is very difficult to get complete analogous data by any turbulent model at high angles of attack. For tubercle models that have high geometric angles of attack at the leading edge, it is even more difficult. Few studies were conducted by researchers to analyze different

turbulent models to find the best model for airfoils. For example, Eleni Douvi et al. (2012) carried out numerical analysis on NACA 0012 airfoils using three different turbulent models respectively Spalart Allmaras, Realizable k-epsilon and k-omega SST. They found most close values to the experimental results with the k-omega SST model. K-epsilon model also provided very close results to the experimental results but not close enough after the stall angle. None of the three models provided exact results like the experiment.

For this study, a lot of time was involved in finding the correct turbulent model. Three very widely used turbulent flow models Spalart Allmaras, K-epsilon, and K-omega were used to simulate the Clark Y 3D airfoil and they were compared with available experimental data. The enabled models for the k-epsilon family was the Realizable K-epsilon, two layer All y+ wall treatment, and exact wall distance. The enabled models related to k-omega turbulent solver were k-omega SST (Menter), two layer All y+ wall treatment, and exact wall distance. Spalart-Allmaras provided close value to the experimental results below angles of attack of 8°, but with higher values such as 12° it provided much higher values than the experimental. It provided very low after stall lift coefficient compared to the experimental data. Similar results were also observed for the SST k-omega model. Although this model provided the best results up to an angle of attack 12°, it deviated significantly from the experimental C_L curve starting after 12°. The model also stalled at 12° which was earlier than the experimental stall angle. On the other hand, the k-epsilon model gave slightly lower values of C_L at pre-stall angles but maintained the pattern with experimental data both at pre-stall and post stall angles. Although none of the models were able to match the experimental data accurately, due to the consistency provided by the Realizable k-epsilon model it was selected for using as the turbulent model for the rest

of the experiments. Figure 29 shows the comparison plot of lift coefficient for different turbulent models with experimental data.

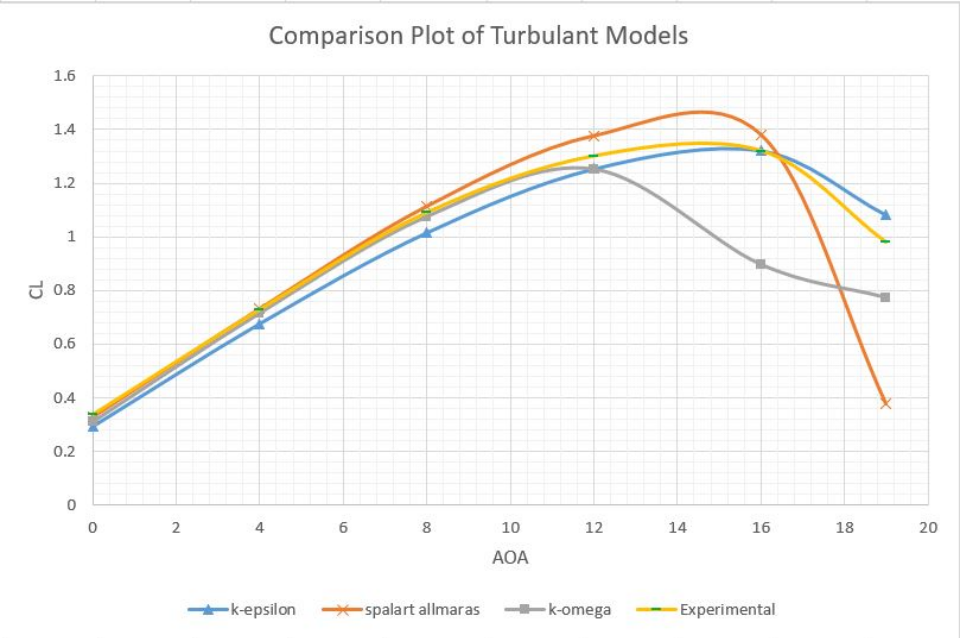

Figure 29: Graph for comparing turbulent models with experimental data

5.5 Post Processing

For straight leading-edge airfoils, flow behavior was very much constant all over the airfoil in any plane taken parallel to YZ. However, for tubercle airfoils, flow had notable variation at different locations along the span. The flow at the crest was different than the flow at the trough area due to their different geometric angles. Difference in the magnitude of velocity, pressure and vorticity continued to the trailing edge, which is why flow was different across the same YZ plane unlike straight airfoils. These differences were much larger for higher angles of attack. Hence, taking only a single plane of velocity or pressure contour was never sufficient for a tubercle model's flow analysis. To understand the flow physics at different locations on the airfoil body, several post processing tools were used, such as velocity contour, pressure contour, vector plot, streamlines, etc. Due to the variation of flow at different regions, several planes were created to plot contour plots of different variables. Sectional planes were created at different locations normal to X-axis and Z-axis. It was necessary to define these planes to avoid confusion during analysis of the contour plots.

Two sectional planes named Plane XY_Z50 and Plane_YZ_X80 are shown in Figures 30 and 31, respectively. The names were given from the coordinate information of the created planes. For example, the plane XY-Z50 was parallel to the XY plane and it was at a distance of 50 mm from the origin in the Z direction; similarly, plane YZ-X80 was in the YZ plane and 80 mm away from the origin in the X direction. The same naming convention is true for all planes created for post processing contour plots. For tubercle airfoils, XY planes were created at both the crest and valley of the tubercles. Planes taken parallel to the XY planes for tubercle models were different

for different models because the position of the crest and trough were different for each model. Velocity contours and vectors were plotted in sectional planes.

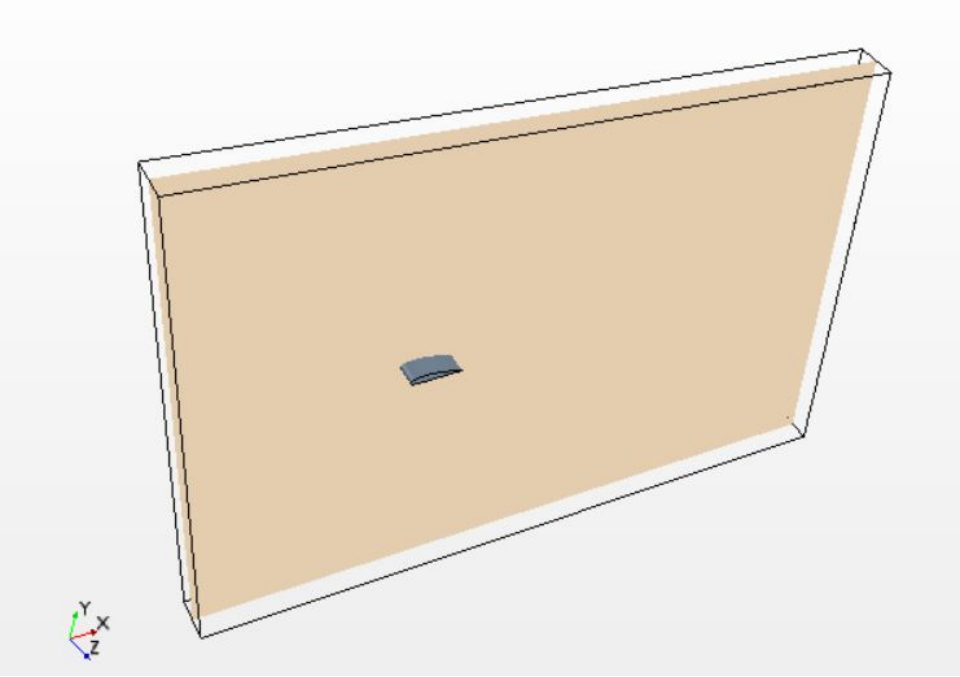

Figure 30: Plane XY_Z50

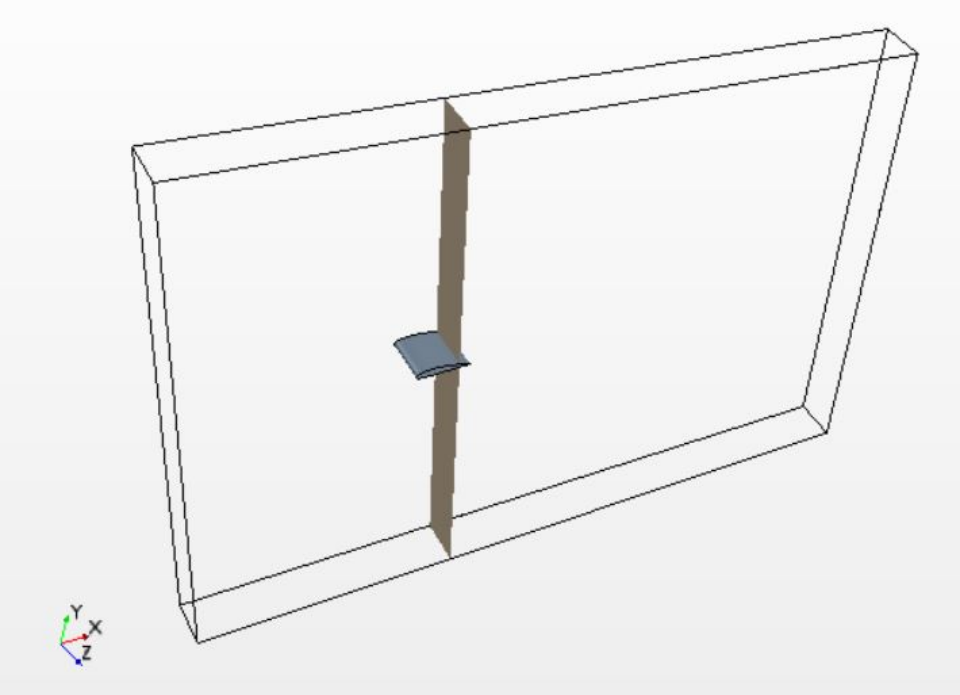

Figure 31: Plane YZ_X80

Streamlines were also used for some models to analyze the flow behavior with a different approach. For different angles of attack, streamlines were generated in terms of velocity at corresponding coordinate systems . Tubes were used as flow streams so that the difference in velocity magnitude was easliy distinguishable.

6. Results and Discussion

Simulations were conducted for the NACA 4414 airfoil and all tubercle airfoils for angles of attack of 0°, 4°, 8°, 12°, 16°, 18°, 20°. Results obtained from tubercle airfoils were compared with the base NACA 4414 airfoil data to evaluate performance changes. The lift coefficient (C_L), drag coefficient (C_D) and lift to drag ratio (C_L/C_D) were calculated for comparison purposes. For analysis purpose, different scalar and vector contour plots were taken in terms of velocity, pressure, streamlines, etc. All the models were simulated for 3000 iterations which was observed as a good number for the convergence of the solutions.

6.1 Base Airfoil Data

Simulation of the NACA 4414 airfoil was performed at the beginning of the study. Plots of lift coefficient, C_L, and drag coefficient, C_D, against angles of attack (AOA), α, are shown in Figures 32 and 33. The lift coefficient increased linearly up to an angle of attack of 12°. After 12°, the C_L curve started to deviate nonlinearly with gradual decrease of the slope until the stall angle of 18° where lift coefficient reached the maximum value of 1.46187. After stalling at 18° the lift coefficient dropped significantly with a 9.57% decrease at 20°. On the other hand, the drag coefficient (C_D) increased exponentially for angles of attack between 0° and 12° but increased linearly afterwards up to 20°. The maximum drag coefficient value of 0.14326 was obtained at an angle of attack of 20°.

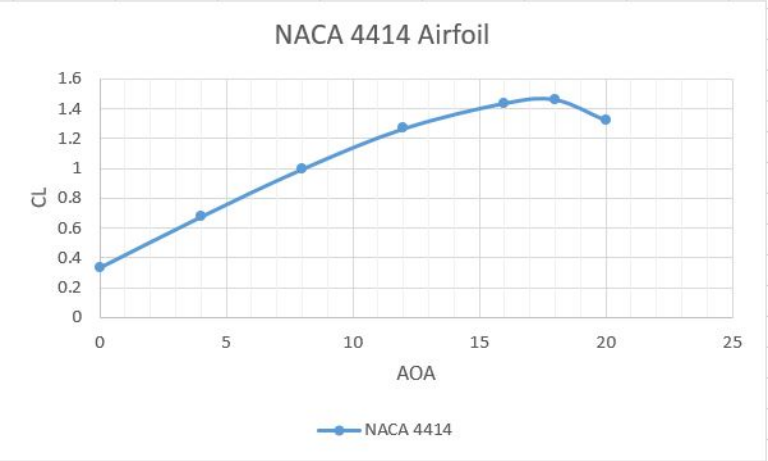

Figure 32: Angle of attack (α) vs. Lift Coefficient (C_L) plot for NACA 4414 base airfoil

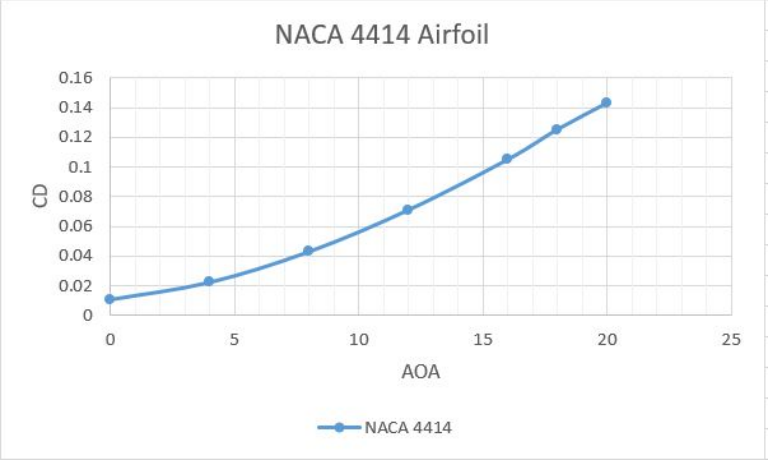

Figure 33: Angle of attack (α) vs. Drag Coefficient (C_D) for NACA 4414 base airfoil

Velocity contour plots of the NACA 4414 airfoil at the plane XY-Z50 for angles of attack from 0° to 20° are shown in Figures 34 to 37. Flow separation started to become dominant and rapid with the increase of angle of attack (blue zone at airfoil aft). At high angles of attack, the thickness of the wake zone increased and the separation point became closer to the leading edge. At the 18° and 20° angles of attack, the separation started almost at the middle of the airfoil. From these contour plots at the plane XY-Z50 it was observed that the maximum velocity of the airfoil increased with the increase of angle of attack.

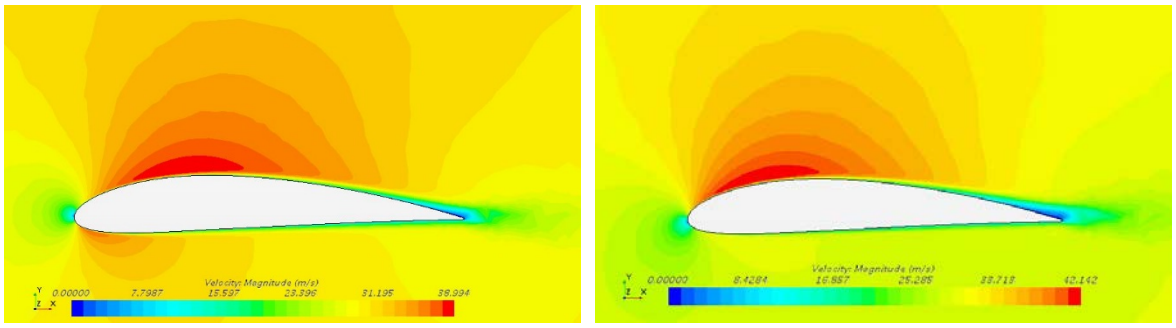

Figure 34: Velocity contour of NACA 4414 at XY-Z50; α=0° (left), α=4° (right)

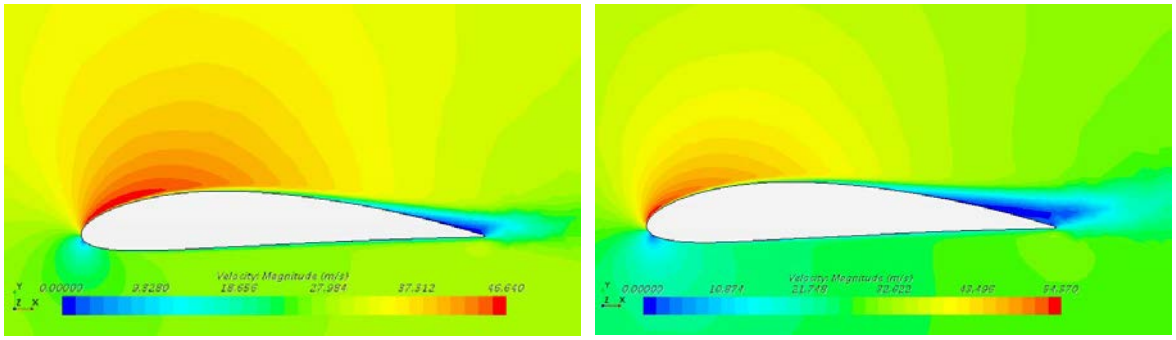

Figure 35: Velocity contour of NACA 4414 at XY-Z50; α=8° (left), α=12° (right)

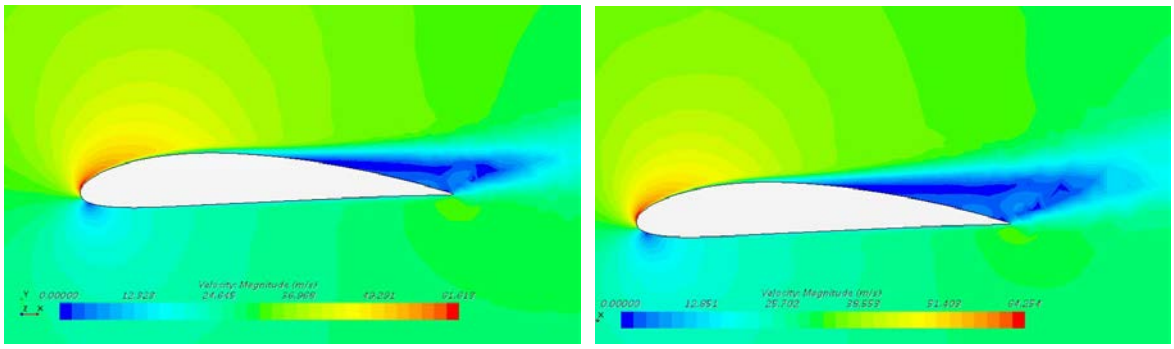

Figure 36: Velocity contour of NACA 4414 at XY-Z50; α=16° (left), α=18° (right)

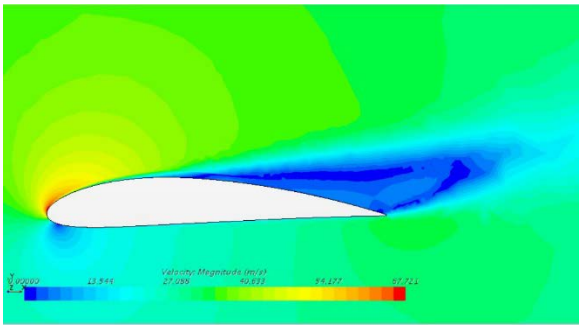

Figure 37: Velocity contour of NACA 4414 at XY-Z50; α=20°

Velocity contours were also taken on plane YZ-X80 which are shown in Figures 38 to 41. An important observation from these contour plots was that the separation of flow was the same at all locations across the airfoil, i.e. spanwise. With increasing angle of attack, the wake zone increased simultaneously across the span length. That is why wake zones of uniform thicknesses were observed in this plane. The maximum velocity at this plane also increased with increasing angle of attack. On this plane, the lowest maximum velocity of 32.78 m/s was recorded at the angle of attack 0° and the highest value of maximum velocity of 34.67 m/s at the angle of attack 20°.

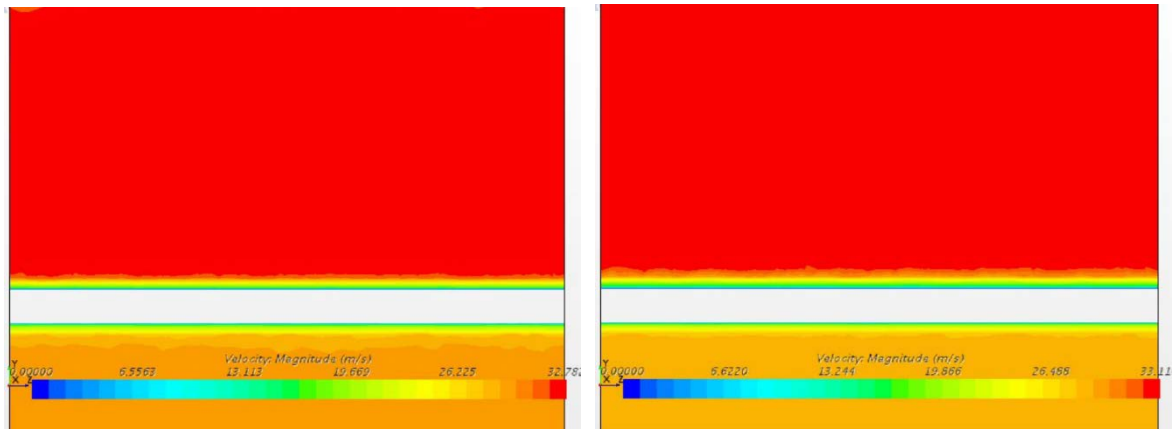

Figure 38: Velocity contour of NACA 4414 at plane YZ-X80; α=0° (left), α=4° (right)

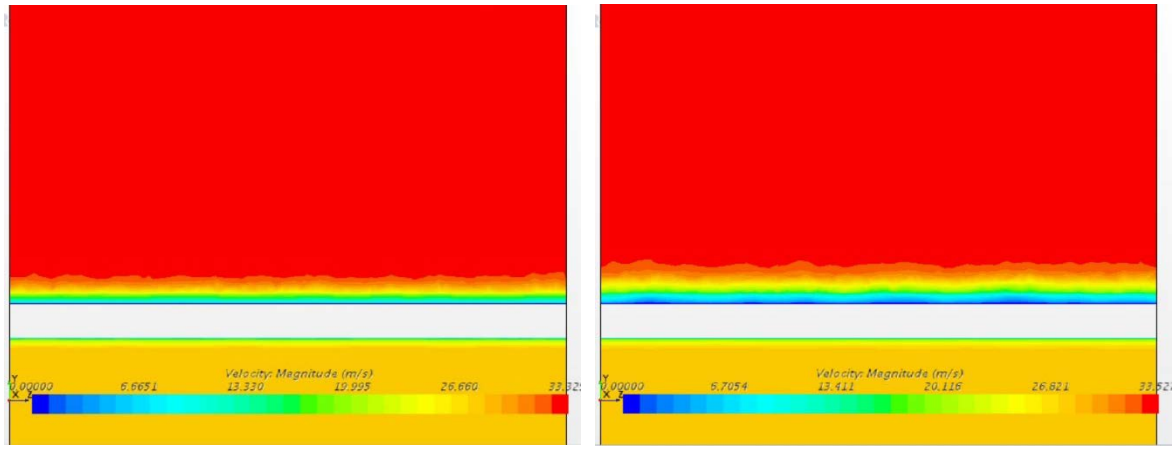

Figure 39: Velocity contour of NACA 4414 at plane YZ-X80; α=8° (left), α=12° (right)

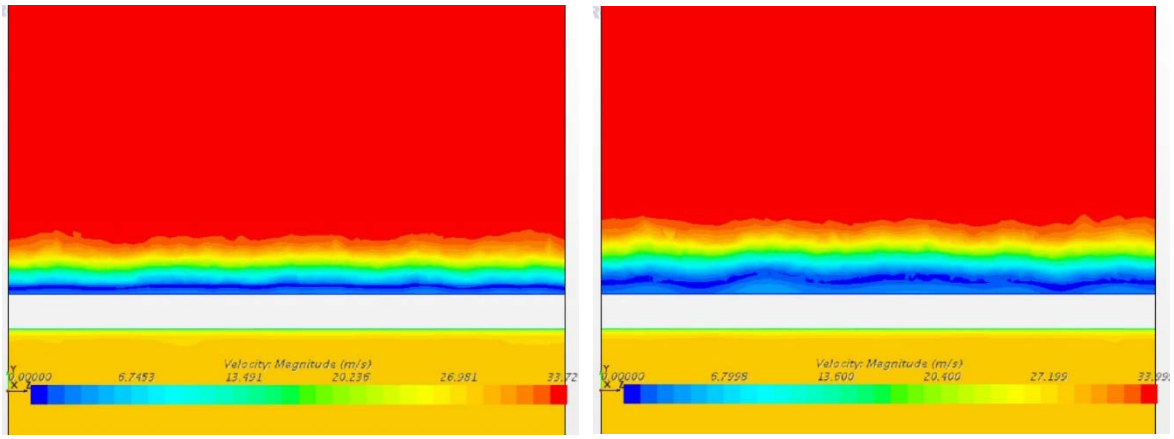

Figure 40: Velocity contour of NACA 4414 at plane YZ-X80; α=16° (left), α=18° (right)

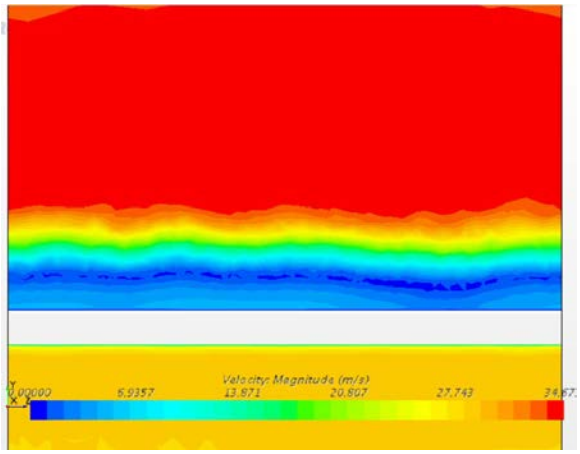

Figure 41: Velocity contour of NACA 4414 at plane YZ-X80; α=20°

6.2 Tubercle Models with Alternative Approach

Alternative approaches were applied to create tubercle airfoils instead of sinusoidal leading edge. In this section results of two such models with two different approaches are discussed. The first alternative tubercle model is 4414_Tubercle1_25 with elliptical tubercles at the front top side of the airfoil. Lift coefficient and drag coefficient plots versus angles of attack for alternative tubercle model 4414_Tubercle1_25 are shown in Figures 42 and 43. The lift coefficient curve for model 4414_Tubercle1_25 showed agreement with the base airfoil NACA 4414 up to an 8° angle of attack. However, after 8° the lift coefficient started to become lower

than the base airfoil and it continued the same way until stall at 18°. After the stall, the lift coefficient started to fall but at a slower rate than the base airfoil. Drag coefficient was always slightly higher than the base airfoil from the very beginning. Deviation of C_D from base airfoil was prominent after the angle of attack 18°. In the comparison plot of lift to drag ratio C_L/C_D in figure [44] it was observed that the ratio was always lower for the tubercle airfoil from the base airfoil. Nonetheless, results were promising in the post-stall region.

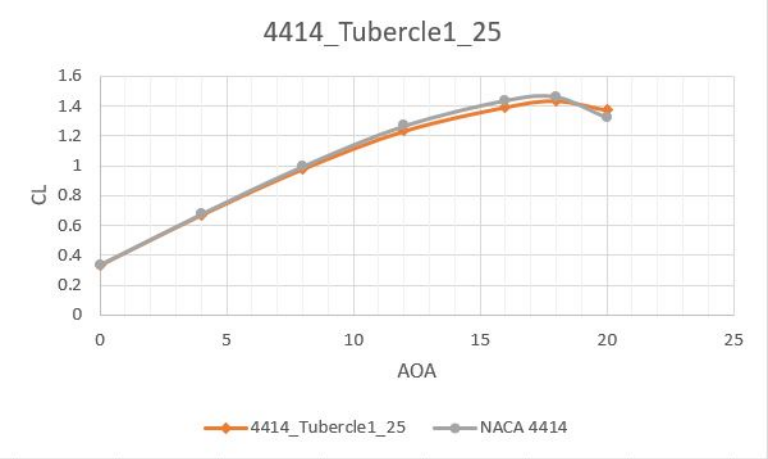

Figure 42: C_L vs. α for 4414_Tubercle1_25 and NACA 4414

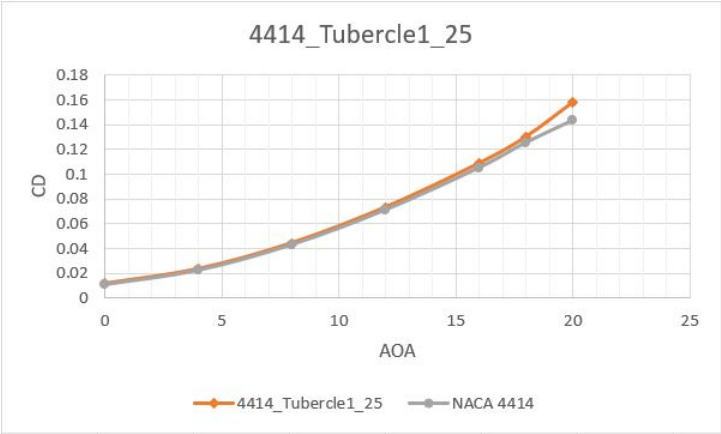

Figure 43: C_D vs. α for 4414_Tubercle1_25 and NACA 4414

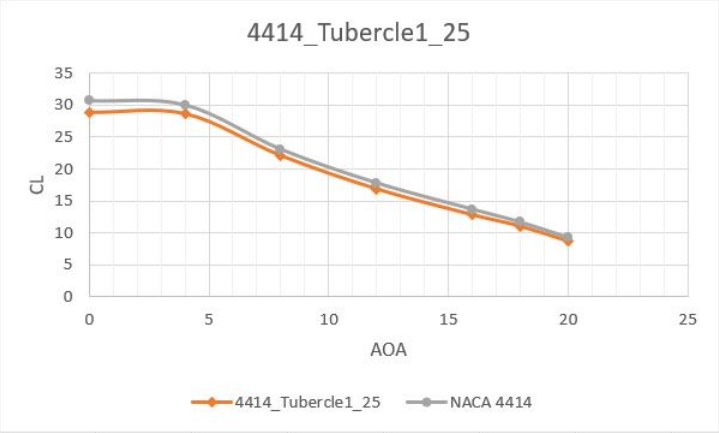

Figure 44: C_L/C_D vs. α for 4414_Tubercle1_25 and NACA 4414

The velocity contours at the plane YZ-X80 for model 4414_Tubercle1_25 are shown in Figures 45 to 48. Due to the presence of the tubercles at the front side of the airfoil the wake zones were not uniform like the base NACA 4414 at the same plane. The wake zone was narrowed behind each tubercle bump which gave a wavy appearance to the wake zone. These narrow wake zone indicates the elliptical tubercles are helping the flow to stay attached to the airfoil surface. However, although the tubercles assisted to control flow separation, low lift values and high drag values were recorded in the pre-stall region. This can be caused due to the position of the tubercles and their geometric shape. Despite this, in the post stall zone, the tubercles influenced the flow separation to avoid drastic fall of the C_L.

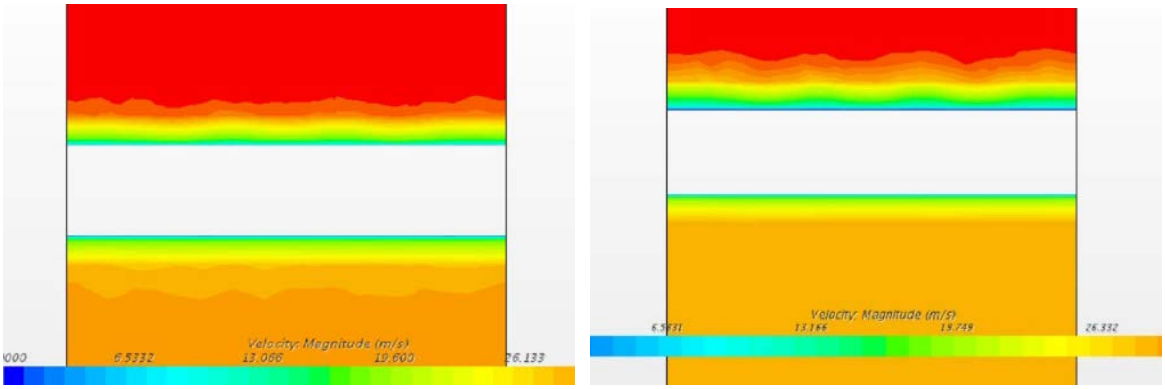

Figure 45: 4414_Tubercle1_25 velocity contour at Plane YZ-X80, α=0° (left); α =4° (right)

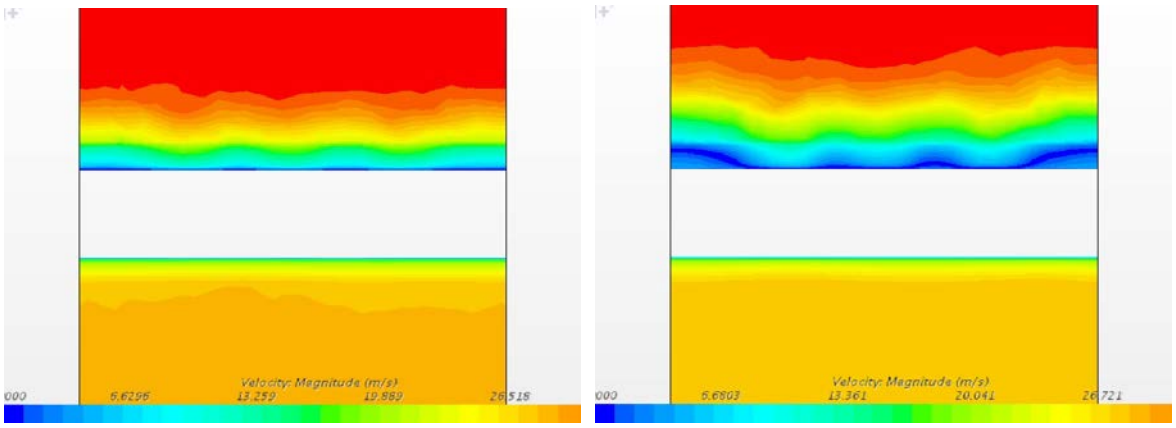

Figure 46: 4414_Tubercle1_25 velocity contour at Plane YZ-X80, α =8° (left); α =12° (right)

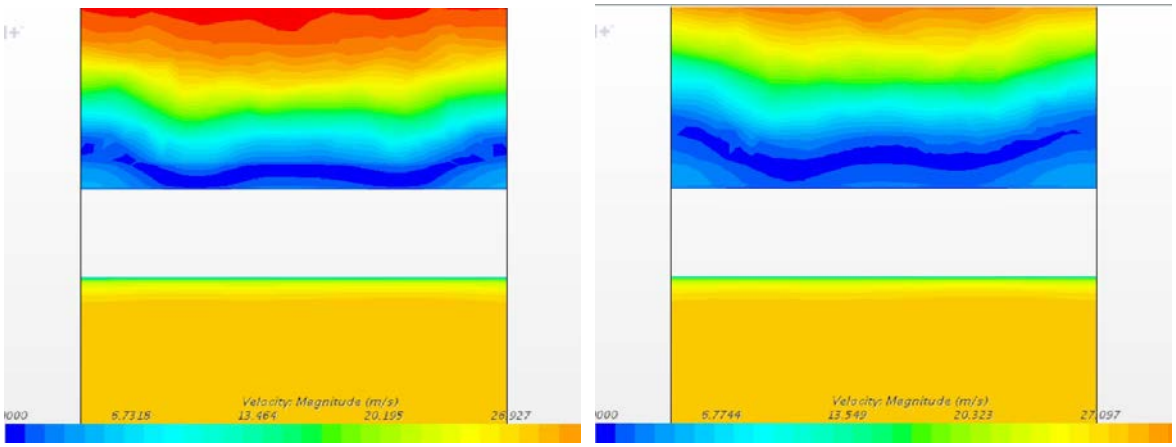

Figure 47: 4414_Tubercle1_25 velocity contour at Plane YZ-X80, α=16° (left); α=18° (right)

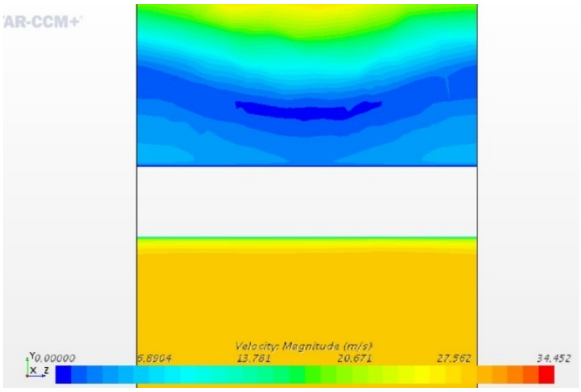

Figure 48: 4414_Tubercle1_25 velocity contour at Plane YZ-X80, α=20°

Alternative tubercle model 4414_Tubercle4_50 was created with bumps at the leading edge, but unlike sinusoidal tubercle airfoils the trough of this airfoil was straight. From the C_L curve in

Figure 49 it is observed that the lift curve for this tubercle airfoil and the NACA 4414 were similar up to 16°. In the pre-stall region, the highest increase in lift from the base airfoil was found 3.93% at the angle of attack 0° with a gradual decrease of the difference at higher angles of attack. Maximum C_L reduced 1.42% from the base airfoil with a 2° reduction in stall angle. From the drag coefficient plot in Figure 50, it is observed that C_D was higher for all angles of attack than the base airfoil. C_D started to deviate at a higher rate after the 12° angle of attack. After 10° this model gave significantly lower values of lift to drag ratio due to the sudden rise of drag after this angle which can be seen in the C_L/C_D comparison plot in Figure 51. This model demonstrated improved lift performance in the pre-stall zone compared to the previous airfoil model.

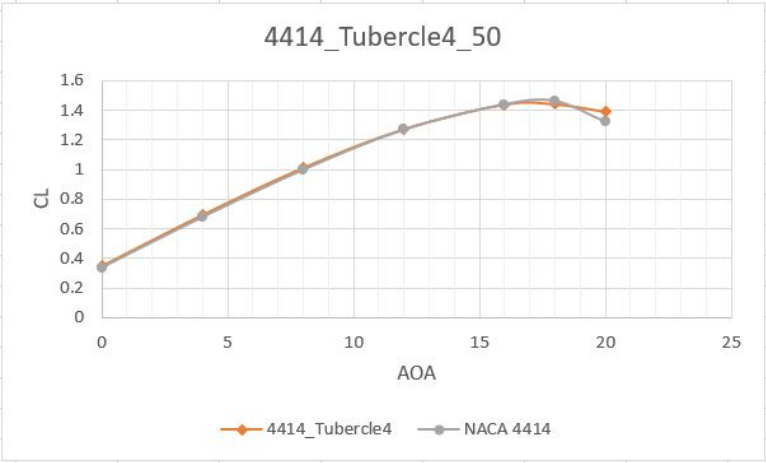

Figure 49: C_L vs. α for 4414_Tubercle4_50 and NACA 4414

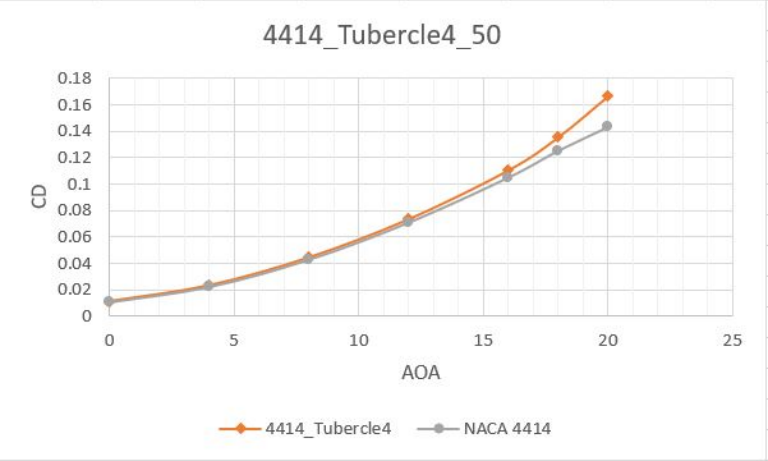

Figure 50: C_D vs. α for 4414_Tubercle4_50 and NACA 4414

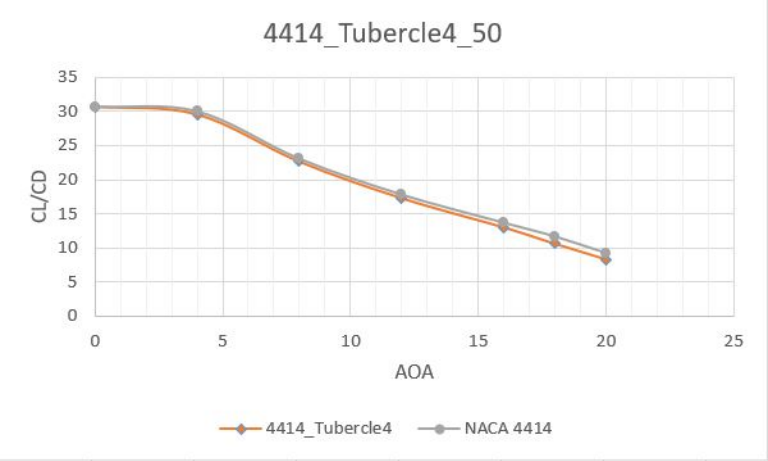

Figure 51: C_L/C_D vs. α for 4414_Tubercle4_50 and NACA 4414

Velocity contours at plane YZ-80 are shown in Figures 52 to 55. The maximum velocity at most of the angles of attack were slightly higher than the base NACA 4414 airfoil at this same plane. The effect of tubercles started to become visible at an angle of attack of 12° where, instead of a straight wake zone, a non-uniform wavy wake zone was formed. This pattern was also seen in the sinusoidal tubercle airfoils which suggests that these tubercles help to control flow separation in a similar way as the conventional tubercles. However, at high angles of attack, large wake zones were observed at the two roots of the airfoil. This could potentially be a result of the symmetry wall boundary condition.

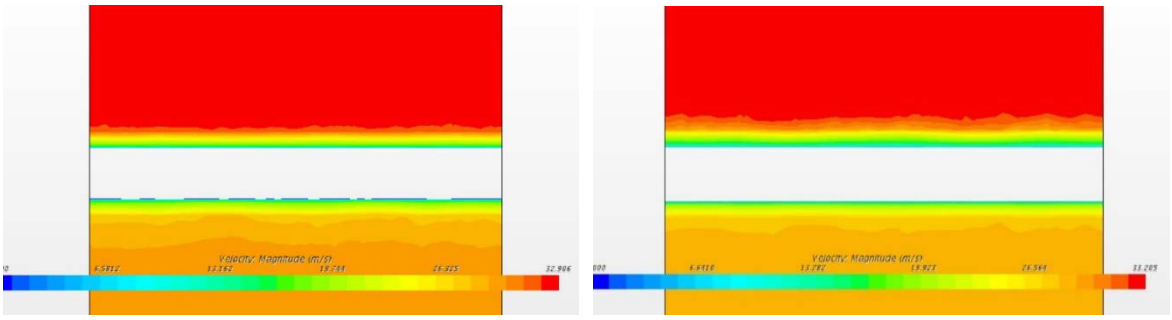

Figure 52: 4414_Tubercle4_50 velocity contour at plane YZ-X80; α=0°(left); 4° (right)

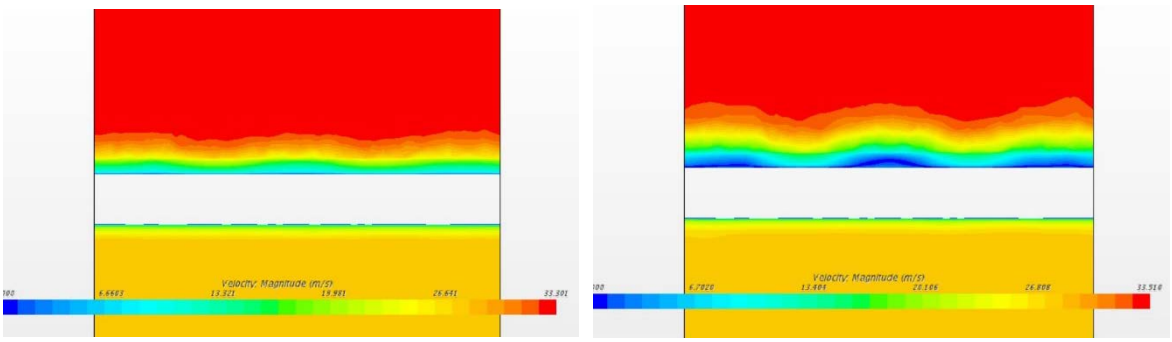

Figure 53: 4414_Tubercle4_50 velocity contour at plane YZ-X80; α=8°(left); α=12°(right)

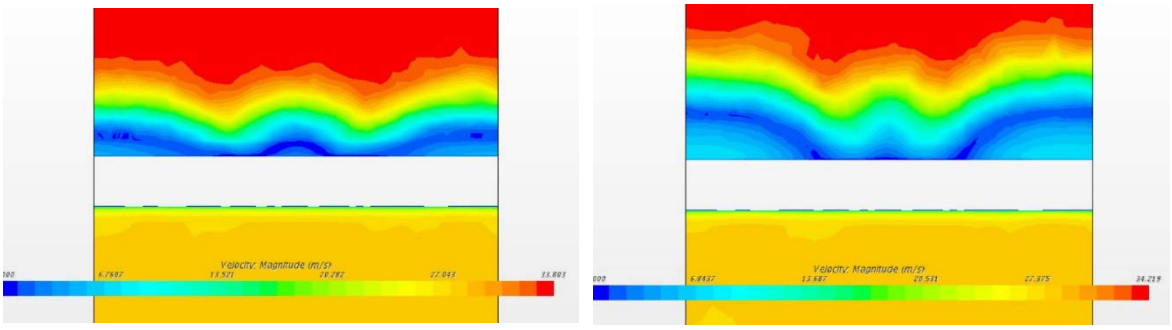

Figure 54: 4414_Tubercle4_50 velocity contour at plane YZ-X80; α=16° (left); α=18° (right)

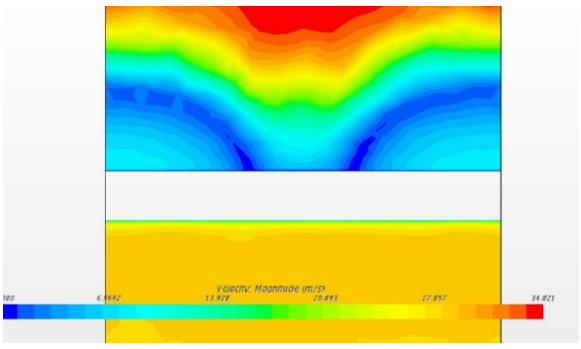

Figure 55: 4414_Tubercle4_50 velocity contour at plane YZ-X80; α=20°

6.3 Sinusoidal Tubercle Airfoil with Varying Amplitude

Model 4414_sin_0.05t_0.4_55 was the first tested sinusoidal model with varying amplitude. At one root, the amplitude of the tubercle was highest, and the amplitude gradually decreased while moving to the other end. The lift coefficients were slightly higher for all angles of attack up to 16°, and then dropped drastically at the post stall region, as can be seen in Figure 56. At 18° the reduction of C_L from the base NACA 4414 airfoil was 26.92%. The drag coefficient was very much like the base airfoil up to 12°, and after that, it started to become very high. After 16° the C_D curve jumped, with a 33.35% increase from the base airfoil. The lift to drag coefficient ratio was found to be 31.69 for the angle of attack 0°, which was higher than the base airfoil ratio of 30.72. However, after angle of attack of 4° the C_L/C_D ratio was found to be lower again than the base NACA 4414 airfoil. The plot of lift to drag ratio versus angle of attack is shown in Figure 58.

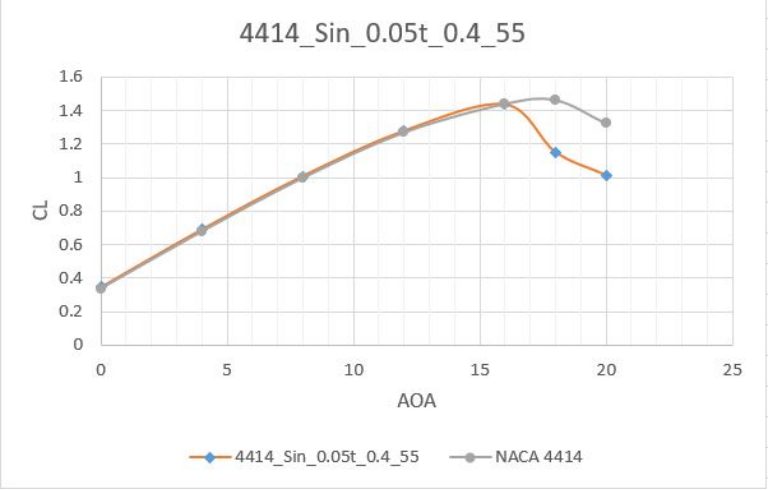

Figure 56: C_L vs. α for 4414_sin_0.05t_0.4_55 and NACA 4414

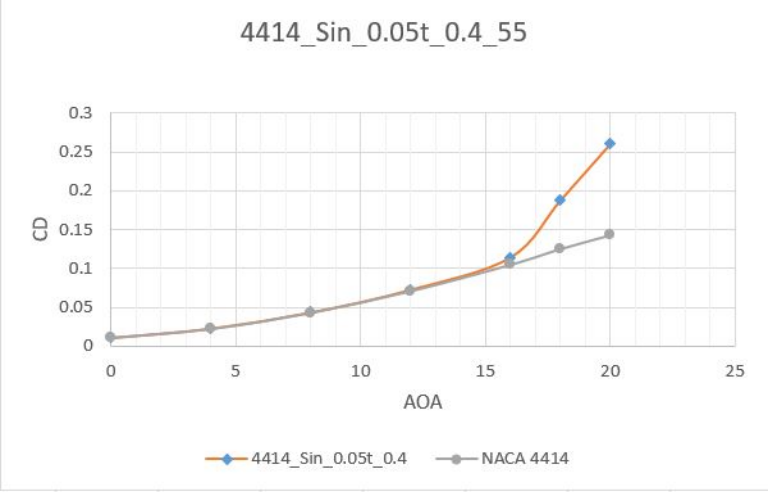

Figure 57: C_D vs. α for 4414_sin_0.05t_0.4_55 and NACA 4414

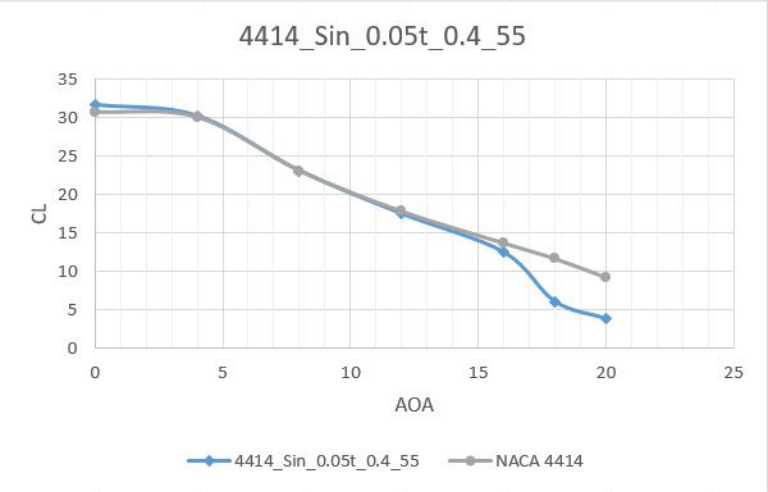

Figure 58: C_L/C_D vs. α for 4414_sin_0.05t_0.4_55 and NACA 4414

Velocity contours at YZ-X80 plane for the model 4414_sin_0.05t_55 are shown in Figures 59 to 61. The left side of the airfoil, where the tubercles are low in amplitude, had a much more attached flow than the right side. At the right side of the airfoil, the boundary layer separation patterns started to become like a uniformly varying tubercle airfoil from the angle of attack 12°. At 16° the wake zone became very big, which explains the sudden drop of lift coefficient. At the angle of attack 18°, the velocity contour shows that a significant low-pressure area was formed

at the two roots of the airfoil, which could be caused due to the interaction of the vortices with the symmetry wall.

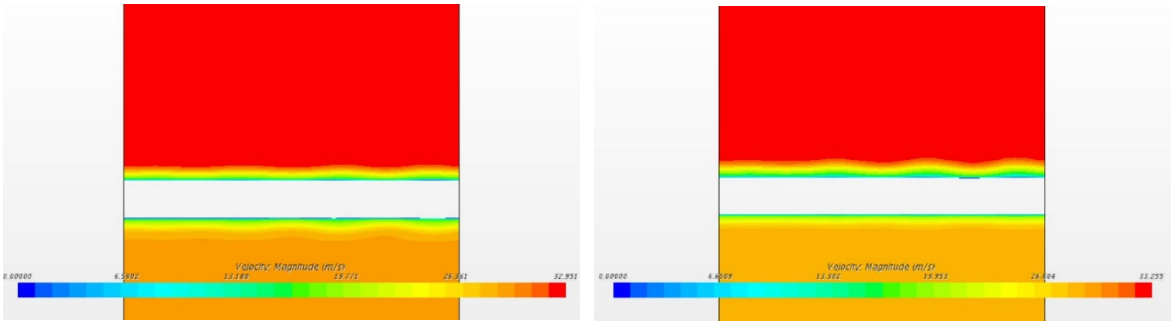

Figure 59: 4414_sin_0.05t_0.4_55 velocity contour at YZ-X80; at α 0° (left), at α 4° (right)

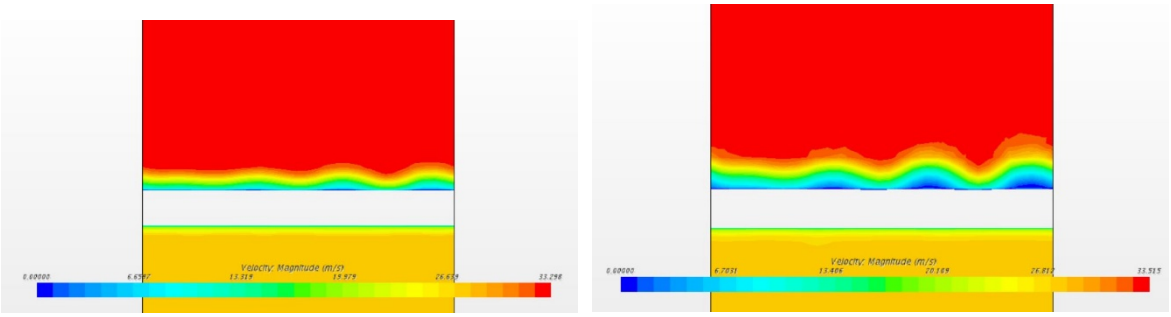

Figure 60: 4414_sin_0.05t_0.4_55 velocity contour at YZ-X80; at α 8° (left), at α 12° (right)

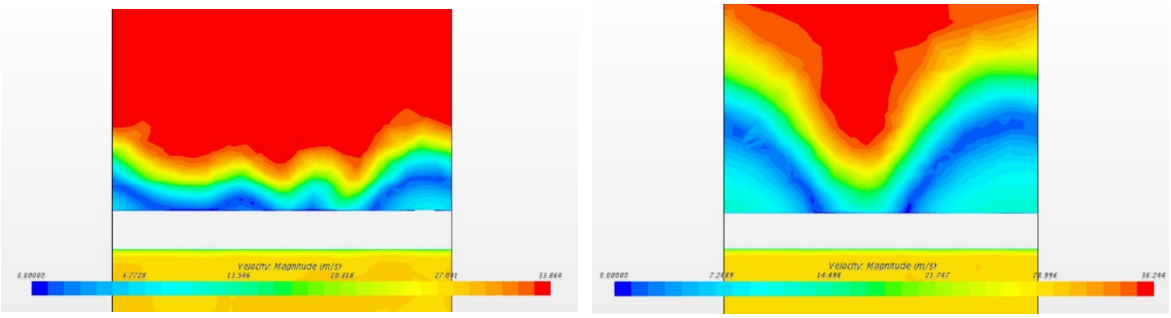

Figure 61: 4414_sin_0.05t_0.4_55 velocity contour at YZ-X80; at α 16° (left), at α 18° (right)

A second sinusoidal tubercle airfoil with varying amplitude model, 4414_sin_0.05t_100, with 100 mm span length was tested. This model stalled too early at the angle of attack 12° but produced higher lift coefficients at low to moderate angles of attack. However, the drag was high as well which resulted in the lift to drag coefficient ratio curve to become significantly

lower than the base NACA 4414 airfoil. The lift coefficient, the drag coefficient, and the lift to drag ratio versus angle of attack are shown in Figures 62, 63, and 64, respectively.

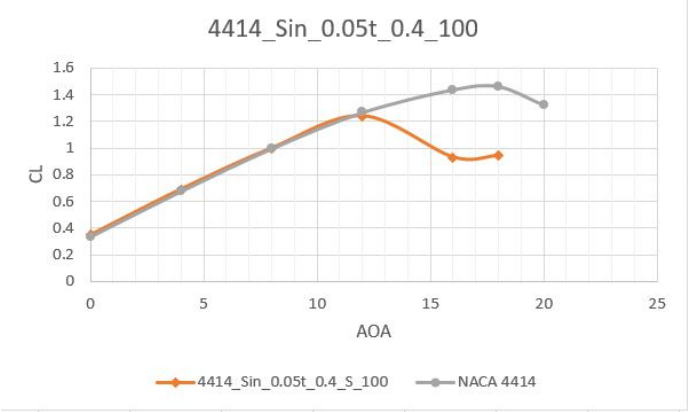

Figure 62: C_L vs. α for 4414_sin_0.05t_0.4_100 and NACA 4414

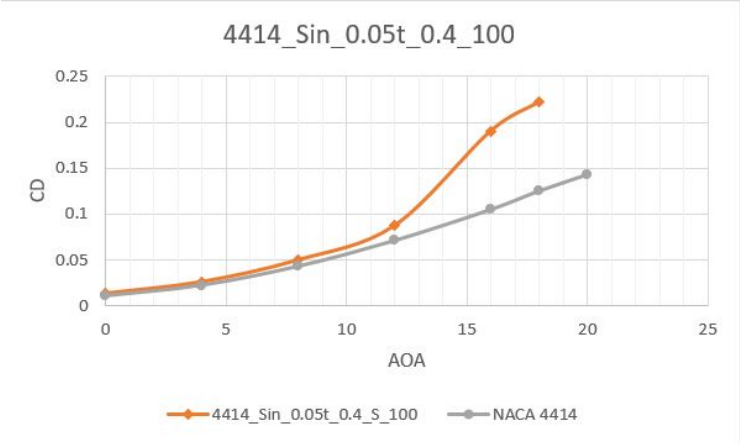

Figure 63: C_D vs. α for 4414_sin_0.05t_0.4_100 and NACA 4414

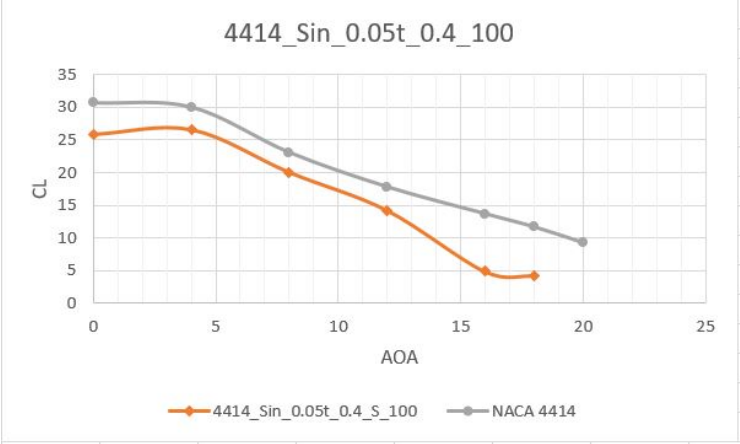

Figure 64: C_L/C_D vs. α for 4414_sin_0.05t_0.4_100 and NACA 4414

It was assumed that the poor performance of model 4414_sin_0.05t_0.4_100 was due to the high amplitude at the front root. Hence model 4414_sin_0.025t_0.4_100 with a 50% reduced amplitude was created. This assumption was found correct as all the variables C_L, C_D, and C_L/C_D ratio were improved from the previous model. The lift curve in Figure 65 shows that the model stalled at an angle of attack 16° with an increase in maximum C_L value, while the previous model stalled at 12°. However, the model did not outperform the base model as it stalled at the 16° angle of attack and the subsequent fall of lift and increase of drag were very fast, which resulted in a drastic fall of the lift to drag ratio. At the angle of attack 0°, the 4414_sin_0.025t_0.4_100 tubercle model had a 1.99% higher lift to drag ratio than the NACA 4414 base airfoil, but the base airfoil had a higher lift to drag ratio for the rest of the angles of attack.

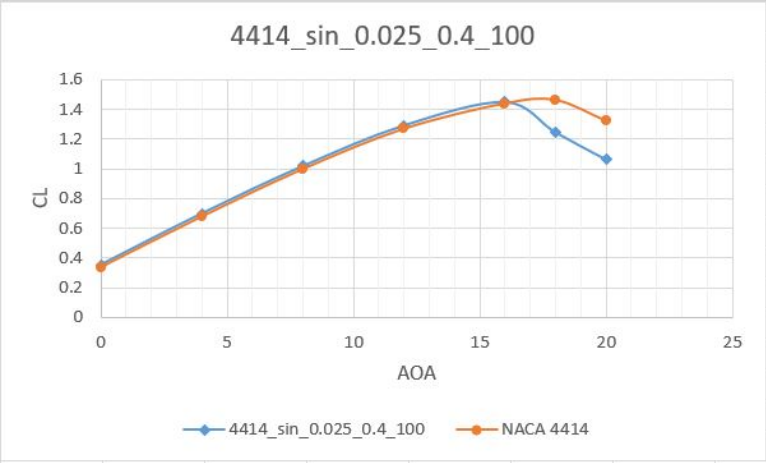

Figure 65: C_L vs. α for 4414_sin_0.025t_0.4_100 and NACA 4414

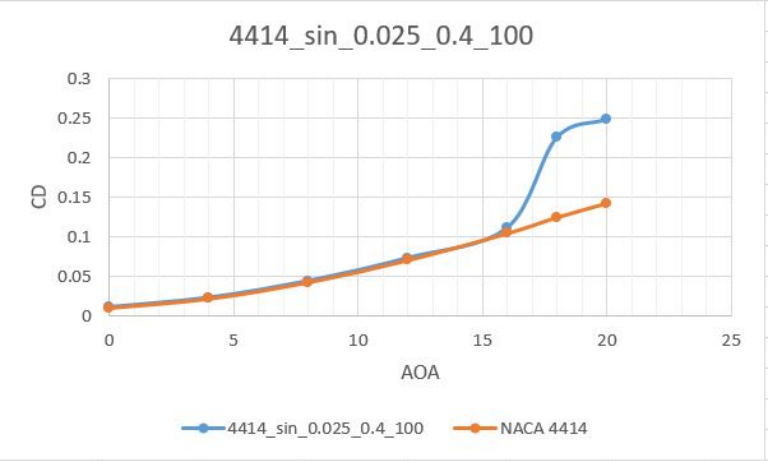

Figure 66: C_D vs. α for 4414_sin_0.025t_0.4_100 and NACA 4414

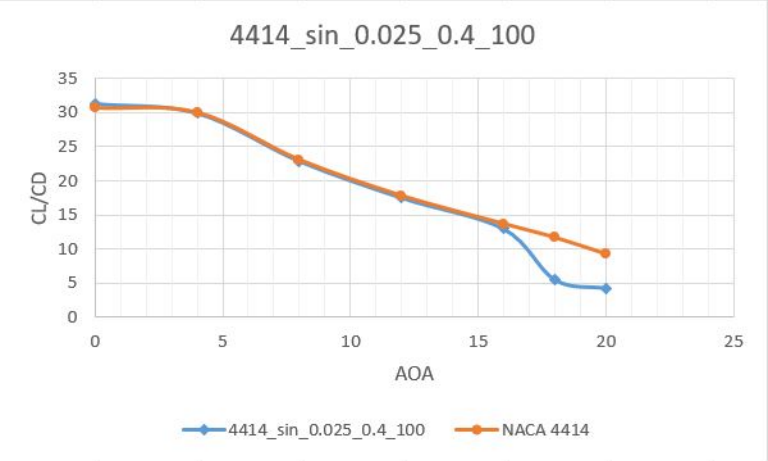

Figure 67: C_L/C_D vs. α for 4414_sin_0.025t_0.4_100 and NACA 4414

Streamline were plotted in terms of velocity at all angles of attack for the model 4414_sin_0.025t_0.4_100, which can be seen in Figures 68 to 74. A non-uniform distribution of velocity was observed over the top surface of the airfoil. On the left side of the airfoil, the distribution of the velocity was uniform; this was due to the straight leading edge of the left side of the airfoil. But, on the right side, shades of high velocity red zone and low velocity yellow zone are clearly visible. At high angles of attack such as 16° and higher, early flow separation was observed on the right side. However, at 20° the flow started separating almost

at the leading edge of the airfoil, as shown in Figure 74. These clearly explains that the stall took place due to the leading-edge flow separation by the high amplitude tubercles.

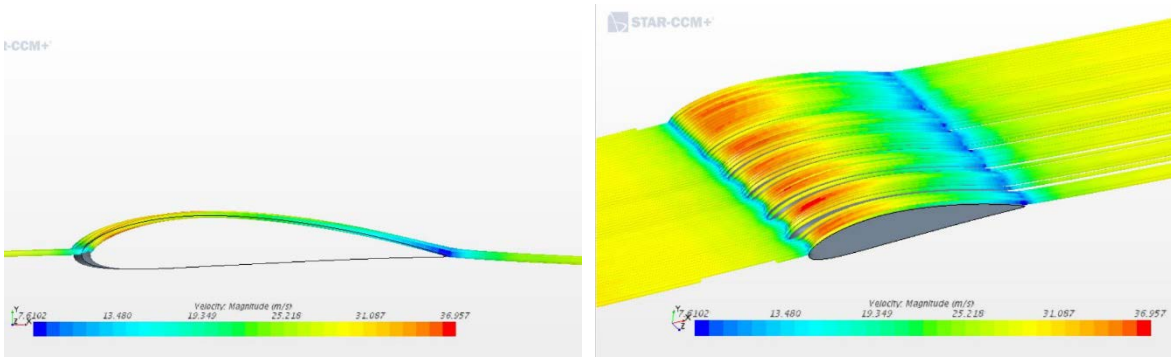

Figure 68: 4414_sin_0.025t_0.4_100 streamlines at α=0°

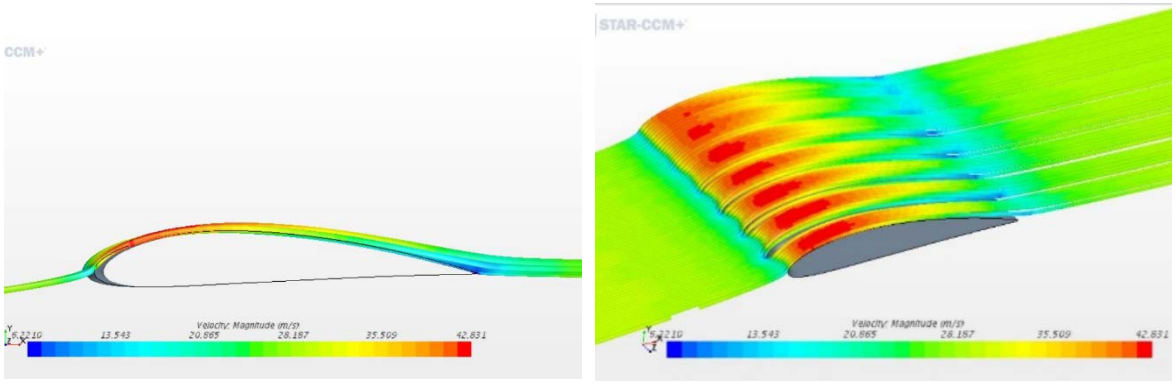

Figure 69: 4414_sin_0.025t_0.4_100 streamlines at α=4°

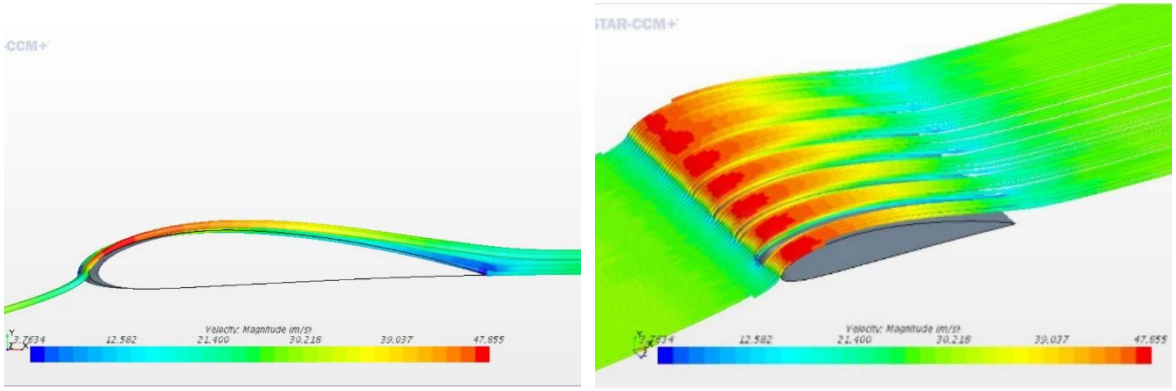

Figure 70: 4414_sin_0.025t_0.4_100 streamlines at α=8°

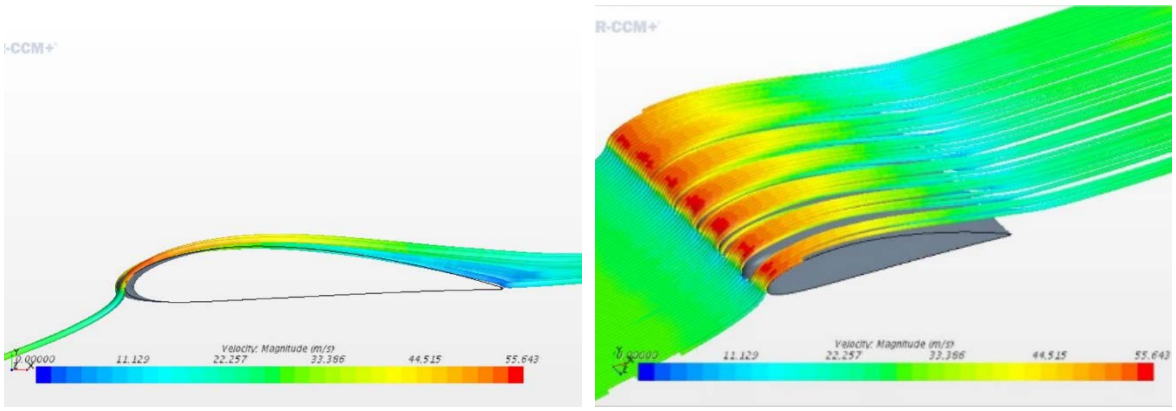

Figure 71: 4414_sin_0.025t_0.4_100 streamlines at α=12°

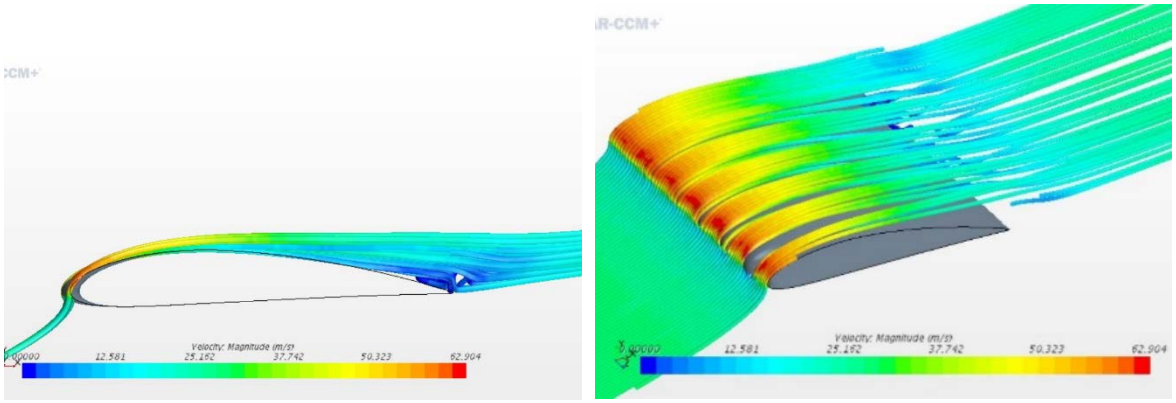

Figure 72: 4414_sin_0.025t_0.4_100 streamlines at α=16°

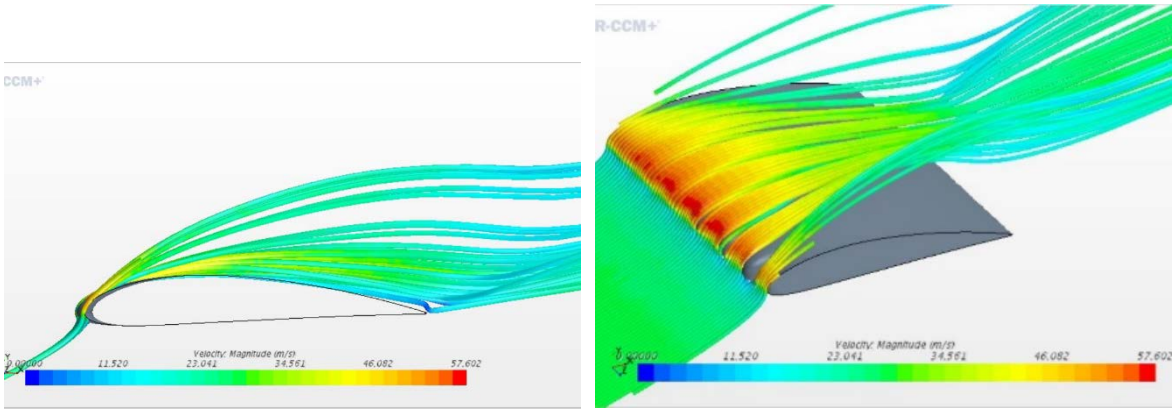

Figure 73: 4414_sin_0.025t_0.4_100 streamlines at α=18°

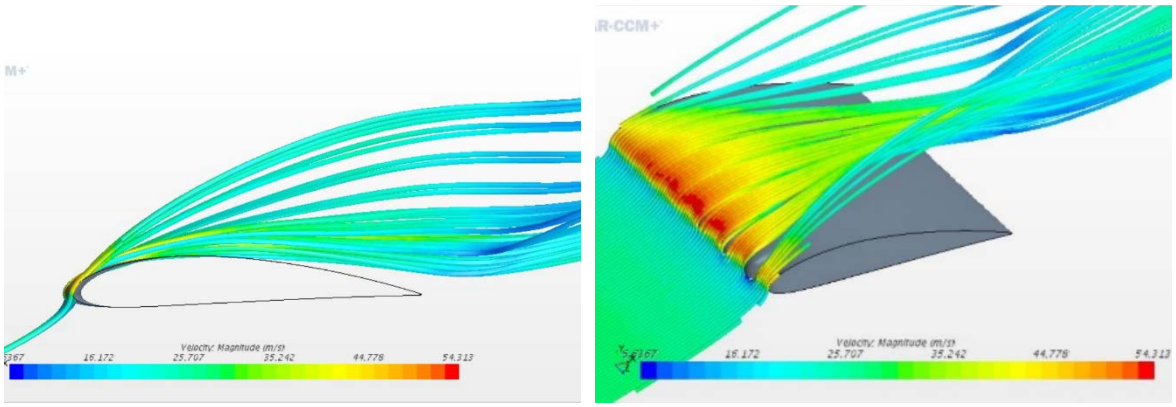

Figure 74: 4414_sin_0.025t_0.4_100 streamlines at α=20°

As it was found that reducing the amplitude was assisting the performance enhancement, model 4414_sin0.015t_0.4_100 with a maximum tubercle amplitude of 1.5% of the chord length was created. Performance enhancement was significantly improved for this model in terms of the lift coefficient. From Figure 75 of the lift versus angle of attack plot, it can be seen that the lift coefficient was higher than the NACA 4414 airfoil for angles of attack until 18°. The stall angle was also increased to 18°. But again after the stall, drop in lift coefficient was very abrubpt. The highest percentage increase of the C_L value was observed for an angle of attack of 0°, which decreased gradually as the angle of attack increased. Also, at the angle of attack 20°, the drag coefficient jumped by 38.89%, which resulted in the C_L/C_D ratio decreasing by 100.03% as shown in Figures 76 and 77.

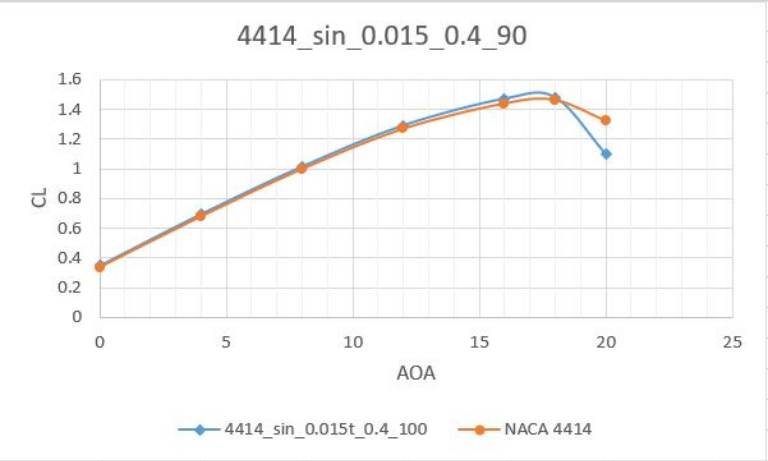

Figure 75: C_L vs. α for 4414_sin_0.015t_0.4_100 and NACA 4414

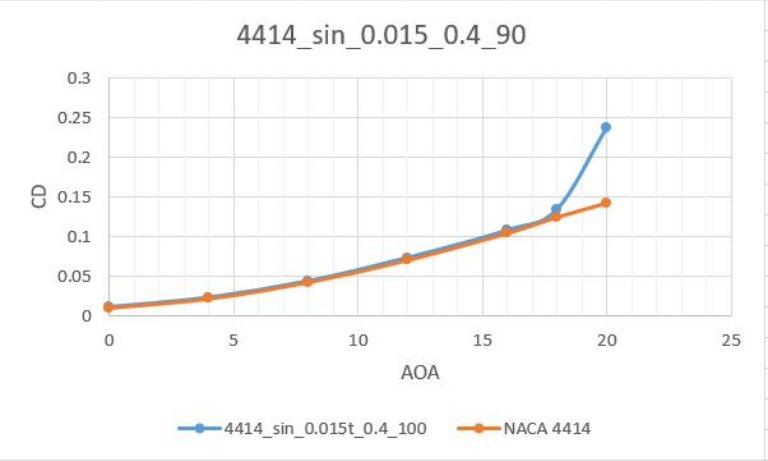

Figure 76: C_D vs. α for 4414_sin_0.015t_0.4_100 and NACA 4414

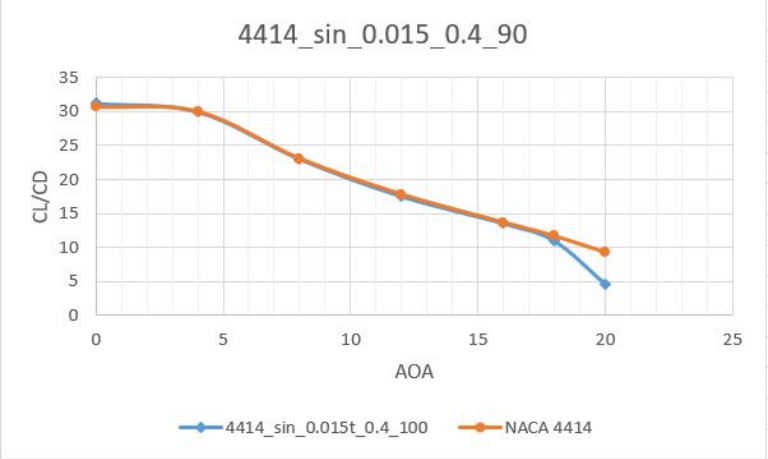

Figure 77: C_L/C_D vs. α for 4414_sin_0.015t_0.4_100 and NACA 4414

Streamlines in terms of velocity were plotted for all tested angles of attack for the 4414_sin_0.015t_0.4_100 model, which can be seen in Figures 78 to 84. Due to the reduction of the maximum amplitude, the difference in velocity distribution was minimized. Flow was more attached to the top surface for lower angles of attack. Swirling was observed at angles of attack of 16° and above at the trailing edge. Flow separation occurred almost at the leading edge at the angle of attack 20°, which can be seen in Figure 84. It is visible from the streamlines that due to the high amplitudes of the tubercles, the flow cannot reach the upper surface of the airfoil. It was concluded from the tested models that although high potential with lift enhancement was visible in the pre-stall zone, the varying amplitude tubercle airfoils provided very poor post-stall lift performance.

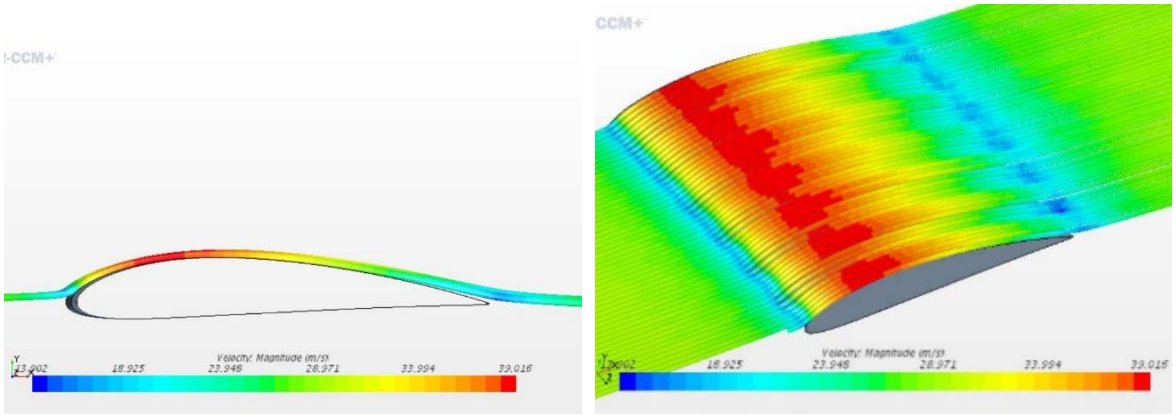

Figure 78: 4414_sin_0.015t_0.4_100 streamlines at α=0°

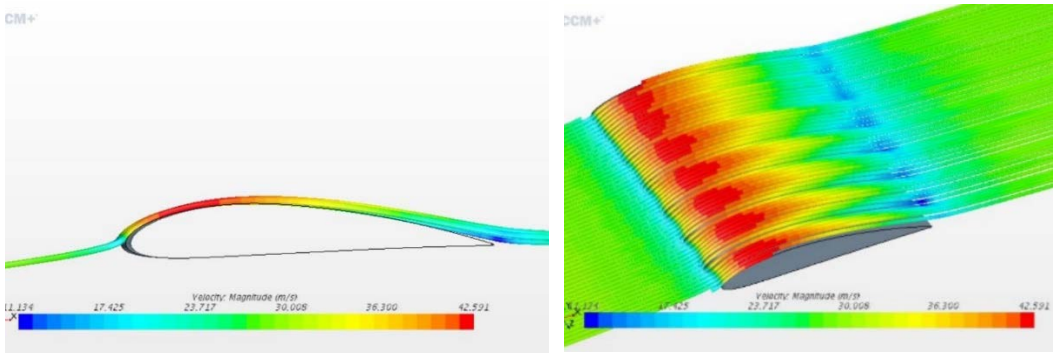

Figure 79: 4414_sin_0.015t_0.4_100 streamlines at α=4°

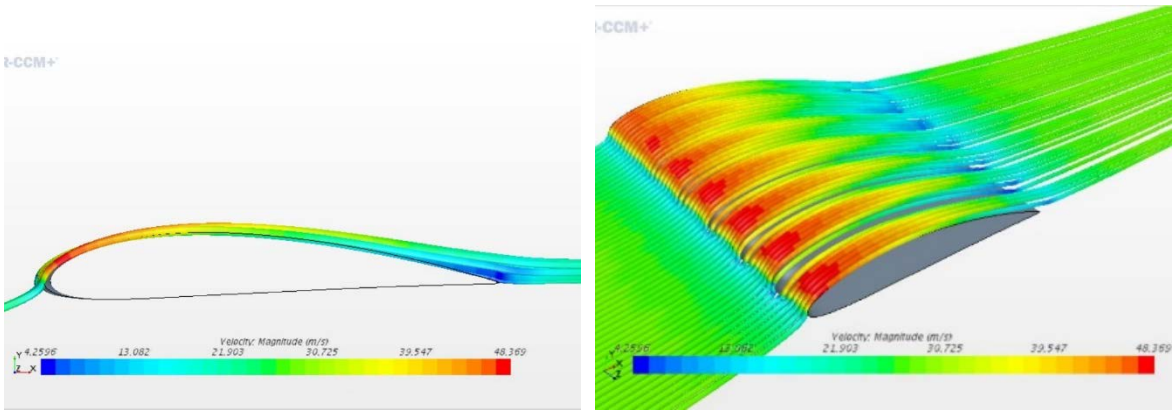

Figure 80: 4414_sin_0.015t_0.4_100 streamlines at α=8°

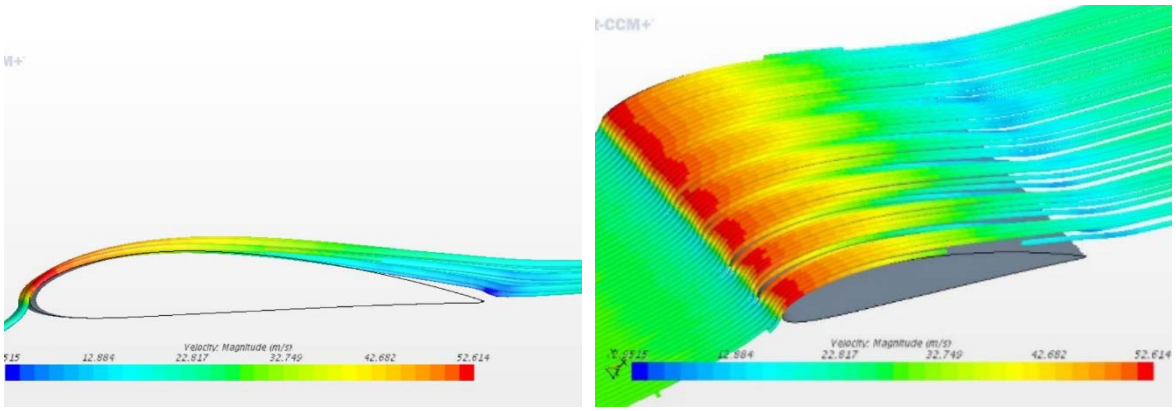

Figure 81: 4414_sin_0.015t_0.4_100 streamlines at α=12°

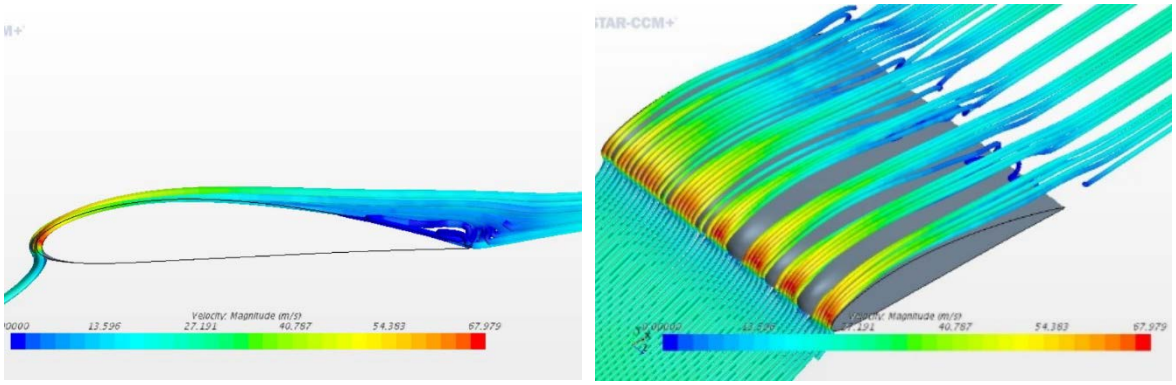

Figure 82: 4414_sin_0.015t_0.4_100 streamlines at α=16°

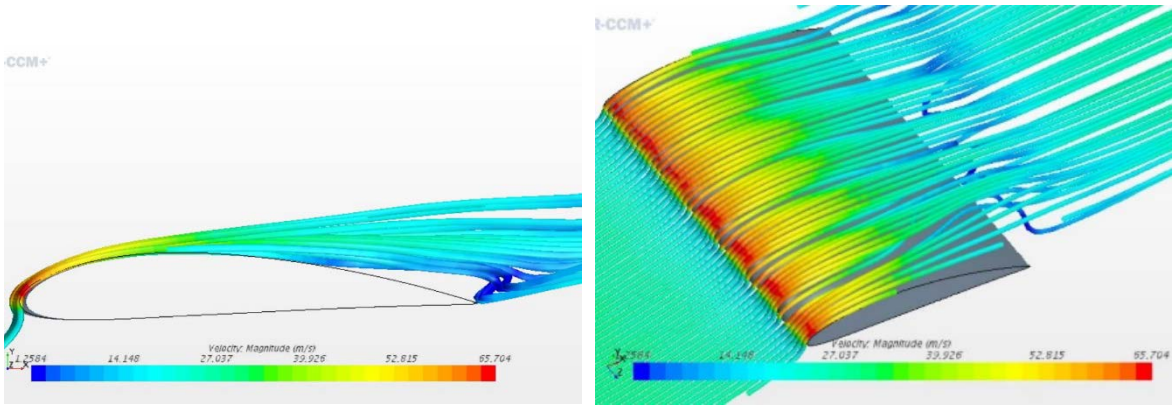

Figure 83: 4414_sin_0.015t_0.4_100 streamlines at α=18°

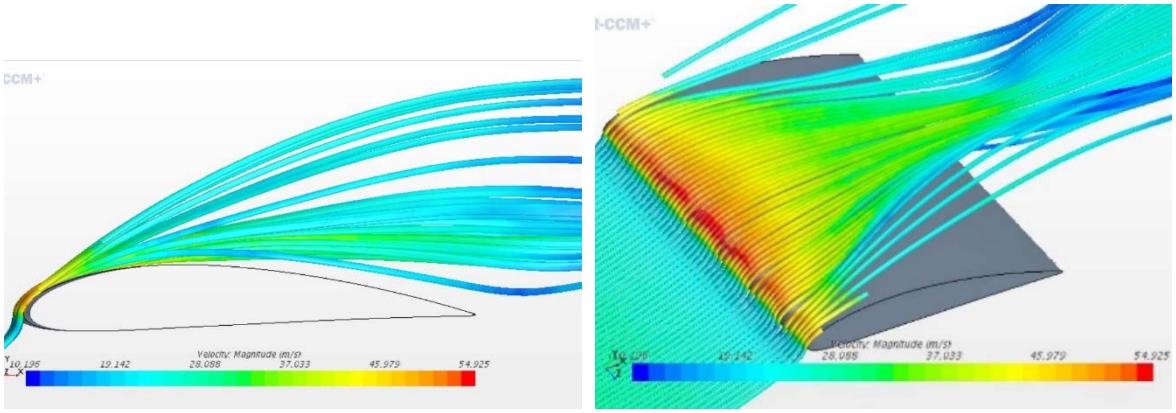

Figure 84: 4414_sin_0.015t_0.4_100 streamlines at α=20°

6.4 Sinusoidal Tubercle Airfoil with Uniform Amplitude & Wavelength

Several sinusoidal tubercle models with constant amplitude and wavelength were tested in this study. The test results of the model 4414_sin_1_0.4_150 are discussed here. From the lift coefficient versus angle of attack plot in Figure 85, it was observed that the model maintained a higher lift coefficient throughout all the angles of attack until 18° compared to the base NACA 4414 airfoil. However, stall took place at an angle of attack of 16°, which is earlier than the base airfoil. The maximum increase in the lift coefficient from the base airfoil was found 4.77% at the angle of attack 0 ° and the difference decreased continuously until the 12° angle of attack.

Between 12° and 20°, the lift coefficient of the tubercle airfoil became higher and lower than the base airfoil. The drag coefficient was higher than the base airfoil for all angles of attack for this model, which can be seen in Figure 86. Deviation of the drag curve from the base airfoil rapidly increased after an angle of attack of 16°. Due to this high drag coefficient, the lift to drag ratio was lower for this model despite having a higher or almost equal lift coefficient, which is shown in Figure 87.

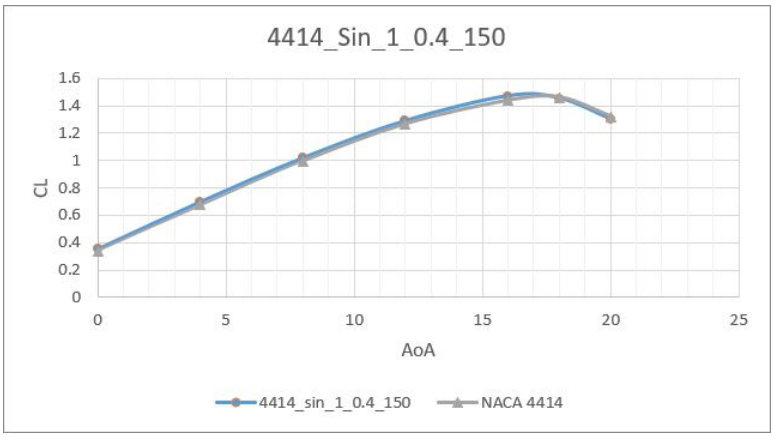

Figure 85: C_L vs. α for 4414_sin_1_0.4_150 and NACA 4414

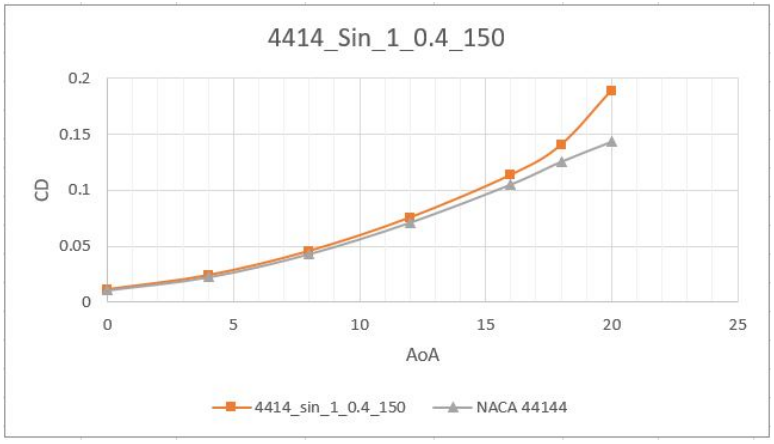

Figure 86: C_D vs. α for 4414_sin_1_0.4_150 and NACA 4414

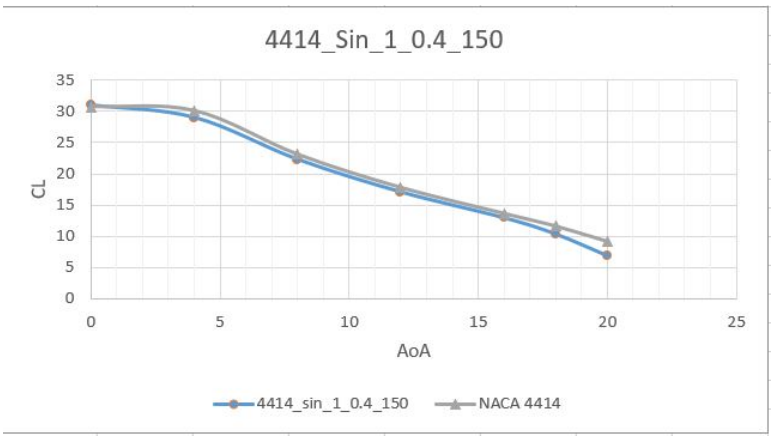

Figure 87: C_L/C_D vs. α for 4414_sin_1_0.4_150 and NACA 4414

Velocity contour plots for the 4414_Sin_1_0.4_150 model with angles of attack between 4° to 18° at plane YZ-X80 are shown in Figures 88 to 90. This airfoil produced a sinusoidal wavy like wake zone which started at an 8° angle of attack. The alternative tubercle airfoils and the varying amplitude tubercle airfoils also provided narrow wake zone, but they were not sinusoidal like this model. The wavy wake zone suggests that tubercles energized the separation zone air to stay attached to the surface at specific locations. It was observed that the narrow zones are behind the crest of the tubercles. At higher angles of attack the wavy wake zone pattern became more visible.

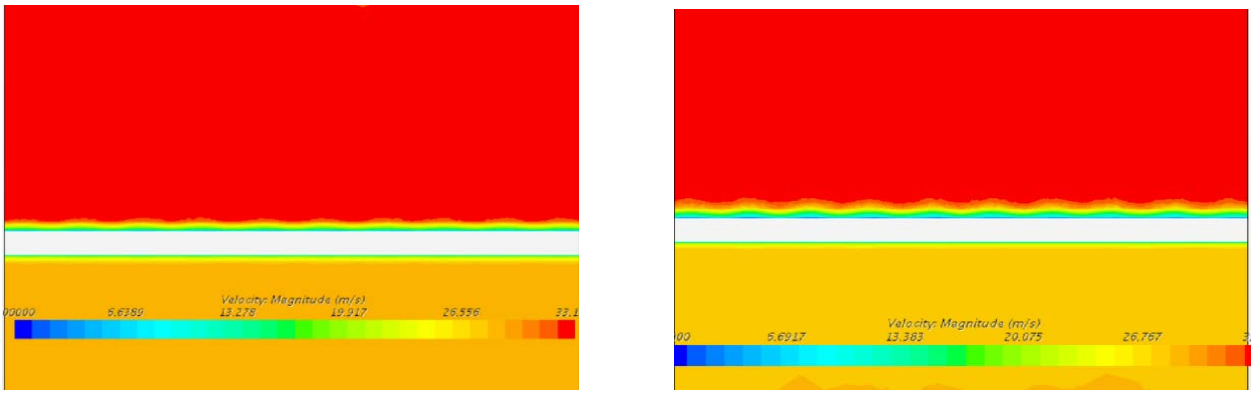

Figure 88: 4414_sin_1_0.4_150; Velocity contour at YZ-X80, α=4° (left); α=8° (right)

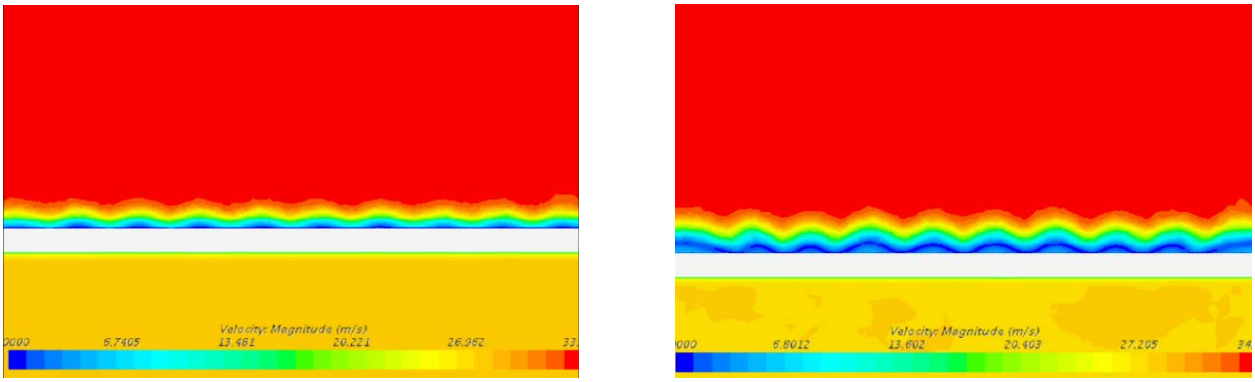

Figure 89: 4414_sin_1_0.4_150; Velocity contour at YZ-X80, α=12° (left); at α=16° (right)

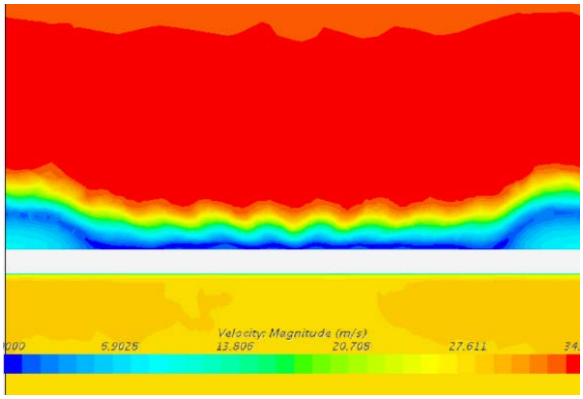

Figure 90: 4414_sin_1_0.4_150; Velocity contour at YZ-X80, at α=18°

Vector contour plots were taken at plane XY-Z43 to observe the flow separation zone behind crest and at plane XY-Z36 to observe flow separation zone behind trough. For each angle of attack vector contour plots at these two planes are shown side by side in Figures 91 to 95. The side by side presentation helps to understand the difference in flow at the crest and trough and the behavior of the air after passing the tubercle bumps. For all angles of attack, it was observed that the flow over the top surface was more attached at plane XY-Z43 (crest) than plane XY-Z36 (trough). Velocity contours taken at YZ-X80 plane also showed similar result that the narrow wake zone was created behind the crest. But it is observed that the maximum velocity at plane XY-Z43 was always lower than the maximum velocity at plane XY-Z36 for same angle of attack. This means that the velocity of air was maximum at the trough region. Hence,

the overall analysis suggests that although maximum velocity was created at the trough zone, due to the interaction of air coming from opposite directions, vortices created and they moved behind the crest area.

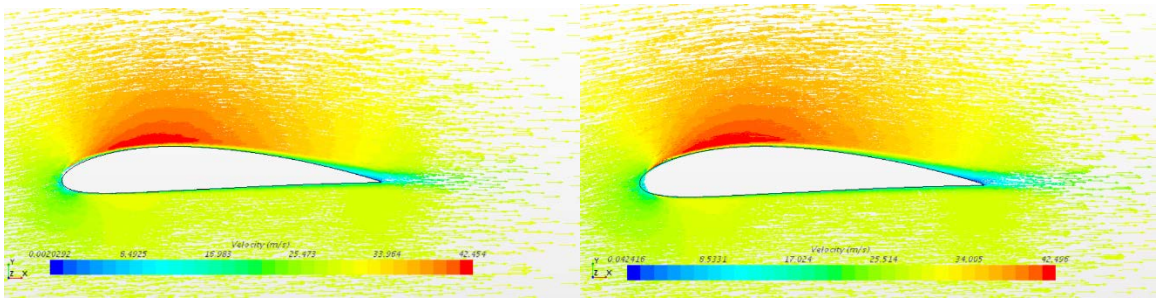

Figure 91: 4414_sin_1_0.4_150; velocity vector for α=4°; plane XY-Z43 (left); plane XY-Z36 (right)

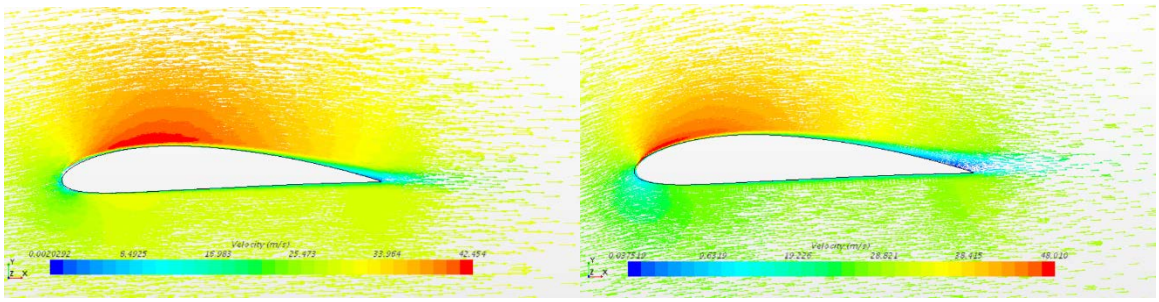

Figure 92: 4414_sin_1_0.4_150; velocity vector for α=8°; plane XY-Z43 (left); plane XY-Z36 (right)

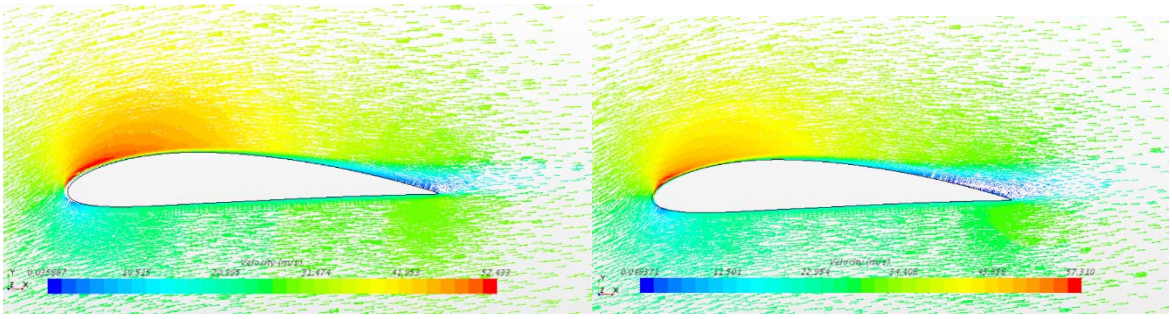

Figure 93: 4414_sin_1_0.4_150; velocity vector for α=12°; plane XY-Z43 (left); plane XY-Z36 (right)

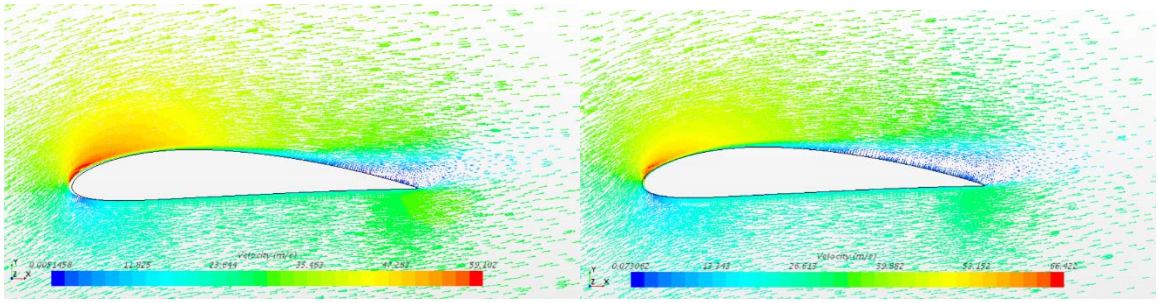

Figure 94: 4414_sin_1_0.4_150; velocity vector for α=16°; plane XY-Z43 (left); plane XY-Z36 (right)

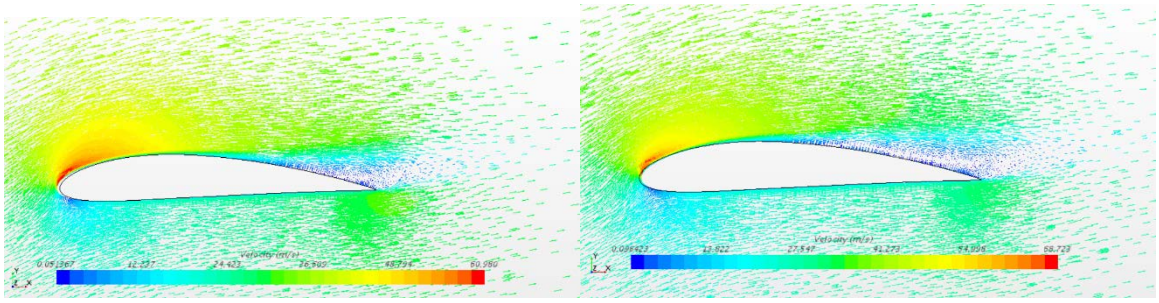

Figure 95: 4414_sin_1_0.4_150; velocity vector for α=18°; plane XY-Z43 (left); plane XY-Z36 (right)

In Figure 96, two close-up views of the vector contour plots at the leading edge of the model 4414_sin_1_0.4_150 are shown. The left picture shows vectors at the crest and right picture shows vectors at the trough zone, both for the angle of attack 18°. The red arrows in the left picture represent high magnitude velocity vectors flowing in a uniform direction at the crest of the tubercle. The high magnitude vectors of the trough plane seem scattered, trying to move to the crosswise direction. These two images confirm that the air at the trough zone was moved behind the crest, which is why the air was more attached behind the crest surface despite the lower kinetic energy.

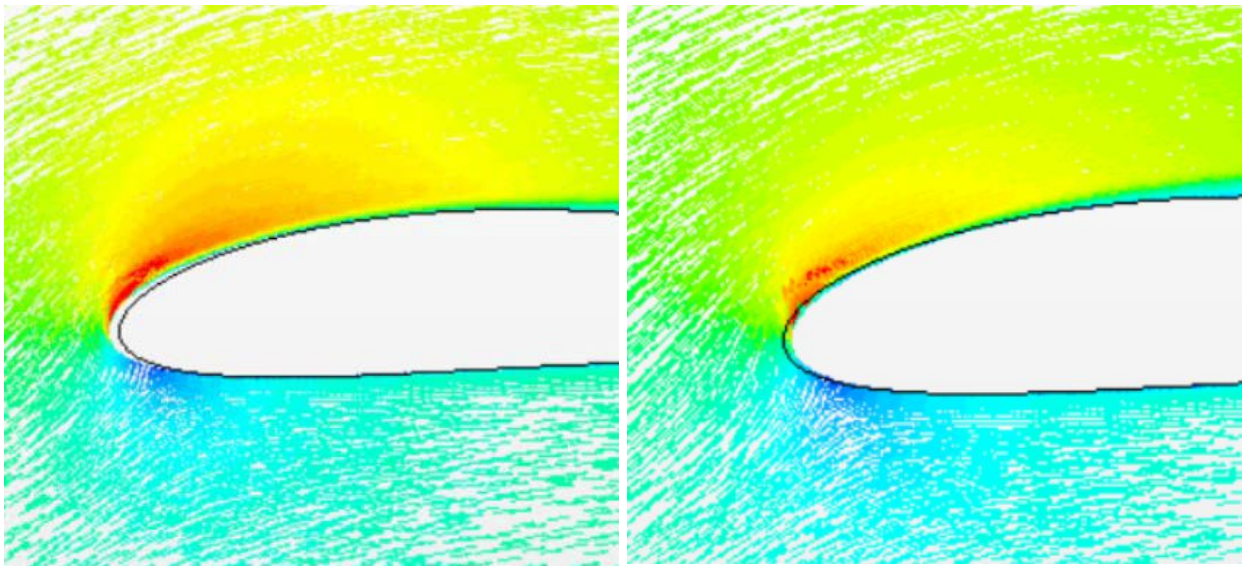

Figure 96: Close-up views of velocity vector at leading edge of 4414_sin_1_0.4_150 tubercles for α=18°; XY-Z43 (left); XY-Z36 (right)

6.5 Effect of Amplitude

As the magnitude of the amplitude and wavelength are two key variables in a uniform sinusoidal tubercle airfoil, a study was carried out to find the optimum value for these variables. To observe the effect of amplitude on the tubercle airfoil performance, several airfoil models were created with different amplitudes keeping the wavelength fixed. Tubercle models 4414_sin_0.6_0.4_100, 4414_sin_1_0.4_100, 4414_sin_2_0.4_100, 4414_sin_3_0.4_100, and 4414_sin_4_0.4_100, with amplitudes of 0.6%, 1%, 2%, 3%, and 4% of the chord length and a fixed wavelength of 15.70% of the chord length were tested with the same physics conditions. The tubercle model with the smallest amplitude of 0.6% of the chord length provided higher lift coefficient and lower drag coefficient compared to other models, which can be seen from the lift plot in Figure 97 and the drag plot in Figure 98. Stall was delayed the most for this model. The lift and drag coefficients were quite similar before 12° angle of attack for all models. Changes started to take place after the angle of attack 12° for the models with higher

amplitudes. In Figure 97, the comparison plot of lift coefficient versus angle of attack shows that the lift coefficient of model 4414_sin_3_0.4_100 and 4414_sin_4_0.4_100 dropped abruptly after the 12° angle of attack. The stall angle of these models was also reduced significantly. The drag coefficient maintained a close match for angles of attack below 12°, which can be seen in Figure 98. After the 12° angle of attack the drag coefficient increased randomly for higher amplitude models. The model 4414_sin_0.6_0.4_100 maintained a smooth hyperbolic C_D curve with no sudden changes even after the stall. From the plot of the lift to drag ratio in Figure 99, it was observed that although high amplitude models provided high C_L/C_D ratios at the beginning, they performed poorly at high angles of attack due to a low lift coefficient and high drag coefficient. On the other hand, the smallest amplitude model maintained a smooth C_L/C_D curve with steady performance at an angle of attack of 20°. This analysis suggests that smaller amplitudes provide better aerodynamic performance by improving the post stall lift coefficient.

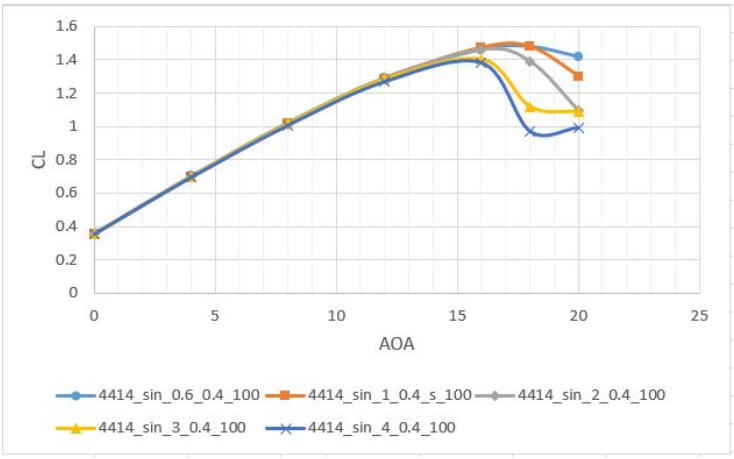

Figure 97: C_L vs. α comparison plot of 4414_sin_0.6_0.4_100, 4414_sin_1_0.4_100, 4414_sin_2_0.4_100, 4414_sin_3_0.4_100, and 4414_sin_4_0.4_100

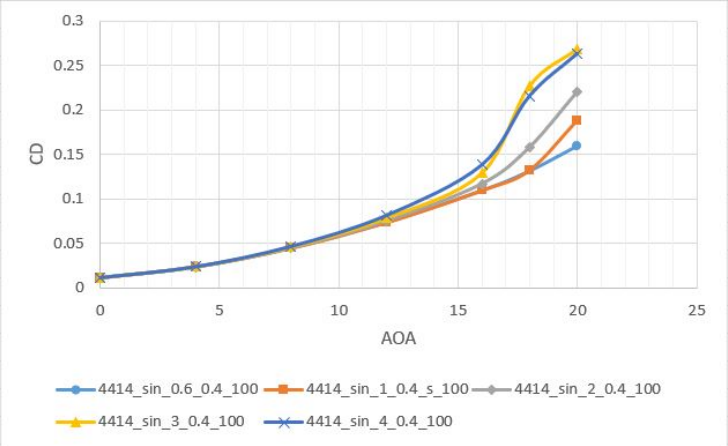

Figure 98: C_D vs. α comparison plot of 4414_sin_0.6_0.4_100, 4414_sin_1_0.4_100, 4414_sin_2_0.4_100, 4414_sin_3_0.4_100, and 4414_sin_4_0.4_100

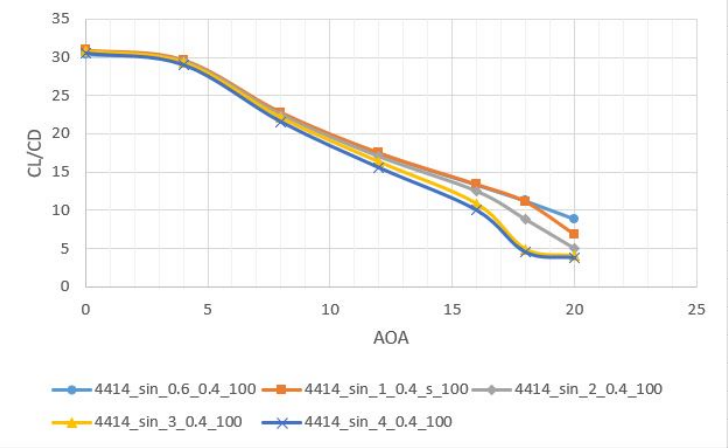

Figure 99: C_L/C_D vs. α comparison plot of 4414_sin_0.6_0.4_100, 4414_sin_1_0.4_100, 4414_sin_2_0.4_100, 4414_sin_3_0.4_100, and 4414_sin_4_0.4_100

6.6 Effect of Wavelength

To observe the effect of wavelength, models with different wavelengths and a fixed amplitude were created. Tubercle models 4414_sin_1_0.2_100, 4414_sin_1_0.4_100, 4414_sin_1_0.6_100, and 4414_sin_1_0.8_100 with constant amplitude of 1% of the chord length and wavelengths of 31.4%, 15.70%, 10.52%, and 8% of the chord length, respectively, were modeled to test the effect of wavelength. Before 15° angle of attack, all models provided similar lift and drag coefficient values, which is shown in Figures 100 and 101. After the 12°

angle of attack performance variation was observed for different models. Airfoils 4414_sin_1_0.4_100 and 4414_sin_1_0.6_100 with wavelengths of 15.7% of the chord length and 10.52% of the chord length achieved the maximum lift coefficient but after stall drop was drastic for these models. On the other hand, the larger wavelength model 4414_sin_1_0.2_100 with a wavelength of 31.4% of the chord length showed smooth post stall behavior with gradual declination of lift. The pre-stall lift coefficients of this model were slightly less than the model 4414_sin_1_0.6 _100 that provided the maximum lift coefficient. Tubercle model 4414_sin_1_0.6_100 with a wavelength of 10.52% of the chord length outperformed all other models in terms of lift to drag ratio until the stall angle, which can be seen in Figure 102. Airfoil 4414_sin_1_0.8_100 with a very small wavelength of 8% of the chord length provided small values of lift and larger values of drag. In summary, the model 4414_sin_1_0.2_100 with a wavelength of 31.4% of the chord length provided the best aerodynamic performance in terms of post-stall performance enhancement which suggests that larger wavelength provides better aerodynamic performance.

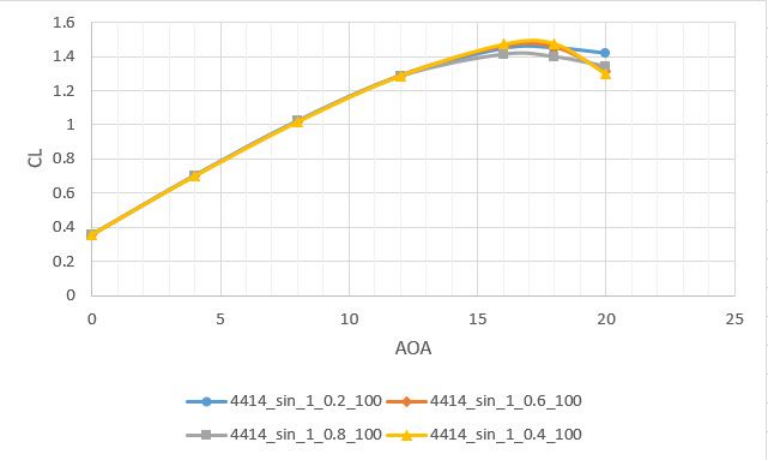

Figure 100: C_L vs. α comparison plot of 4414_sin_1_0.2_100, 4414_sin_1_0.4_100, 4414_sin_1_0.6_100, and 4414_sin_1_0.8_100

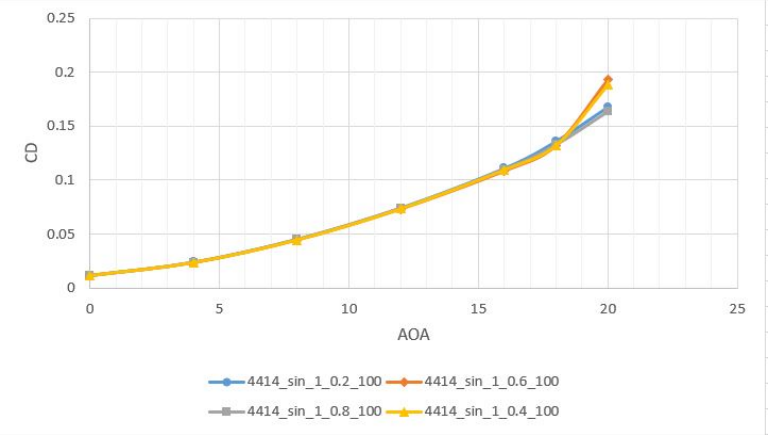

Figure 101: C_D vs. α comparison plot of 4414_sin_1_0.2_100, 4414_sin_1_0.4_100, 4414_sin_1_0.6_100, and 4414_sin_1_0.8_100

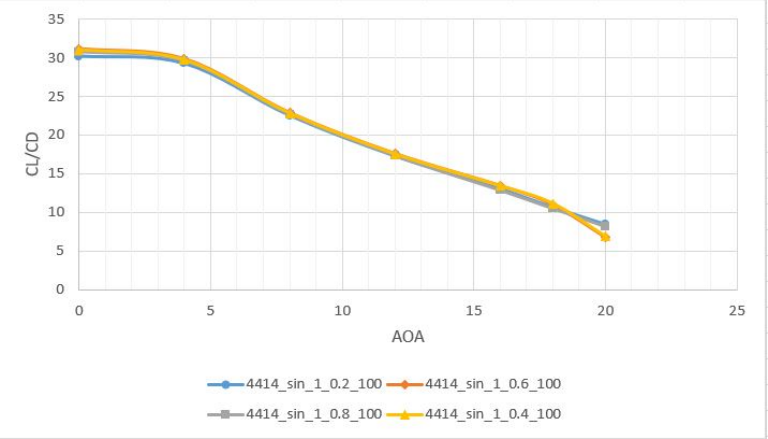

Figure 102: C_L/C_D vs. α comparison plot of 4414_sin_1_0.2_100, 4414_sin_1_0.4_100, 4414_sin_1_0.6_100, and 4414_sin_1_0.8_100

6.7 Effect of Surface Waviness

All sinusoidal tubercle models were generated with SolidWorks surface loft tool. During the execution of surface loft, some wavy shapes were created at the top and bottom surfaces of the airfoil body. An investigation was carried out to observe how this waviness affects the airfoil performance. For this purpose, model 4414_sin_1_0.4_100V2 with no waves at the top and bottom surfaces, and model 4414_sin_1_0.4_100V1 with waves only at the top surface were created and their results compared to the original model, 4414_sin_1_0.4 _100. No difference in the lift curve among the three models was observed until angle of attack of 12°.

After 12° angle of attack, the model with no surface waves continuously gave lower C_L values compared to the original model and the model with top surface waves that can be seen in Figures 103 and 104. This suggests that the surface waviness provides better lift coefficient. The model with waves only at the top surface and the original model had almost similar C_L curves with slightly lower values provided by the former after the stall. From these it can be deduced that the bottom surface waviness is not very influential compared to the top waves. The C_D plot also shows that the smooth model provided higher drag coefficient than the other two models in the post stall region, with no change in the pre-stall zone. The C_L/C_D plot of the no wavy surface airfoil was always below the two wavy models which can be seen in Figure 105. Hence, it was understood from this analysis that surface waviness provides aerodynamic benefits to the tubercle airfoils.

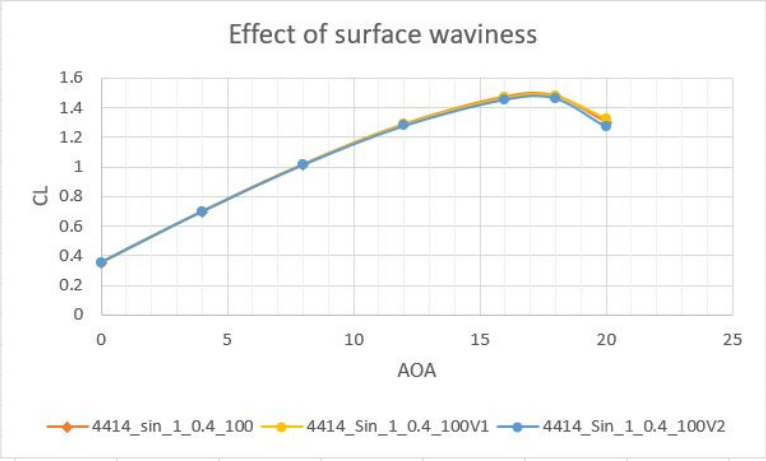

Figure 103: C_L vs. α comparison plot of 4414_sin_1_0.4_100, 4414_sin_1_0.4_100V2, and 4414_sin_1_0.4_100V1

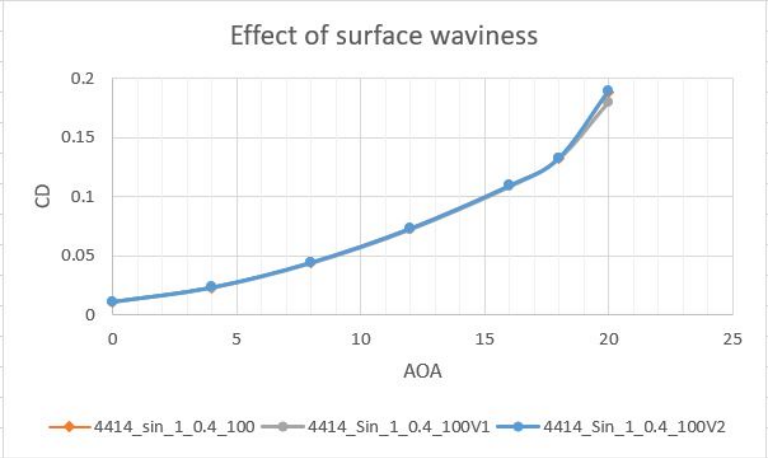

Figure 104: C_D vs. α comparison plot of 4414_sin_1_0.4_100, 4414_sin_1_0.4_100V2, and 4414_sin_1_0.4_100V1

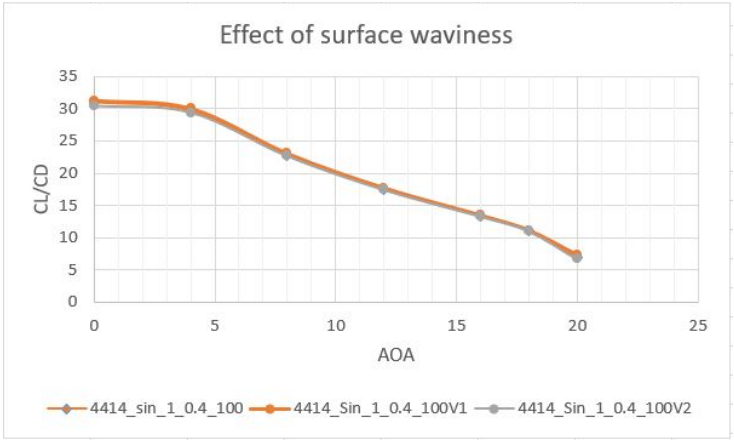

Figure 105: C_L/C_D vs. α comparison plot of 4414_sin_1_0.4_100, 4414_sin_1_0.4_100V2, and 4414_sin_1_0.4_100V1

6.8 Optimum Tubercle Geometry

After analyzing the effect of amplitude and wavelength of sinusoidal tubercle geometry, it was found that the magnitude of the amplitude and wavelength of tubercles both had a significant effect on the performance. From the tested models it was found that amplitude with a magnitude of 0.6% of the chord length and a wavelength of 31.4% of the chord length was most advantageous for significant post stall performance enhancement with a slight enhancement in the pre-stall region. Hence, tubercle model 4414_sin_0.6_0.4_100 was created using the

optimum magnitude of the amplitude and wavelength. For this model, the lift coefficient was found to be higher than the base airfoil for all angles of attack, which can be seen in Figure 106. Although the lift curve of the optimum tubercle looked like it merged on the base airfoil, it was always slightly higher, starting from a high of 4.05% improvement from the base airfoil at the 0° angle of attack. The percent increase of C_L gradually reduced to 0.17% at the angle of attack of 18°. The percent increase of C_L again moved upward to 6.21% at 20° angle of attack thus confirming a superior post-stall lift performance. C_D increased simultaneously along with C_L up to angle of attack of 16°. In the pre-stall region, the maximum percent increase of C_D was recorded as 3.56% at 4° angle of attack which continued a reducing trend up to the angle of attack of 16° where it was still 1.77 % higher. After the 16° angle of attack the C_D started to increase again with a percent increase of 2.70% at angle of attack of 18° and 8.93% at 20°, as shown in Figure 107. For the optimum geometry, the lift to drag ratio showed 0.85% enhancement only at the angle of attack of 0°. For the rest of the angles of attack the ratio was lower than the base airfoil, which is shown in Figure 108. The gain in lift was offset but the increase in drag.

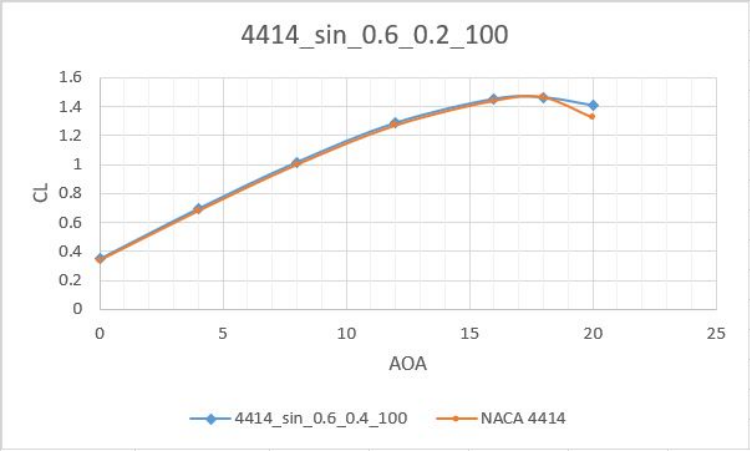

Figure 106: C_L vs. α plot of 4414_sin_0.6_0.2_100 and NACA 4414

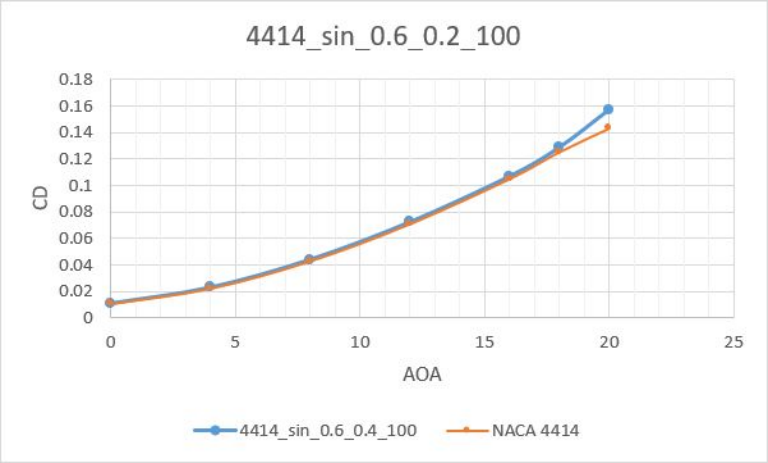

Figure 107: C_D vs. α plot of 4414_sin_0.6_0.2_100 and NACA 4414

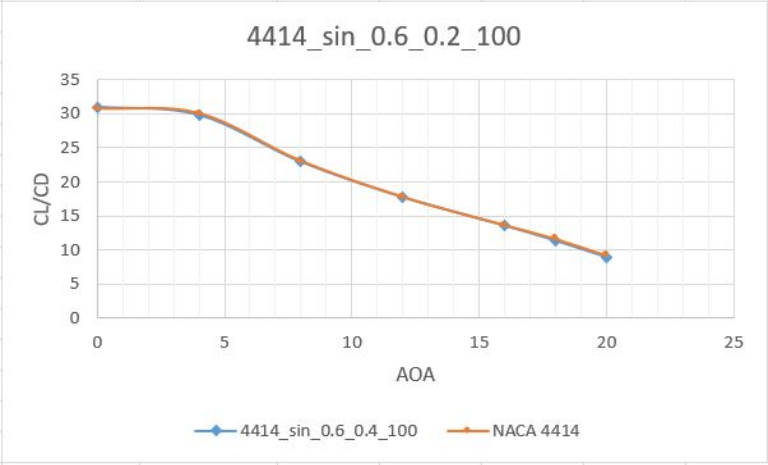

Figure 108: C_L/C_D vs. α plot of 4414_sin_0.6_0.2_100 and NACA 4414

From the velocity contour plots at plane YZ-X80, the overall scenario of wake zone development over the span length was observed in Figures 109 to 112. The maximum velocity for different angles of attack at the same plane was found to be a close match with the maximum velocity of the base NACA 4414 airfoil. For some angles of attack, the maximum velocity of model 4414_sin_0.6_0.2 exceeded the base airfoil. The maximum velocity increased linearly over the increase of angles of attack. There were three bumps in the tubercle model and three narrow wake zones were formed as well in the YZ-X80 contour plots.

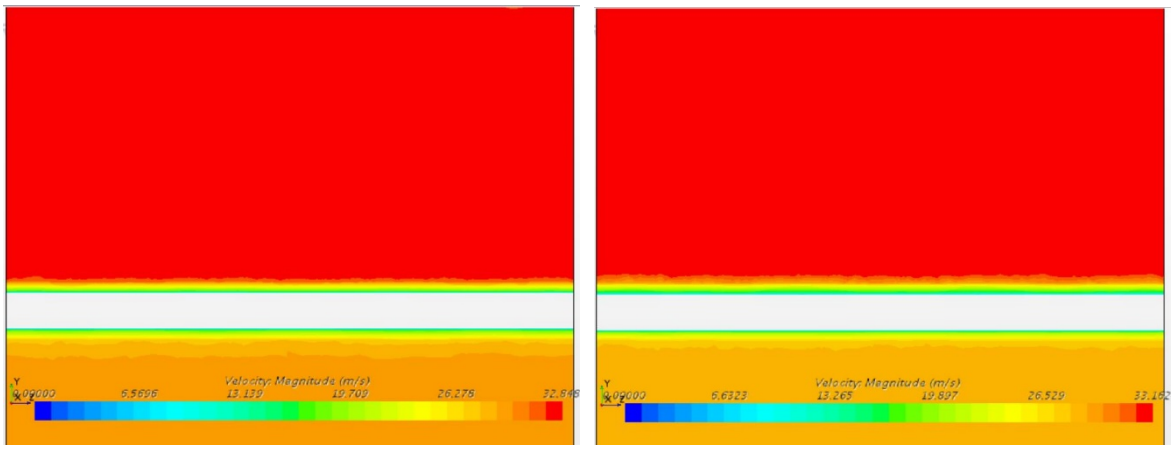

Figure 109: 4414_sin_0.6_0.2_100 velocity contour at plane YZ-X80; α=0° (left) α=4°(right)

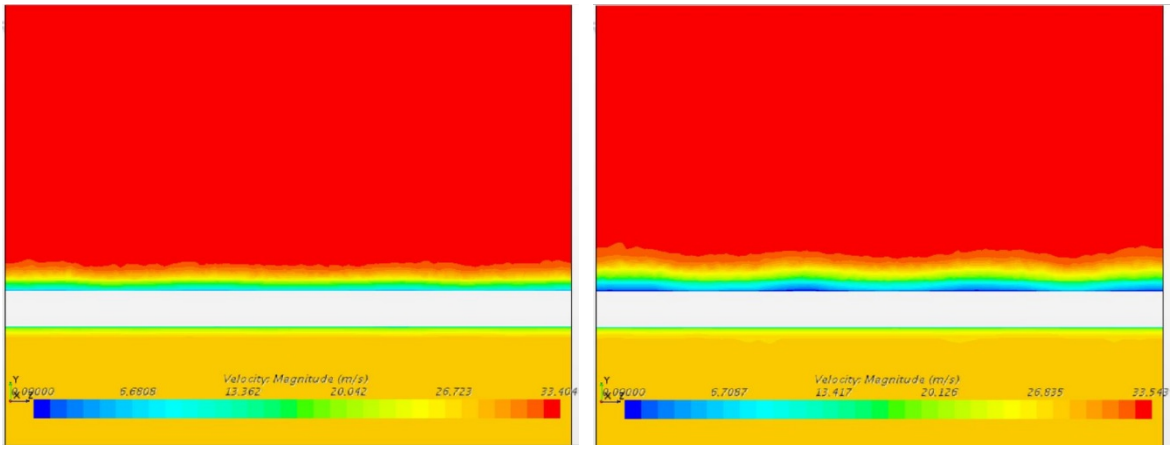

Figure 110: 4414_sin_0.6_0.2_100 velocity contour at plane YZ-X80; α=8° (left) α=12°(right)

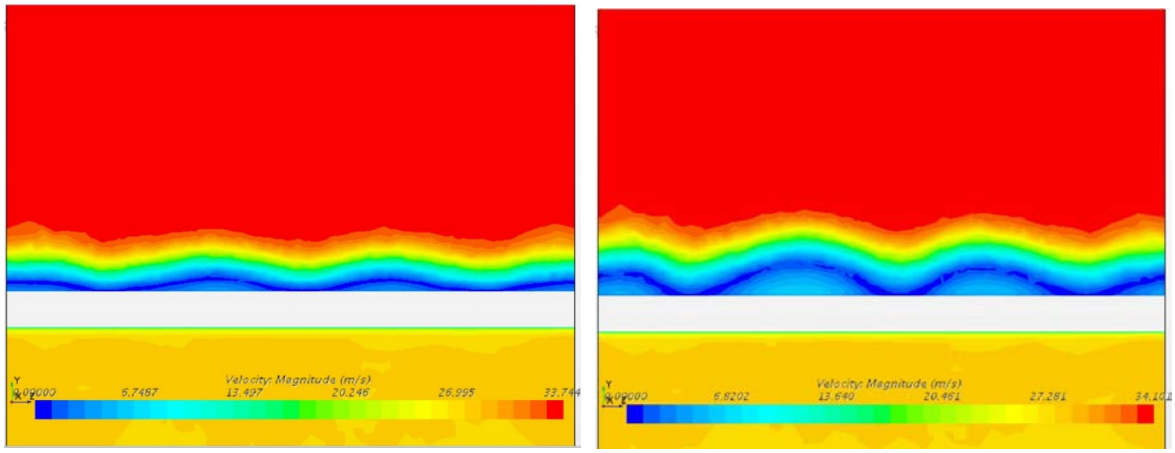

Figure 111: 4414_sin_0.6_0.2_100 velocity contour at plane YZ-X80; α=16° (left) α=18°(right)

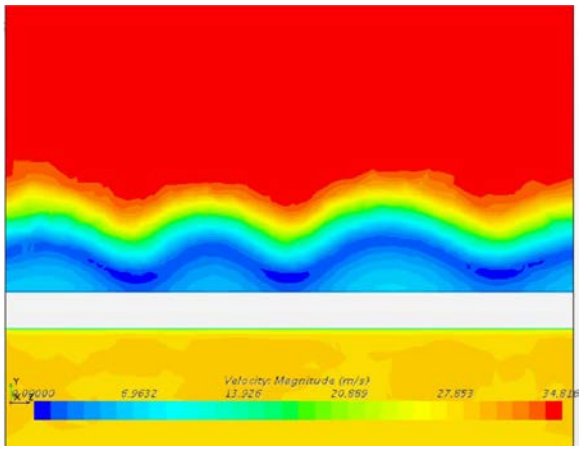

Figure 112: 4414_sin_0.6_0.2_100 velocity contour at plane YZ-X80; α=20°

Velocity contour plots were taken at plane XY-Z52 (crest) and XY-Z35 (trough) to observe the flow behavior after passing the crest and trough of the tubercle, which are shown in Figures 113 to 119. The maximum velocity at the trough was higher than the maximum velocity at the crest. Below an angle of attack of 12° no significant difference was observed between the velocity contours taken on planes at the crest and trough. Beginning from the angle of attack of 12° boundary layer separation started earlier behind the trough. The wake zone behind the trough became wider than the wake zone at the crest. At angles of attack of 18° and 20° significant differences were observed between the wake zone behind the crest and the trough.

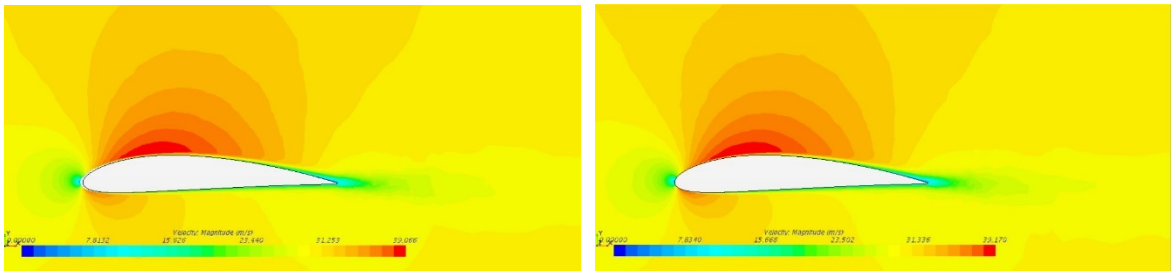

Figure 113: 4414_sin_0.6_0.2_100 velocity contour for α=0°; plane XY-Z 52 (left), plane XY-Z35 (right)

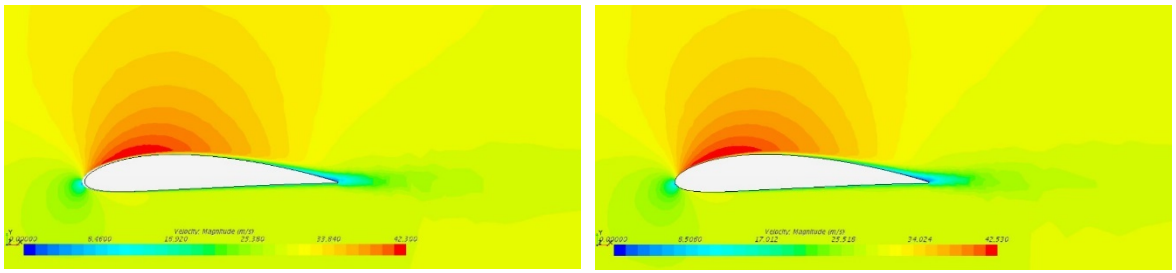

Figure 114: 4414_sin_0.6_0.2_100 velocity contour for α=4°; plane XY-Z52 (left), plane XY-Z36 (right)

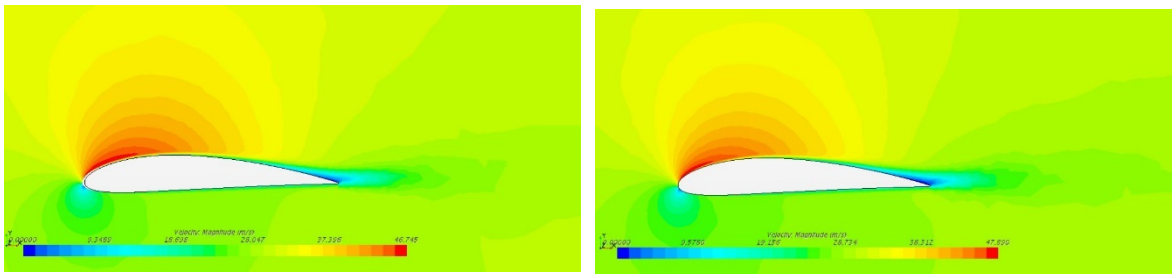

Figure 115: 4414_sin_0.6_0.2_100 velocity contour for α=8°; plane XY-Z52 (left), plane XY-Z36 (right)

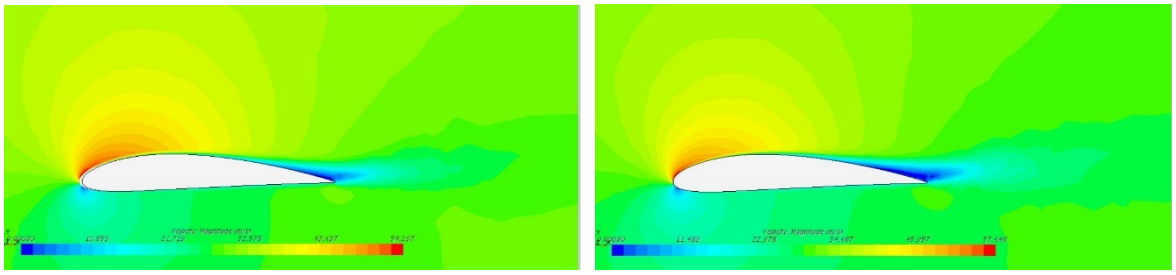

Figure 116: 4414_sin_0.6_0.2_100 velocity contour for α=12°; plane XY-Z52 (left), plane XY-Z36 (right)

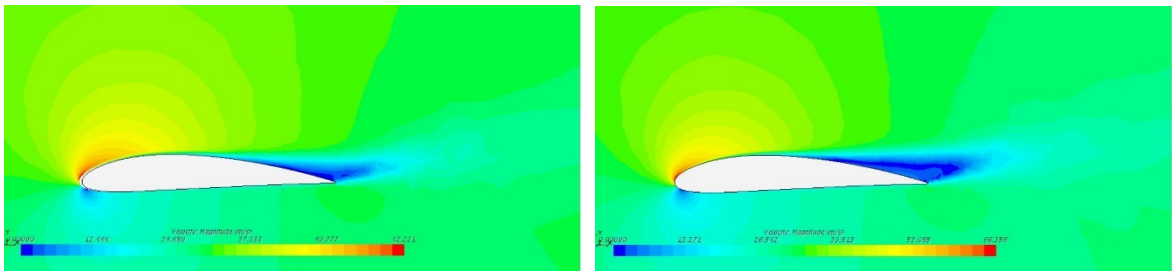

Figure 117: 4414_sin_0.6_0.2_100 velocity contour for α=16°; plane XY-Z52 (left), plane XY-Z36 (right)

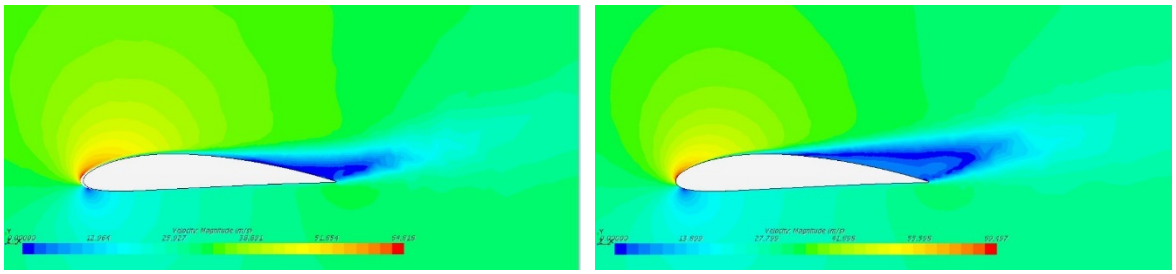

Figure 118: 4414_sin_0.6_0.2_100 velocity contour for α=18°; plane XY-Z52 (left), plane XY-Z36 (right)

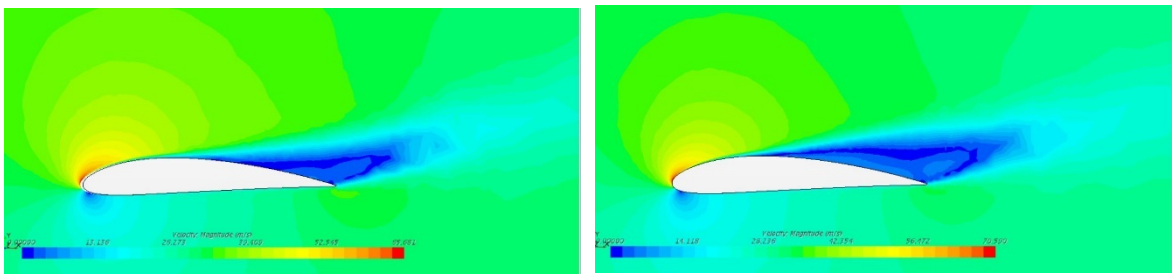

Figure 119: 4414_sin_0.6_0.2_100 velocity contour for α=20°; plane XY-Z52 (left), plane XY-Z36 (right)

Streamlines in terms of velocity magnitude were plotted around the airfoil body, which can be seen in Figures 120 and 121 for angles of attack of 12°, 16°, 18°, and 20°. The change in flow behavior started after an angle of attack of 12° where the flow over the airfoil looked equally distributed. At the angle of attack of 16° a non-uniform distribution of flow was observed over the top surface. Behind the crest, low-velocity air was found very close to the leading edge, but flow was attached to the airfoil. However, behind the trough the low-velocity zone appeared far from the leading edge, but at the same time the flow moved away from the top surface. These differences in flow behind the crest and the trough created a wavy layer of the stream of flow near the trailing edge.

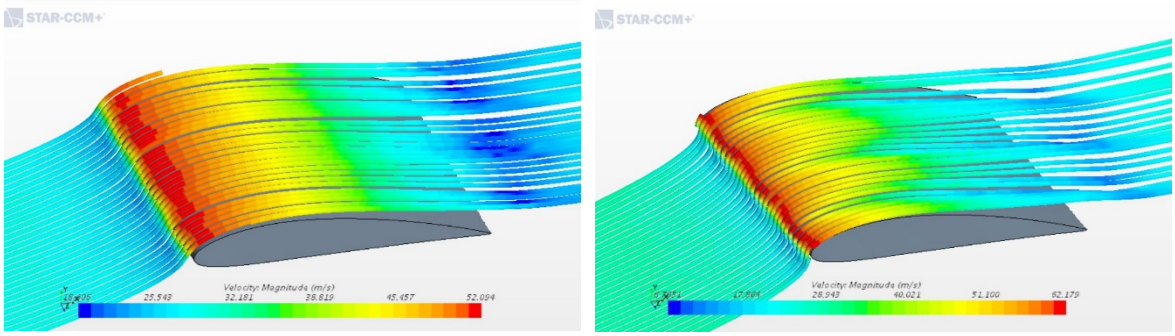

Figure 120: 4414_sin_0.6_0.2_100 streamline; α=12° (left), α=16° (right)

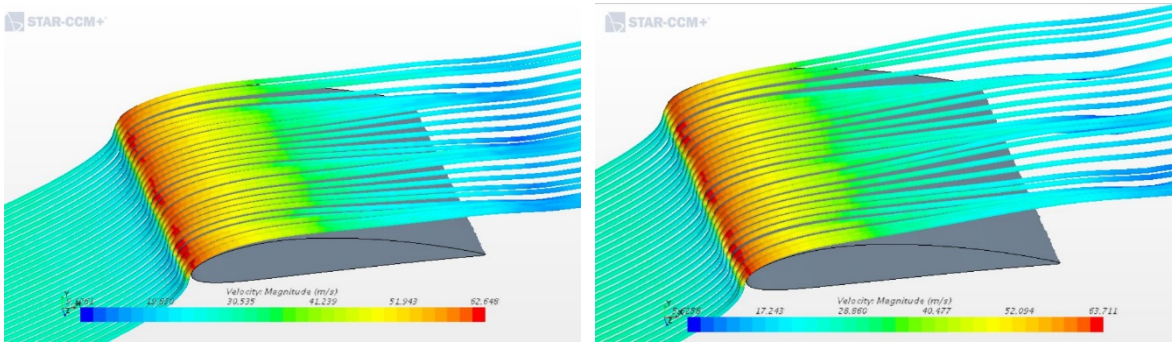

Figure 121: 4414_sin_0.6_0.2_1000 streamline; α=18° (left), α=20° (right)

6.9 Effect of Reynolds Number

To check how the tubercle airfoil behaves for various Reynolds numbers, the optimum tubercle model was scaled to a chord length of 1 m and a span length of 1 m. Then by only changing the velocity of the stream, Reynolds numbers were varied to $1x10^6$, $5x10^6$ and $10x10^6$ ($1x10^7$). For Re=$1x10^6$ stall took place at an 18° angle of attack like the model simulated with Re=$2x10^5$ for a chord length of 0.1 m. But at Re of $5x10^6$ and $10x10^6$ the airfoil did not stall that early. Hence simulations were carried out for angles of attack up to 28°. The values of C_L, C_D, and C_L/C_D versus the angle of attacks for three different Reynolds number were plotted together for comparison in Figures 122 to 124, respectively. The highest lift coefficient was generated by Reynolds number of $10x10^6$ at all angles of attack as can be seen

in Figure 122. It was observed that the airfoil stalled at a very high angle of attack of 24° for both Reynolds numbers of $5x10^6$ and $10x10^6$. However, no significant change was observed in the drag curve before an angle of attack of 20°, as shown in Figure 123. After 20°, drag increased abruptly for Re=$1x10^6$ while for the other two Reynolds numbers drag steadily increased together with a slight increase by Re=$10x10^6$ beginning at the angle of attack of 24°. The reduction in wake zone for the higher Re values was reducing the pressure drag. As the lift coefficient was the maximum for the highest Reynolds number with the same drag coefficient, the lift to drag ratio was also found to be a maximum for the highest Reynolds number of $10x10^{6,}$.

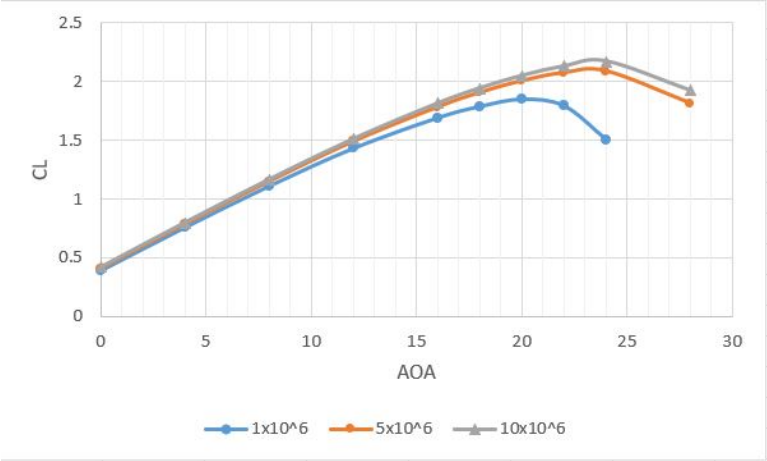

Figure 122: C_L vs. α comparison plot for Reynolds numbers of $1x10^6$, $5x10^6$, and $10x10^6$

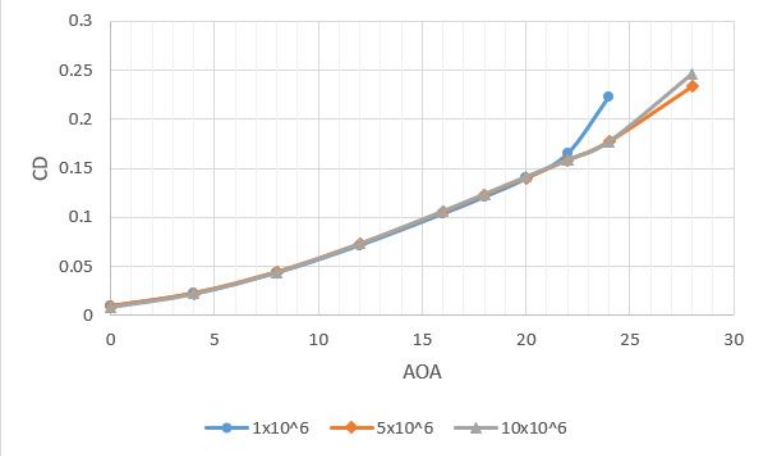

Figure 123: C_D vs. α comparison plot for Reynolds numbers of $1x10^6$, $5x10^6$, and $10x10^6$

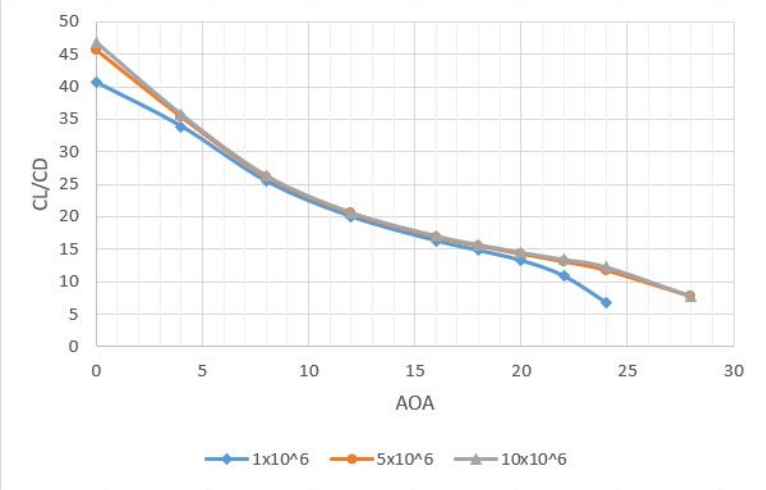

Figure 124: C_L/C_D vs. α comparison plot for Reynolds numbers of $1x10^6$, $5x10^6$, and $10x10^6$

Streamlines were generated at selected angles of attack to better understand flow behavior over the airfoil due to varying Reynolds numbers. In Figure 125, for the Reynolds number $1x10^6$ and at angle of attack 16°, the flow over the airfoil was in close attachment to the top surface, although it was clearly visible that the velocity was not uniformly distributed in the mid surface. This distribution was found more non-uniform for angles of attack of 18°, 20°, and 24° in Figures 126 to 128. At the angle of attack of 24°, very early flow separation was observed due to high turbulence.

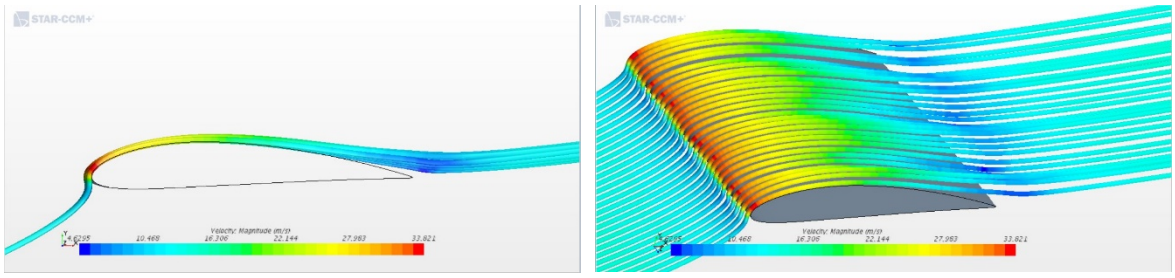

Figure 125: 4414_sin_0.6_0.2_100 streamline for Re=1x10^6; α=16°

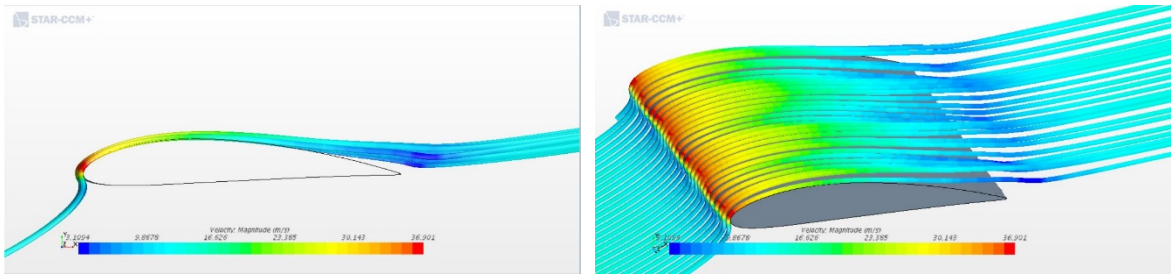

Figure 126: 4414_sin_0.6_0.2_100 streamline for Re=1x10^6; α=18°

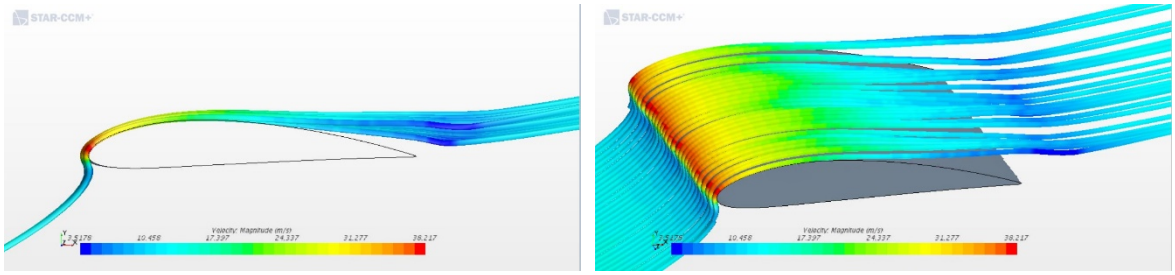

Figure 127: 4414_sin_0.6_0.2_100 streamline for Re=1x10^6; α=20°

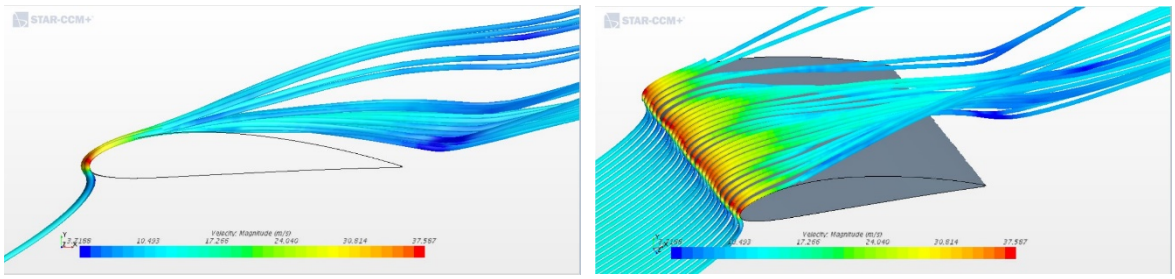

Figure 128: 4414_sin_0.6_0.2_100 streamline for Re=1x10^6; α=24°

At the Reynolds number 5x10^6, where velocity was 75 m/s, flow separation started significantly at a high angle of attack of 20°. At and below an 18° angle of attack, separation was minimal, and flow was attached to the top surface. Non-uniform distribution of flow

velocity was observed starting from the angle of attack of 20°, which is shown in Figure 130. The maximum velocity increased with increasing angle of attack. For the angle of attack of 28°, the maximum velocity was still in the subsonic zone.

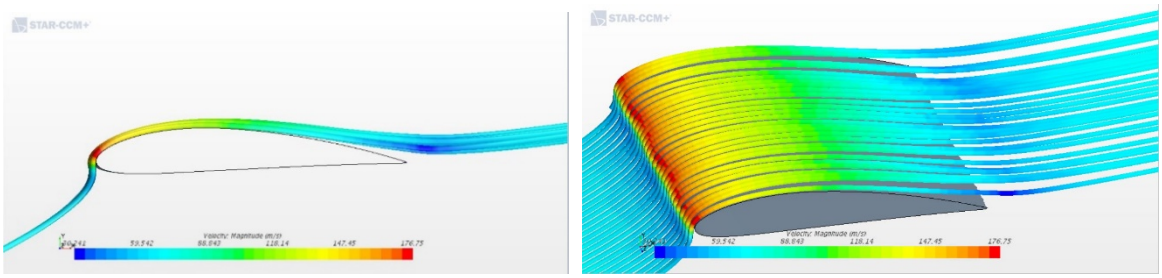

Figure 129: 4414_sin_0.6_0.2_100 streamline for Re=5x10^6; α=18°

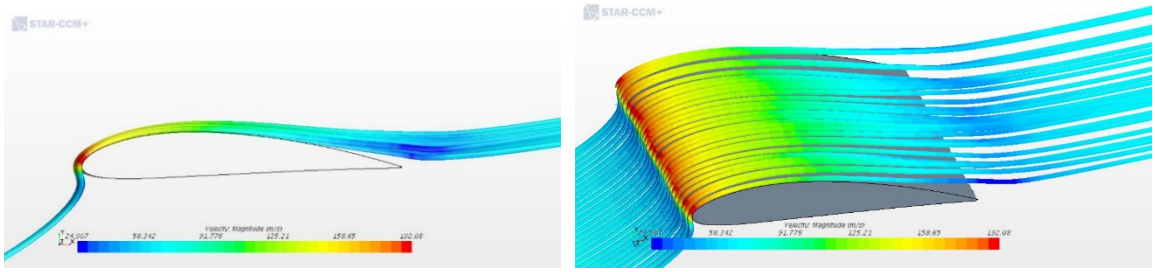

Figure 130: 4414_sin_0.6_0.2_100 streamline for Re=5x10^6; α=20°

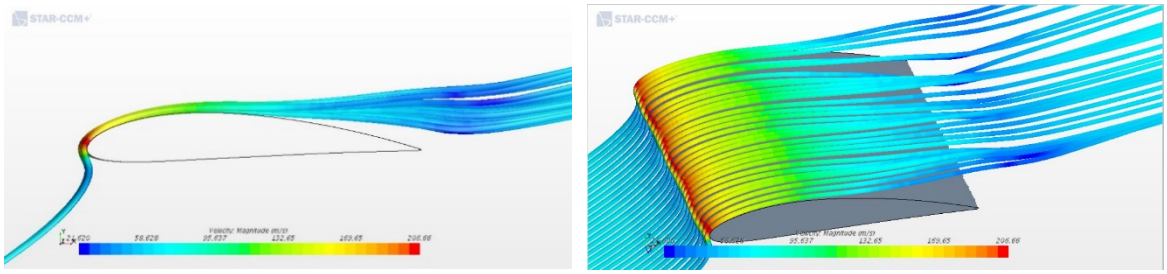

Figure 131: 4414_sin_0.6_0.2_100 streamline for Re=5x10^6; α=24°

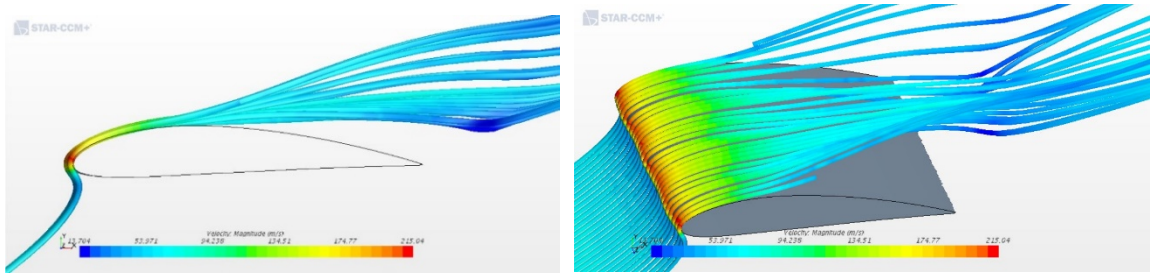

Figure 132: 4414_sin_0.6_0.2_100 streamline for Re=5x10^6; α=28°

At a Reynolds number of $10x10^6$ the inlet speed was 145 m/s, but the maximum speed exceeded the speed of sound for several angles of attack. In Figure 133 the flow speed was observed to be 361.36 m/s for angle of attack of 18°, which is larger than the speed of sound and falls in the supersonic zone. However, it was evident that flow separation was more delayed at this Reynolds number compared to the low and medium Reynolds numbers.

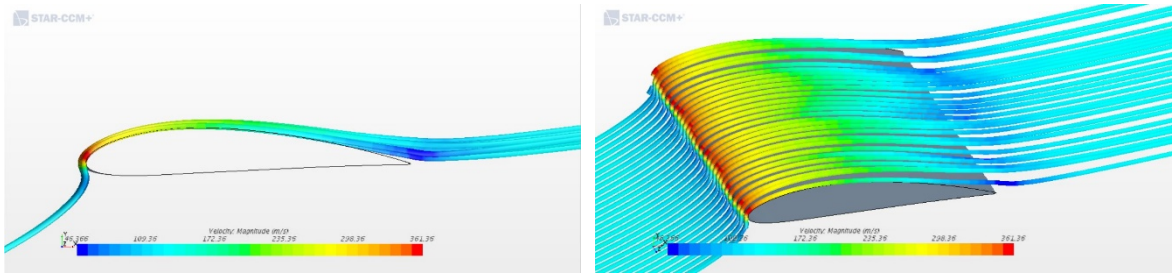

Figure 133: 4414_sin_0.6_0.2_100 streamline for Re=$10x10^6$; α=18°

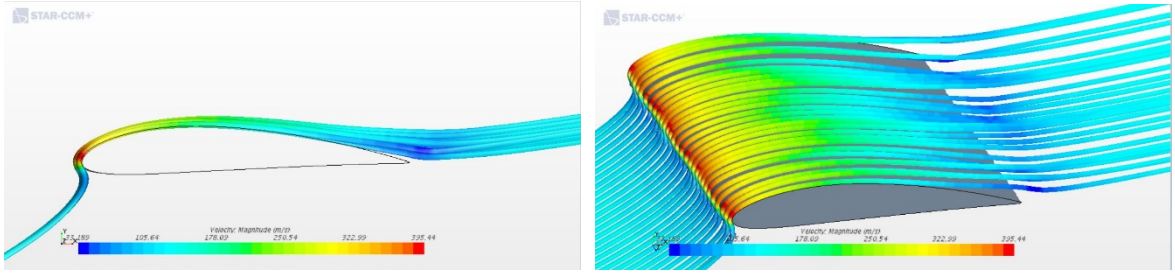

Figure 134: 4414_sin_0.6_0.2_100 streamline for Re=$10x10^6$; α=20°

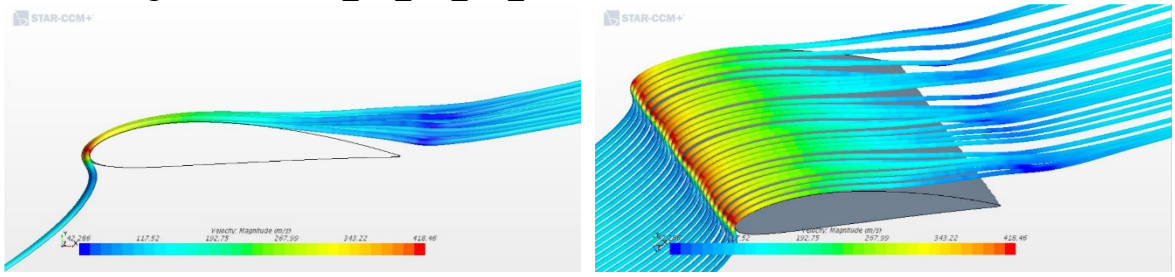

Figure 135: 4414_sin_0.6_0.2_100 streamline for Re=$10x10^6$; α=24°

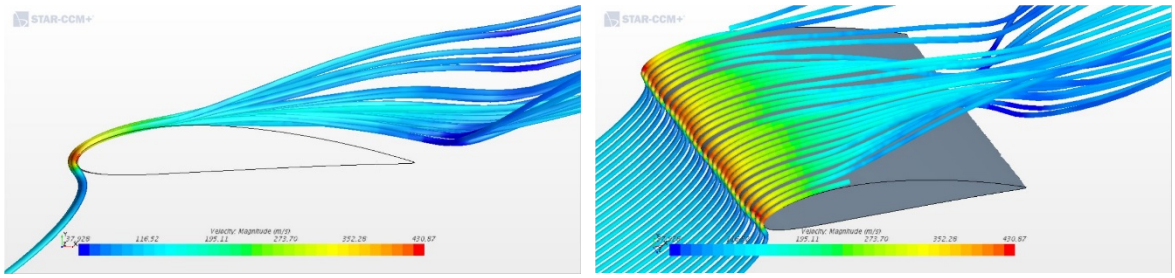

Figure 136: 4414_sin_0.6_0.2_100 streamline for Re=10x10^6; α=28°

For a Reynolds number of 10x10^6 the maximum velocity reached the supersonic zone. Hence, a solid conclusion can not be drawn about the data obtained from this model as in the physics model constant density was selected as the flow type. However, the pattern from the low Reynolds number to high Reynolds number shows that with the increase in Reynolds number the lift coefficient and stall angle increase which means that this tubercle airfoil can be used for high Reynolds number applications. Further investigation with appropriate physics model is required, and this is beyond the scope of this research.

7. Summary and Conclusion

In this study, various types of tubercle airfoils were developed in SolidWorks and tested with the CFD application tool Star CCM+. The alternative tubercle airfoil 4414_Tubercle1_25 with elliptical bumps at the leading edge provided better post-stall performance by preventing the drastic fall of lift coefficient. However, their performance was hindered in the pre-stall zone. The second type of alternative tubercle airfoil 4414_Tubercle4_50 with spherical bumps at the leading edge produced slightly higher lift coefficients than the base airfoil at all pre-stall and post stall angles of attack, but due to the high drag coefficient it eventually provided poor lift to drag ratio. The maximum lift was also reduced for the model by 1.42% from the base model. From the analysis of these two alternative models it was evident that these types of alternative tubercle models can also provide post stall performance enhancements like sinusoidal tubercles.

Varying amplitude models provided higher lift coefficients and lower drag coefficients before stall. Models with a high maximum amplitude such as 2.5% and 5% of the chord length stalled very early. Higher lift coefficients and stall angles were achieved by reducing the maximum amplitude. For model 4414_sin_0.015t_0.4_100, lift to drag ratio was found to be higher than the base airfoil at 0° and 4° angles of attack. In the post stall region these models suffered due to the rapid drop in lift and increase in drag.

The uniform sinusoidal model, 4414_sin_1_0.4_150, stalled at a 16° angle of attack, which was 2° early than the base airfoil. The lift coefficient curve followed the base airfoil lift curve with a slightly increased value at all angles of attack before stall, but due to the increased drag, the lift to drag ratio became lower than the base airfoil. By testing several uniform

sinusoidal models with various amplitudes and wavelengths it was found that low amplitude and longer wavelength contribute to better post stall performance. Among the tested models, an amplitude of 0.6% of the chord length and a wavelength of 31.4% of the chord length provided the optimal airfoil performance. An investigation was carried out with models with surface waviness and without surface waviness. It was found that surface waviness provided better aerodynamic performance.

Using the information found from the analysis an optimum tubercle airfoil of uniform sinusoidal type with an amplitude of 0.6% of the chord length and wavelength of 31.4% of the chord length was created and tested. For all angles of attack both in the pre-stall and post-stall region this airfoil provided a higher lift coefficient than the straight edge base airfoil with a maximum of 6.21% increase of C_L at the angle of attack 20°. Later, using this tubercle airfoil the effect of Reynolds number on the tubercle airfoil was analyzed by testing this airfoil at three different Reynolds numbers: $1x10^6$, $5x10^6$, and $10x10^6$ ($1x10^7$). It was observed that the tubercle airfoil demonstrated improved performance as the Reynolds number increased. At higher Reynolds numbers, the stall was also delayed.

8. Future Scope of Study

Tubercle geometry holds great potential as a passive flow control method. Using CFD for the analysis of many designs of tubercle airfoils provided an extensive opportunity to understand the physics of tubercles in this study. It was revealed from this study that alternative approaches for tubercles have potential to improve aerodynamics. Different geometric variations of these alternative tubercles can be further investigated. In this study, elliptical and spherical tubercles were investigated as alternative tubercles. Other shapes can be investigated with different sizes and distances, i.e. geometric parameters. A combination of different flow control techniques can be studied, such as vortex generators and tubercles. After numerical analysis, selective tubercle models can be run for experimental testing.

9. References

1. Soderman, P. T. (1972). Aerodynamic effects of leading-edge serrations on a two-dimensional airfoil.
2. Anderson, G. W. (1973). An experimental investigation of a high lift device on the owl wing (No. GAM/AE/73-6). Air Force Institute of Technology, Wright-Patterson Air Force Base, Ohio.
3. Bearman, P. W., & Owen, J. C. (1998). Reduction of bluff-body drag and suppression of vortex shedding by the introduction of wavy separation lines. Journal of Fluids and Structures, 12(1), 123-130.
4. Meyer, R., Bechert, D. W., & Hage, W. (1999). Wind tunnel experiments with artificial bird feathers for passive separation control on airfoils. In IUTAM Symposium on Mechanics of Passive and Active Flow Control (pp. 99-100). Springer, Dordrecht.
5. Watts, P., & Fish, F. E. (2001, August). The influence of passive, leading edge tubercles on wing performance. In Proc. Twelfth Intl. Symp. Unmanned Untethered Submers. Technol. Durham New Hampshire: Auton. Undersea Syst. Inst.
6. Lin, J. C. (2002). Review of research on low-profile vortex generators to control boundary-layer separation. Progress in Aerospace Sciences, 38(4-5), 389-420.
7. Miklosovic, D. S., Murray, M. M., Howle, L. E., & Fish, F. E. (2004). Leading-edge tubercles delay stall on humpback whale (Megaptera novaeangliae) flippers. Physics of fluids, 16(5), L39-L42.
8. Miklosovic, D. S., Murray, M. M., & Howle, L. E. (2007). Experimental evaluation of sinusoidal leading edges. Journal of aircraft, 44(4), 1404-1408.

9. Van Dam, C. P., Berg, D. E., & Johnson, S. J. (2008). Active load control techniques for wind turbines (No. SAND2008-4809). Sandia National Laboratories.
10. Carreira Pedro, H., & Kobayashi, M. (2008, January). Numerical study of stall delay on humpback whale flippers. In 46th AIAA aerospace sciences meeting and exhibit (p. 584).
11. Stanway, M. J. (2008). Hydrodynamic effects of leading-edge tubercles on control surfaces and in flapping foil propulsion (Doctoral dissertation, Massachusetts Institute of Technology).
12. Van Nierop, E. A., Alben, S., & Brenner, M. P. (2008). How bumps on whale flippers delay stall: an aerodynamic model. Physical review letters, 100(5), 054502.
13. Weber, P. W., Howle, L. E., Murray, M. M., & Miklosovic, D. S. (2011). Computational evaluation of the performance of lifting surfaces with leading-edge protuberances. Journal of Aircraft, 48(2), 591-600.
14. Fish, F. E., Weber, P. W., Murray, M. M., & Howle, L. E. (2011). The tubercles on humpback whales' flippers: application of bio-inspired technology.
15. Hansen, K. L., Kelso, R. M., & Dally, B. B. (2011). Performance variations of leading-edge tubercles for distinct airfoil profiles. AIAA journal, 49(1), 185-194.
16. Swatton, P. J. (2011). Principles of flight for pilots (Vol. 42). John Wiley & Sons.
17. Fernandes, I., Sapkota, Y., Mammen, T., Rasheed, A., Rebello, C., & Kim, Y. H. (2013). Theoretical and Experimental Investigation of Leading-Edge Tubercles on the Wing Performance. In 2013 Aviation Technology, Integration, and Operations Conference (p. 4300).

18. Lohry, M. W., Clifton, D., & Martinelli, L. (2012, July). Characterization and design of tubercle leading-edge wings. In Seventh International Conference on Computational Fluid Dynamics (ICCFD7), Big Island, Hawaii (pp. 9-13).
19. Hansen, K. L. (2012). Effect of leading edge tubercles on airfoil performance (Doctoral dissertation).
20. Rostamzadeh, N., Kelso, R. M., Dally, B. B., & Hansen, K. L. (2013). The effect of undulating leading-edge modifications on NACA 0021 airfoil characteristics. Physics of fluids, 25(11), 117101.
21. Rostamzadeh, N., Hansen, K. L., Kelso, R. M., & Dally, B. B. (2014). The formation mechanism and impact of streamwise vortices on NACA 0021 airfoil's performance with undulating leading edge modification. Physics of Fluids, 26(10), 107101.
22. Zhang, M. M., Wang, G. F., & Xu, J. Z. (2014). Experimental study of flow separation control on a low-Re airfoil using leading-edge protuberance method. Experiments in fluids, 55(4), 1710.
23. Bolzon, M. D., Kelso, R. M., & Arjomandi, M. (2016). Formation of vortices on a tubercled wing, and their effects on drag. Aerospace Science and Technology, 56, 46-55.
24. Ng, B. F., New, T. H., & Palacios, R. (2016). Effects of leading-edge tubercles on wing flutter speeds. Bioinspiration & biomimetics, 11(3), 036003.
25. Wei, Z., Zang, B., New, T. H., & Cui, Y. D. (2016). A proper orthogonal decomposition study on the unsteady flow behavior of a hydrofoil with leading-edge tubercles. Ocean Engineering, 121, 356-368.

26. Aftab, S. M. A., Razak, N. A., Rafie, A. M., & Ahmad, K. A. (2016). Mimicking the humpback whale: An aerodynamic perspective. Progress in Aerospace Sciences, 84, 48-69.

27. Bolzon, M. D., Kelso, R. M., & Arjomandi, M. (2017). Performance effects of a single tubercle terminating at a swept wing's tip. Experimental Thermal and Fluid Science, 85, 52-68.

28. Wei, Z., Lian, L., & Zhong, Y. (2018). Enhancing the hydrodynamic performance of a tapered swept-back wing through leading-edge tubercles. Experiments in Fluids, 59(6), 103.

29. Winslow, J., Otsuka, H., Govindarajan, B., & Chopra, I. (2018). Basic Understanding of Airfoil Characteristics at Low Reynolds Numbers (10 4–10 5). Journal of Aircraft, 55(3), 1050-1061.

30. Eleni, D. C., Athanasios, T. I., & Dionissios, M. P. (2012). Evaluation of the turbulence models for the simulation of the flow over a National Advisory Committee for Aeronautics (NACA) 0012 airfoil. Journal of Mechanical Engineering Research, 4(3), 100-111.

31. DiGiovanni, D., O'Hearn, J., Visser, R., Manoharan, S. (2018). The Design, Build, and Test of an Airfoil: An Experimental and Numerical Study on Flow Characteristics.